Technische
Universität
München

Walther-Meißner-
Institut für Tief-
Temperaturforschung

Bayerische
Akademie der
Wissenschaften

Observation of quantum switching in driven-dissipative superconducting oscillators

Master's thesis
Sebastiano Davide Covone

Supervisor: Prof. Dr. Rudolf Gross
Advisor: Dr. Kirill Fedorov
Garching – October 9, 2023

E Pangloss talvolta diceva a Candido, "Gli eventi forman tutti una catena nel migliore dei mondi possibili, perchè, finalmente, quando voi non foste stato cacciato a furia di calci nel deretano da un bel castello per amore di madamigella Cunegonda; quando non foste stato sottomesso all'Inquisizione; quando non aveste fatta a piedi l'America; quando non aveste dato un buon colpo di spada al barone; quando non aveste perso tutti i vostri montoni del bel paese d'Eldorado; non mangereste qui canditi e pistacchi". "Ben detto" rispose Candido "ma bisogna coltivare il nostro giardino".

Candide, Voltaire, Italian translation.

L'utopia è all'orizzonte. Mi avvicino di due passi, lei si allontana di due passi. Cammino per dieci passi e l'orizzonte si sposta di dieci passi più in là. Per quanto io cammini, non la raggiungerò mai. A cosa serve l'utopia? Serve proprio a questo: a camminare.
Utopia is on the horizon. I move two steps closer; it moves two steps further away. I walk another ten steps and the horizon runs ten steps further away. As much as I may walk, I'll never reach it. So what's the point of utopia? The point is this: to keep walking.

Eduardo Galeano

Contents

List of Figures

Introduction

Over the last century, quantum mechanics has revolutionized our understanding of the physical world, leading to an impetuous flow of scientific discoveries and technological progress. As of today, quantum mechanics promises to shape our future, thanks to the developments of quantum computation [2], quantum communication [3, 4, 5], and quantum sensing [6]. Despite the breadth of this advancements and discoveries, many fundamental questions remain unanswered. Among these, understanding how the transition between quantum and classical dynamics occurs is still an open problem [7], which motivates many theoretical and experimental efforts. In particular, Kerr non-linear oscillators are one of the most natural candidates to explore the boundaries between classical and quantum physics [8, 9, 10]. Furthermore, Kerr non-linear oscillators gained interest thanks to their applications as quantum-limited amplifiers [11], in error-correction [12] and quantum state engineering [13, 14, 15]. In this context, the current thesis focuses on analyzing an emitted radiation of Kerr non-linear oscillators operated in their *steady-state*. With in mind the long-term objective of exploring the transient dynamics of these oscillators and investigating whether they can be used as a source of non-classical microwave states useful for quantum information processing, this thesis aims to provide, the technical, theoretical, and experimental foundations for future experiments in this research field. Moreover, we analyze the emitted radiation of Kerr non-linear oscillators without *a-priori* assumptions on the measured quantum state.

To experimentally study the dynamics of the Kerr non-linear oscillators, superconducting quantum circuits [16], such as Josephson parametric amplifiers (JPA) and Josephson parametric converters (JPC), represent an ideal platform due to their reproducibility, interaction strengths and tunability [17, 18, 19]. The Josephson junction is the central component of such superconducting quantum circuits, which functions as a nonlinear, tunable, and lossless inductance. In particular, superconducting circuits realize strong Kerr non-linearities at the single-photon level [15], which can be utilized both for quantum studies and for applications related to quantum information processing. Moreover, these circuits operate in the gigahertz regime, which allows for their straightforward integration with microwave and electronic components.

In order to achieve our aforementioned scientific goals, our work is split into several parts. First, we concentrate on the technical aspects associated with our experiments. Specifically, we explain how we developed, programmed, and numerically tested the protocol for quantum tomography of propagating quantum microwave signals. Additionally, we illustrate how we designed and compiled the code for data acquisition by the field-programmable gate array

(FPGA) utilized in our experiments. In the theory part, we review the models found in the literature, constructing a robust theoretical foundation for the subsequent experimental phase of our work. In particular, we focus on describing one-photon and two-photon-driven Kerr oscillators, with a particular emphasis on the interplay between driving and dissipation [20, 21]. In the experimental part, we initially perform a careful calibration of the effects introduced by our amplification chain, which is essential for the room-temperature detection of propagating quantum signals generated by the superconducting circuits. Subsequently, building upon the prior theoretical research, we present our experimental measurements of the *steady-state* emission of both the JPA and JPC operated respectively as the two-photon and one-photon driven Kerr non-linear resonators, respectively.

The thesis is organized as follows. In Chapter 1, we provide the essential theory needed to analyze later experimental results. In Chapter 2, we describe the tomographic method for the reconstruction of experimental density matrices, applied to the heterodyne detection scheme that is used in our experiments. In Chapter 3, we describe the experimental set-up used during this work and explain the calibration of the amplification chain and superconducting devices. In Chapter 4, we review the theory of Kerr non-linear oscillators. Moreover, we numerically analyze transient and *steady-state* features of these systems using a master's equation approach and providing some insights on the displayed quantum-to-classical transition. In Chapter 5, we discuss the main experimental results obtained during this work and we analyze them by comparing them to the theoretical predictions developed in Chapter 4. Lastly, we give a conclusion of the thesis and provide an outlook.

Chapter 1

Propagating quantum microwaves

This chapter covers the fundamental theory needed to understand our work. In the first section, we briefly introduce the theoretical framework needed to model propagating quantum microwaves. In the second section, we summarize the theory of open quantum systems in the Markovian approximation, which is one of the most useful tools in the study of propagating quantum signals. In the last section, we describe the fundamental theory of the superconducting quantum circuits used to generate the quantum states of lights which are measured during this thesis work.

1.1 Propagating quantum microwaves

In this section, we give an elementary overview of the theory of propagating quantum microwaves. We first introduce the quantum representation of those signals in terms of bosonic creation and annihilation operators. Then, we review the most important mathematical representations of quantum signals: quasiprobability distributions and density matrices. At this point, we focus on Wigner W-function, Husimi Q-function and Glauber-Sudarshan P-function. For each of them, we highlight the definition, the physical interpretation, and their practical importance in the computation of specific expectation values.

1.1.1 Quantum description of propagating microwave signals

In this thesis work, we focus on microwave signals propagating on coaxial transmission lines. A complete treatment on the quantization of propagating microwave signals goes beyond the scope of this chapter; for this, we refer the reader to the standard textbook in quantum optics by G. Millburn and D. Walls [22].

Classical microwave signals A microwave signal whose bandwidth is much smaller compared to the carrier frequency is considered to be *narrow-band*. In our experiments, the carrier frequency is $\Omega_0/2\pi \approx 5$ GHz, while the signal bandwidth is always smaller than $\Delta f \approx 2$ MHz. In the *narrow-band* approximation, the voltage signal coming from the coaxial transmission line can be modeled as

$$V(t) = I(t)\cos\big(\Omega_0 t\big) + Q(t)\sin\big(\Omega_0 t\big), \tag{1.1}$$

where $I(t)$ and $Q(t)$ are the *in-phase* and *out-of-phase* quadrature components of the signal. The quadratures $I(t)$ and $Q(t)$ are slowly-varying time functions, in the sense that they vary appreciably on a time scale given by the inverse of the bandwidth Δf of the signal. We define the dimensionless function

$$A(t) = \sqrt{\frac{1}{2\kappa}} \left(I(t) - \mathrm{j}Q(t) \right), \tag{1.2}$$

where $\mathrm{j} = \sqrt{-1}$ is the imaginary unit and κ, measured in Volts^2, is the setup-dependent *photon number conversion factor* (PNCF). So, we can rewrite Eq. 1.1 in terms of the field $A(t)$ and its complex conjugate as

$$V(t) = \sqrt{k} \left(A(t) e^{\mathrm{j}\Omega_0 t} + A^*(t) e^{-\mathrm{j}\Omega_0 t} \right). \tag{1.3}$$

Propagating quantum microwaves To encompass quantum-mechanical effects, we convert the functions $A(t)$ and $A^*(t)$ to operators

$$\begin{aligned} A(t) &\rightarrow \hat{a}(t), \\ A^*(t) &\rightarrow \hat{a}^\dagger(t). \end{aligned} \tag{1.4}$$

It can be proved, as done by A. Clerk, in Ref. [23], that $\hat{a}$ and $\hat{a}^\dagger$ are bosonic operators satisfying the commutation relation

$$\left[\hat{a}^\dagger, \hat{a} \right] = \mathbb{I}, \tag{1.5}$$

where $\mathbb{I}$ is the idenity operator. The quantum-mechanical equivalent of Eq. 1.3, is therefore,

$$\hat{V}(t) = \sqrt{\kappa} \left(\hat{a}(t)\, e^{\mathrm{j}\Omega_0 t} + \hat{a}^\dagger\, (t) e^{-\mathrm{j}\Omega_0 t} \right). \tag{1.6}$$

1.1.2 Density operator

Density operators are ubiquitous in quantum mechanics. Mathematically, they provide the most fundamental description of a quantum state ([24]), by generalizing the idea of *pure-states* to a more experimentally relevant concept of *mixed-states*. Formally, given an infinite-dimensional or a finite-dimensional Hilbert space $\mathbb{H}$ and *any* basis $\left\{ \left| \psi_n \right\rangle \right\}_i$, every quantum state can be encoded in a uniquely defined operator

$$\rho = \sum_{n,m} c_{n,m} \left| \psi_n \right\rangle \left\langle \psi_m \right|, \tag{1.7}$$

where the coefficients $c_{n,m}$ depend only on the quantum state. Since the density operator contains all the information about the quantum state, in the following we will use the term *quantum state* to refer to the density operator of the specific quantum state.

1.1.3 Quasiprobability distributions

In this section, we define and analyze the main properties of the most commonly used quasiprobability distributions: the Glauber-Sudarshan P-function ([25]), the Wigner function

([26]) and the Husimi Q-function ([27]). On mathematical grounds, neither of them behaves like proper probability distributions: for instance, the Glauber-Sudarshan P-function can be a singular function; the Wigner function can assume negative values and the Husimi Q-function does not respect the third axiom of probabilities. Despite those limitations, quasi-probability distributions are useful tools and are commonly used to analyze the properties of quantum states of light and compute expectation values of the associated quantum states. For a comprehensive and in-depth discussion on the mathematical and physical properties of phase space distributions, we refer to Ref. [28].

Glauber-Sudarshan P-function

The P-function was defined in 1963 by R. Glauber ([29]) and G. Sudarshan ([25]), who worked independently on the subject in the same year. The P-function of a quantum state ρ is defined by the relation

$$\rho = \iint\limits_{\mathbb{C}} d^2\alpha \, P(\alpha) \left|\alpha\right\rangle \left\langle\alpha\right| . \tag{1.8}$$

Since every density matrix $\hat{\rho}$ is unit-trace, the P-function is normalized in the phase-space. The P-function allows to compute the expectation values of normally ordered products of field operators $\left(\hat{a}^\dagger\right)^n \hat{a}^m$, with n and m integers. From the definition, it can be readily derived that

$$\langle \left(\hat{a}^\dagger\right)^n \hat{a}^m \rangle = \iint\limits_{\mathbb{C}} d^2\alpha \, P(\alpha) \left(\alpha^*\right)^n \; \alpha^m . \tag{1.9}$$

Non-classicality condition The P-function allows to write any quantum state as a mixture of coherent displaced states $|\alpha\rangle$. This feature can be used to define a general criterion for the *non-classicality* or *quantumness* of a state of light. The criterion, introduced by M. Titulaer and R. Glauber in Ref. [30], states that a states of light ρ is classical *if and only if* its P-function behaves like a regular probability distribution in the phase space. In this case, indeed, ρ can be uniquely written as a classical mixture of coherent displaced states of light $|\alpha\rangle$. This state is classical, in the sense that it can be predicted by non-quantum theories and it does not have features such as quantum superposition. An example of a quantum states, which do not have classical analogs, is squeezed vacuum states: in fact, it can be shown, see Ref [31], that the P-function of squeezed vacuum state is negative in some regions of the phase-space.
Despite its conceptual elegance, the P-function is not easy to reconstruct experimentally. A method to experimentally retrieve the physical information encoded from the Glauber P-function was introduced by Kiesel et al. in Ref [32]. This method will be discussed in Chapter 5, in relation to our measurements.

Wigner function

The Wigner function of a quantum system is defined as the Weyl-transform of its density matrix ρ [33]. Formally, the Wigner function W_ρ associated to the quantum state ρ and computed in the phase-space point $\alpha = (q + \mathrm{j}p)\sqrt{2}$ is given by

$$W_\rho(\alpha) = \int dy\, e^{-\mathrm{j}py} \langle q + y/2|\hat{\rho}|q - y/2\rangle \tag{1.10}$$

where $|q\rangle$ (p), with $q(p) \in \mathbb{R}$, labels the eigenvectors of the quadrature operators

$$\begin{aligned} \hat{q} &= \frac{1}{\sqrt{2}}\left(\hat{a} + \hat{a}^\dagger\right), \\ \hat{p} &= \frac{1}{\sqrt{2}\mathrm{j}}\left(\hat{a} - \hat{a}^\dagger\right), \end{aligned} \tag{1.11}$$

where the coefficient $\sqrt{2}$ is chosen to preserve the commutation relation

$$\left[\hat{q}, \hat{p}\right] = \mathrm{j}. \tag{1.12}$$

The Wigner function is normalized in the phase-space $\mathbb{C}$,

$$\iint_{\mathbb{C}} W(\alpha) d^2\alpha = 1 \tag{1.13}$$

and it is useful to compute expectation values of product operators of the type $\hat{q}^n \hat{p}^m$, where n and m are integers. Indeed, for a product operator of this kind, the expectation value can be computed easily as

$$\langle \hat{q}^n \hat{p}^m \rangle = \frac{1}{2} \int dq\, q^n \int dp\, p^m W(q,p), \tag{1.14}$$

where we made the changed coordinates using

$$\begin{aligned} q &= \frac{\alpha + \alpha^*}{\sqrt{2}} \\ p &= \frac{\alpha - \alpha^*}{\sqrt{2}\mathrm{j}}. \end{aligned} \tag{1.15}$$

Wigner functions can not be interpreted as probability distributions because they are not bound to be positive everywhere; in the following section, we explore the connection between the negativity of the Wigner function and the purity of the quantum states.

Why Wigner functions become negative? Let us suppose that we have two pure states $|\phi\rangle$ and $|\psi\rangle$ which are orthogonal, i.e $\langle\phi|\psi\rangle = 0$. Without loss of generality, we assume that $|\phi\rangle$ has a positive Wigner distribution W_ϕ; a pure state with this feature is the vacuum state $|0\rangle$. In terms of the Wigner functions, Ref. [33], the orthogonality condition can be written as

$$\langle\phi|\psi\rangle = \iint_{\mathbb{C}} W_\phi(\alpha) W_\psi(\alpha) d^2\alpha = 0. \tag{1.16}$$

Since $W_\phi(\alpha) \geq 0$ for all $\alpha \in \mathbb{C}$, there must be a set of points $\beta \in \mathbb{C}$ for which $W_\phi(\beta) < 0$ in order for the relation 1.16 to be satisfied. So, Wigner *negativity* is a necessary feature for a set of *pure* and orthogonal quantum states, as the Fock-states, $|n\rangle$ ([24]). For this reason, Wigner *positivity* can be related to the mixing of pure states with an environment. To corroborate the last statement, we numerically studied the case of a pure quantum state $|1\rangle\langle 1|$ mixed with a thermal state ρ_{th} of photon population $\bar{n} = 1$ by a mixing factor ϵ,

$$\rho(\epsilon) = (1 - \epsilon)\,|1\rangle\langle 1| + \epsilon\rho_{\text{th}}, \tag{1.17}$$

where the $(1 - \epsilon)$ factor is necessary to preserve the unit trace of the density matrix. In the limiting cases of $\epsilon \to 0$ and $\epsilon \to 1$, we have respectively a pure quantum state, the Fock state $|1\rangle$, and the mixed state ρ_{th}. Numerically, we computed and plotted the negative volume $V_N(\epsilon)$ and the purity $\mathcal{P}(\epsilon) = \text{Tr}\left(\rho(\epsilon)^2\right)$, where $V_N(\epsilon)$ of a quantum state ρ is defined as

$$V_N = \iint_{\mathbb{C}} d^2z\, \left|W(z)\right| - 1. \tag{1.18}$$

The results of the numerical analysis are showed in Fig. 1.1.

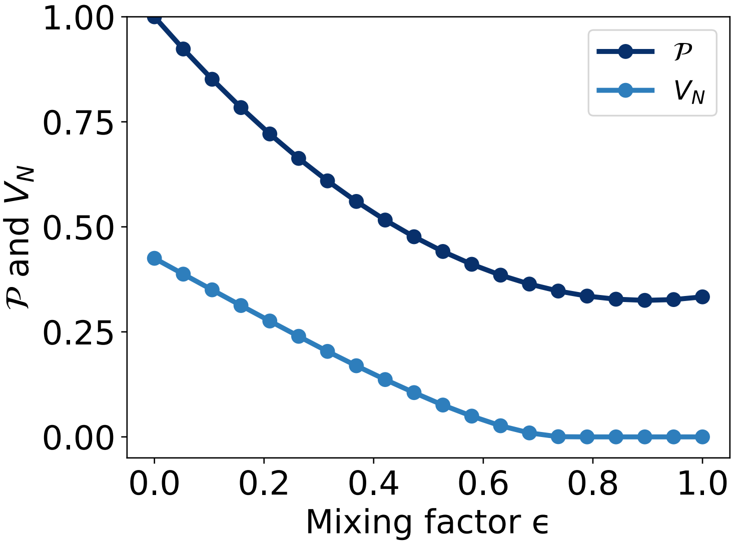

Figure 1.1: The negative Volume V_N and purity $\mathcal{P}$ as a function of the mixing parameter ϵ. As $\epsilon \to 1$, the purity saturates to the purity of the thermal state ρ_{th} and the negative volume goes to zero.

The results show a clear correlation between coupling to the environment and the exponential disappearance of the negativity in the Wigner function. It is also worth it to keep in mind that Wigner *negativity* is a *sufficient* condition for a general state, not necessarily pure, ρ to be defined *quantum*, but not a *necessary* one. Indeed, squeezed-vacuum states are non-classical states, but their Wigner function is a Gaussian distribution in the phase-space.

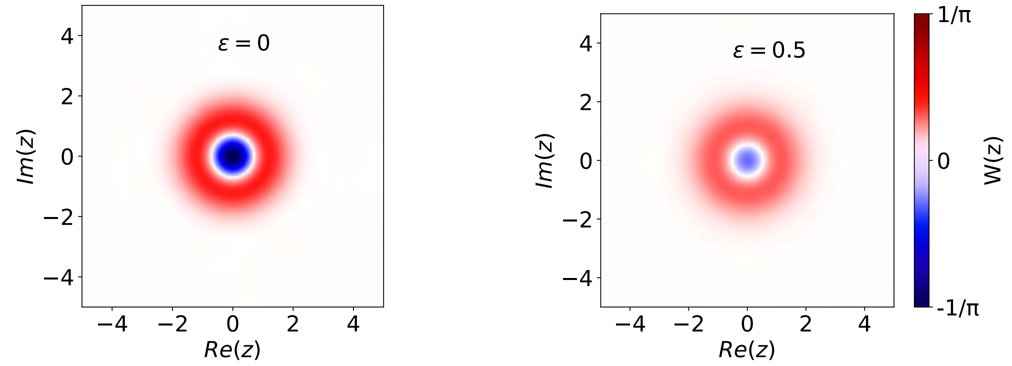

(a) **(b)**

Figure 1.2: (a) Wigner function of partially mixed state $\rho(\epsilon)$ for $\epsilon = 0.5$. (b) Wigner function of totally mixed state $\rho(\epsilon)$ for $\epsilon = 1$.

Husimi Q-function

The Husimi Q-function for a given quantum state ρ is defined as

$$Q_\rho(\alpha) = \frac{\langle\alpha|\rho|\alpha\rangle}{\pi} \tag{1.19}$$

where the π factor in the denominator ensures the phase-space normalization of the function:

$$\int_{\mathbb{C}} d^2\alpha\, Q_\rho(\alpha) = 1. \tag{1.20}$$

From now on, we indicate the Q-function simply as $Q(\alpha)$, omitting the subscript ρ. In contrast to the Wigner function, $Q(\alpha)$ is *always* positive since it measures the overlap between the state ρ and the coherent state $|\alpha\rangle$. Despite this, the Q-function is *not* a proper probability distribution; in fact, two different coherent states $|\alpha\rangle$ and $|\alpha'\rangle$ are not-orthogonal, so $Q(\alpha)$ and $Q(\alpha')$ do not represent the probabilities of two mutually exclusive states.

The Husimi Q-function is related to the Wigner function by the convolution

$$Q(\alpha) = \int_{\mathbb{C}} d^2\beta\, W(\beta - \alpha)e^{-|\beta|^2/2}. \tag{1.21}$$

This equation provides a conceptually elegant insight into the positivity of the Husimi Q-function: in particular, Eq. 1.21 states that the Q-function is just the Wigner function smoothened over a gaussian with variance value equal 1/2.

The Q-function is used to compute expectation values of *anti-ordered* products of the annihilation and creation operators: the most general product of this kind is $a^n \left(a^\dagger\right)^m$, with n, m arbitrary integers. By using the completeness relation for coherent states, it is easy to prove from equation 1.19 that

$$\langle a^n \left(a^\dagger\right)^m \rangle = \int_{\mathbb{C}} d^2\alpha\, \alpha^n \alpha^{*m} Q(\alpha). \tag{1.22}$$

We note that expectation values of products of annihilation and creation operators, which are not *anti-ordered*, are not straightforward to calculate using the Q-function representation.

1.2 Open quantum systems

In order to extract information from a quantum system, it is necessary to couple it to an external environment. For this reason, we provide a concise introduction to the theory of non-isolated microwave quantum systems. We start with a brief review of the *input-output* theory, originally developed by Collet and Gardiner [34]. Then, we explain the main idea behind the derivation of the density matrix master equation, starting from the input-output theory. Lastly, we present a quick treatment of the numerical solution of the density matrix master equation, which relies on the Choi–Jamiolkowski isomorphism [35], [36].

1.2.1 Input-output theory

The first and simplest version of the input-output theory was developed by Collet and Gardiner in their seminal paper [34]. Our quantum system of interest is described by an Hamiltonian H_S, which depends only on the creation and annihilation operators of the cavity mode, which we label as $\hat{b}$. In general, the cavity will have its own resonance frequency ω_0 and we can write the Hamiltonian H_S as

$$H_S = \hbar\omega_0 \hat{b}^\dagger \hat{b} + h_S, \tag{1.23}$$

where h_S describes other features of the system, such as an external pump or non-linearities of different orders.

The cavity is coupled to an external environment, which can be described by a Hamiltonian H_{env}

$$H_{\text{env}} = \int d\omega\, \hbar\omega\, \hat{a}(\omega)^\dagger \hat{a}(\omega), \tag{1.24}$$

where the modes $\hat{a}(\omega)$ form a continuous set which satisfies the commutation relation

$$\left[\hat{a}(\omega), \hat{a}(\omega')^\dagger\right] = \delta(\omega - \omega'). \tag{1.25}$$

The first assumption of the input-output theory is that the interaction operator H_{int} between the cavity and the waveguide is linear in both $\hat{b}$ and $\hat{a}(\omega)$; this implies that H_{int} is of the type

$$H_{\text{int}} = \int d\omega\, g(\omega) \left(b^\dagger + b\right) \left(a(\omega)^\dagger + a(\omega)\right), \tag{1.26}$$

where the function $g(\omega)$ describes the strength of the coupling between the environment modes $\hat{a}(\omega)$ and the cavity mode $\hat{b}$. The total Hamiltonian is

$$H_{\text{tot}} = H_S + H_{\text{env}} + H_{\text{int}}. \tag{1.27}$$

The second assumption of input-output theory is that all the relevant dynamics happens in a small frequency range around the resonance frequency ω_0 of the cavity. This assumption let us to transform equation 1.27 in the frame rotating with frequency ω_0 and to perform the *rotating wave approximation* (RWA). The transformed total Hamiltonian reads

$$H'_{tot} = h'_S + \int_{-\omega_0}^{\infty} d\omega\, \hbar\omega\, \hat{a}(\omega)^\dagger \hat{a}(\omega) + \int_{-\omega_0}^{\infty} d\omega\, \hbar g(\omega) \left(b^\dagger a(\omega) + b a(\omega)^\dagger \right), \tag{1.28}$$

where h'_S is the operator h_S defined in 1.23 transformed in the rotating frame.
The third and final assumption of this theory is that the coupling strength $g(\omega)$ is frequency-independent, i.e. $g(\omega) = g$ for all the frequencies ω. This approximation is also known as Markov approximation. We define the external coupling factor γ_e as

$$\gamma_e = g^2. \tag{1.29}$$

Therefore,

$$H'_{\text{tot}} = h'_S + \int_{-\omega_0}^{\infty} d\omega\, \hbar\omega\, \hat{a}(\omega)^\dagger \hat{a}(\omega) + \hbar \sqrt{\gamma_e} \int_{-\omega_0}^{\infty} d\omega \, \left(b^\dagger a(\omega) + b a(\omega)^\dagger \right). \tag{1.30}$$

Langevin Equations

In the Heisenberg picture, all operators in Eq. 1.30 depend on time. To obtain the equation of motion for the cavity operator $\hat{b}$, we have to evaluate the Heisenberg equation of motion,

$$\frac{d}{dt}\hat{b} = -\frac{\mathrm{j}}{\hbar} \left[H'_{\text{tot}}, \hat{b} \right]. \tag{1.31}$$

Computing the commutator in the last equation gives us

$$\frac{d}{dt}\hat{b} = -\frac{\mathrm{j}}{\hbar} \left[h'_S, \hat{b} \right] - \frac{\gamma_e}{2} \hat{b}(t) + \mathrm{j} \sqrt{\gamma_e} \int_{-\omega_0}^{\infty} d\omega\, a(\omega, 0) e^{-\mathrm{j}\omega t}. \tag{1.32}$$

We define the input field a_{in} as

$$a_{\text{in}}(t) = \int_{-\omega_0}^{\infty} d\omega\, a(\omega, 0) e^{-\mathrm{j}\omega t}. \tag{1.33}$$

Physically the input field a_{in} describes the free-evolution in time of the external modes $a(\omega)$ at time $t = 0$, before the interaction with the cavity. In more practical terms, the profile $a(\omega, 0)$ of the external modes at the initial time $t = 0$ fully determines the interaction between the cavity and the waveguide. If we substitute the definition of the input field $a_{\text{in}}(t)$ 1.33 in the time equation for $\hat{b}$ 1.32, we get

$$\frac{d}{dt}\hat{b} = -\frac{\mathrm{j}}{\hbar} \left[h'_S, \hat{b} \right] - \frac{\gamma_e}{2} \hat{b}(t) + \mathrm{j} \sqrt{\gamma_e} a_{\text{in}}(t). \tag{1.34}$$

The equation 1.34 is known as the quantum Langevin equation for the cavity mode $\hat{b}$. Theoretically, this equation allows us compute cavity modes at any given time t, if we know the initial condition $\hat{b}(t = 0)$ and the input mode $a_{\text{in}}(t)$.

1.2.2 Output-mode and boundary conditions

While equation 1.34 correctly describes the intra-cavity dynamics, the latter is never observed experimentally. Indeed, in experiments, we can only retrieve physical information from the external modes $a(\omega)$. To build a model that describes the effect of the cavity modes $\hat{b}$ on the external modes $a(\omega)$, we define the output-mode a_{out} as

$$a_{\text{out}}(t) = \int_{-\omega_0}^{\infty} d\omega\, a(\omega, \infty) e^{\mathrm{j}\omega t}. \tag{1.35}$$

Physically, the input field a_{out} describes the backward evolution in time (see the sign of ω in the last equation) of the operators $a(\omega)$ computed at time $t \to \infty$, *after* the interaction with the cavity. It can be proved, see Ref. [34], that, in terms of the output-mode operator a_{out}, the equation of motion is

$$\frac{d}{dt}\hat{b} = -\frac{\mathrm{j}}{\hbar}\left[h'_S, \hat{b}\right] + \frac{\gamma_e}{2}\hat{b}(t) + \mathrm{j}\sqrt{\gamma_e} a_{\text{out}}(t). \tag{1.36}$$

If we subtract the last equation to equation Eq. 1.34, we derive the boundary-condition for the quantum Langevin equation,

$$a_{\text{out}}(t) = a_{\text{in}}(t) + \mathrm{j}\sqrt{\gamma_e}\hat{b}(t). \tag{1.37}$$

So, if we both know the input mode $a_{\text{in}}(t)$, the cavity mode $b\hat{(t)}$, we can obtain the information about the measured quantum mode thanks to the boundary condition 1.37.

1.2.3 Loss modes

In experiments, the cavity never interacts only with the observable external modes $\hat{b}(\omega)$. Indeed, our cavity often interacts with other degrees of freedom whose dynamics cannot be measured, such as parasitic two-level systems due to fabrication imperfections. In the framework of the input-output theory, we describe those degrees of freedom introducing the loss modes $c(\omega)$. The loss mode interact with the cavity with an Hamiltonian H_{loss} given by

$$H_{loss,cavity} = \sqrt{\gamma_i} \int_{-\omega_0}^{\infty} d\omega \left(c(\omega)^\dagger b + c(\omega) b^\dagger\right), \tag{1.38}$$

where the factor γ_i is the internal loss rate and quantifies the amount of energy per unit of time that the system lose by interacting with the loss modes. Including the Hamiltonian 1.38 in the

Heisenberg equation of motion 1.31, we get a new quantum Langevin equation

$$\frac{d}{dt}\hat{b} = -\frac{\mathrm{j}}{\hbar}\left[h'_S, \hat{b}\right] - \frac{\gamma}{2}\hat{b}(t) + \mathrm{j}\sqrt{\gamma_e}a_{in}(t) + \mathrm{j}\sqrt{\gamma_i}c_{in}(t), \tag{1.39}$$

where $\gamma = \gamma_i + \gamma_e$ is the *total loss rate* which quantifies the rate at which the cavity loses the information stored inside it and $c_{\text{in}}(t)$ is the input mode associated to the loss-modes.

1.2.4 Master equation

The quantum Langevin equation 1.39, derived in the previous section, is often practically intractable. In some simple cases, this equation is equivalent to a description formulated using the quantum state density matrix ρ. The time equation for ρ is referred to as master's equation. The derivation of the master's equation, presented in full details in Ref. [34], is based on the idea that the expectation values computed using the quatum Langevin equation and the master's equation should be identical. In equations,

$$\mathrm{Tr}\left(\hat{a}\frac{d}{dt}\rho\right)_S = \mathrm{Tr}\left(\left(\frac{d}{dt}\hat{a}\right)\rho\right)_H, \tag{1.40}$$

where H and S subscripts indicate respectively Schroedinger's and Heisenberg's pictures. In the following part of this section, we present the explicit form of the master's equation in two simple cases which are relevant to our experiments:

1. interaction of the cavity with vacuum noise;
2. interaction of the cavity with a coherent tone.

Interaction with vacuum noise When the both the input mode a_{in} and the loss mode c_{in} describe quantum fluctuations, the resulting equation of motion for the cavity density operator ρ is

$$\frac{d}{dt}\rho(t) = \frac{i}{\hbar}\left[\rho, h'_S\right] + \frac{\gamma}{2}\left(2\hat{b}\rho\hat{b}^\dagger - \left\{\hat{b}^\dagger\hat{b}, \rho\right\}\right) = \mathcal{L}(\rho(t)). \tag{1.41}$$

The super-operator $\mathcal{L}$ is called Lindbladsuper-operator and equation 1.41 is also known as Lindblad master's equation [37]. This equation is useful to model the case of the two-photon pumped JPA described in Chapter 4. In that case, the two-photon pump can be included as a term of the system's Hamiltonian operator and we can assume that the input fields a_{in} and c_{in} descibe weak-thermal states with photon population $\bar{n} < 10^{-3}$.

Interaction with a coherent tone Another case of interest is when the input loss mode c_{in} describes vacuum fluctuations and the input mode a_{in} describes a *classical* coherent tone of power P_{in} and frequency ω_{in}. This case is relevant for our experiments, since we use a Josephson parametric converted (JPC) as a resonantly driven non-linear oscillator. The theory and the results of these experiments are explained respectively in Chapters 4 and 5. The equation of motion in this case is

$$\frac{d}{dt}\rho(t) = \mathcal{L}'\left(\rho(t)\right), \tag{1.42}$$

where $\mathcal{L}'$' is computed as

$$\mathcal{L}'(\rho(t)) = \frac{\mathrm{j}}{\hbar}\left[\rho, h'_S\right] + \frac{\mathrm{j}\Delta}{\hbar}\left[\rho, \hat{b}^\dagger\hat{b}\right] - \frac{\Omega}{\hbar}\left[\rho, \left(\hat{b}^\dagger - \hat{b}\right)\right] + \frac{\gamma}{2}\left(2\hat{b}\rho\hat{b}^\dagger - \left\{\hat{b}^\dagger\hat{b}, \rho\right\}\right), \tag{1.43}$$

where $\Delta = \omega_0 - \omega_{in}$ is the detuning between the cavity and the resonant mode and $\Omega = \sqrt{\gamma_e P_{in}/\hbar\omega_0}$ quantifies the strength of the interaction between the coherent input tone and the cavity.

1.2.5 Numerical treatment of the master's equation

In this section we explain how to solve numerically the master's equations 1.41 and 1.42 in both the time-transient and steady-state regimes. The techniques explained in this section are used in the next chapters of this thesis.

Dimensional cutoff

For quantum states associated with the bosonic annihilation and creation operators, the Hilbert space has infinite dimensions. In order to numerically represent the density matrix of a infinite-dimensional Hilbert space, we have to introduce a cutoff dimension $\mathcal{D}_c$. As a rule of thumb, in order to not introduce numerical artifacts in the state representation, $\mathcal{D}_c$ is chosen such that

$$\mathcal{D}_c \gg \bar{N} = \mathrm{Tr}\left[b^\dagger b\,\rho\right]. \tag{1.44}$$

If we want to simulate the equation of motion over a time-interval $[t_0, t_f]$ this last rule can be generalized in such a way that the cutoff dimension is large enough for every point in the considered time interval:

$$\mathcal{D}_c \gg \max_{t\in[t_0,t_f]} \bar{N}(t). \tag{1.45}$$

Choi-Jamiolkowki isomorphism

The Choi-Jamiolkowki isomorphism ([35]) makes it possible to rewrite the non-linear master's equation as a first-order linear differential equation, without any approximation. This possibility allows for the straightforward numerical implementation of the master's equation in both the transient and steady-state regimes. Formally, it states that there is a one-to-one correspondence between the set of *trace preserving* and *completely positive* quantum channels, such as the Lindblad super-operator $\mathcal{L}$, acting on a Hilbert space of dimension $\mathcal{D}$ and the set of non-negative linear operators acting on a larger Hilbert space of dimension $\mathcal{D}^2$. This theoretical result has two important consequences:

1. any density matrix on the Hilbert space of dimension $\mathcal{D}$, $\mathcal{H}$, is equivalent to a pure state, a *ket*, on the Hilbert space of dimension $\mathcal{D}^2$, $\mathcal{H}'$. In practice, we can associate to each density matrix $\hat{\rho} \in \mathcal{H}$ a ket $\left|\rho\right\rangle \in \mathcal{H}'$: this can be realized by rearranging the entries of the density matrix to form a column vector.

2. We can associate to the non-linear super-operator $\mathcal{L}$ acting on the Hilbert space $\mathcal{H}$ an equivalent linear and non-negative operator $\hat{L}$ acting on the Hilbert space $\mathcal{H}'$. The linear operator $\hat{L}$ is equivalent to $\mathcal{L}$ in the sense that the non-linear Lindblad master's equation is equivalent to the linear equation

   $$\frac{d}{dt}\left|\rho\right\rangle = \hat{L}\left|\rho\right\rangle . \tag{1.46}$$

   As proved in Ref. [38], it is possible to provide an explicit expression for the linear operator $\hat{L}$:

   $$\begin{aligned}\hat{L} = -\mathrm{j}\left[(h_S' \otimes \mathbb{I}) - \left(\mathbb{I} \otimes {h_S'}^{\mathrm{TR}}\right)\right] \\ + \frac{\gamma}{2}\left(2\hat{b} \otimes \hat{b}^* - \hat{b}^\dagger \hat{b} \otimes \mathbb{I} - \mathbb{I} \otimes \hat{b}^{\mathrm{TR}} \hat{b}^*\right),\end{aligned} \tag{1.47}$$

   where $\otimes$ labels the outer product ([39]).

If the initial condition $\left|\rho\right\rangle (t = 0)$ is known, the linear equation 1.46 can be implemented in common programming languages such as Python, using standard numerical integration techniques. In the following chapters, we used a fourth-order Runge-Kutta method [40] implement using the "Qutip" [41] package for the Python programming langauge.

Steady state solution By definition, the steady-state, ρ_{ss}, of a quantum system exists if

$$\frac{d}{dt}\left|\rho_{\mathrm{ss}}\right\rangle = 0. \tag{1.48}$$

Using equation 1.46, the last equation is equivalent to

$$\hat{L}\left|\rho_{\mathrm{ss}}\right\rangle = 0. \tag{1.49}$$

Since, from the Choi-Jamiolwski isomorphism, we know that $\hat{L}$ is a non-negative operator, its eigenvalues $\{\lambda\}$ have non-negative real parts. Then, we can find the steady-state ρ_{ss} computing the eigenvector of $\hat{L}$ with the eigenvalue which has the smallest real part. If it exists an eigenvalues λ_0 with $\mathrm{Re}\{\lambda_0\} = 0$ (within the numerical accuracy), the corresponding eigenvector is the wanteds steady-state.

The problem of finding and sorting the eigenvalues and eigenvectors can be solved using the iterative Lanczos Algorithm ([42]), which is implemented in standard modern numerical libraries such as the "linalg" package of the SciPy ([43]). We observe that this approach is much faster and more memory efficient compared to solving the equation 1.46 and taking the limit

$t \rightarrow \infty$.

1.3 Superconducting quantum circuits

In this section, we present the superconducting quantum devices we use in this thesis work to generate the quantum states of light which are measured in Chapter 5. In particular, we aim to describe the Josephson parametric amplifier (JPA) and the Josephson parametric converter (JPC).

1.3.1 Josephson junctions

The Josephson effect, discovered by B. D. Josephson in 1962 [44], occurs when two superconductors are weakly coupled to each other, often by introducing a thin insulating barrier and forming a Josephson junction. This macroscopic quantum phenomenon is described by the first and second Josephson equations [45],

$$\begin{aligned} I_s(\varphi) &= I_c \sin\left(\varphi\right), \\ \frac{\partial \varphi}{\partial t} &= \frac{2\pi}{\Phi_0} V(t), \end{aligned} \tag{1.50}$$

where φ is the gauge-invariance phase difference across the junction, I_s is the supercurrent flowing trough the junction, I_c is the Josephson critical current of the junction. $\Phi_0 = h/(2e)$ is the flux quantum and $V(t)$ is voltage across the junction. The non-linear inductance, L_s, of the junction can be computed from the definition of inductance $V = LdI/dt$,

$$L_s(\varphi) = \frac{\Phi_0}{2\pi I_c \cos(\varphi)} = \frac{L_c}{\cos(\varphi)}. \tag{1.51}$$

where $L_c = \Phi_0/(2\pi I_c)$ is the minimum junction inductance [45].

1.3.2 DC-SQUID

The direct-current superconducting quantum interference device (DC SQUID) is a powerful quantum device and it consists of two Josephson junctions in a superconducting loop. It was first realized by R. C. Jaklevic et al. in 1964 [46]. In the simplest case, the superconducting loop is composed by two nominally identical Josephson junctions of critical current I_c. Then, the phase difference between the two junction is

$$\varphi_1 - \varphi_2 = \frac{2\pi\Phi}{\Phi_0} + 2\pi n, \tag{1.52}$$

where $n \in \mathbb{Z}$ and $\Phi = \Phi_e + L_{\text{loop}} I_{\text{circ}}$ is total magnetic flux through the loop, which is given by two contributions: the applied external flux Φ_e and the self-induced flux $L_{\text{loop}} I_{\text{circ}}$, where L_{loop} is the self-inductance of the superconducting loop and I_{circ} is the circulating current. The total magnetic flux through the DC-SQUID is given by [45],

$$\frac{\Phi}{\Phi_0} = \frac{\Phi_\mathrm{e}}{\Phi_0} - \frac{\beta_\mathrm{L}}{2} \cos\left(\frac{\varphi_1 + \varphi_2}{2}\right) \sin\left(\frac{\varphi_1 - \varphi_2}{2}\right) \tag{1.53}$$

where $\beta_L = 2L_\mathrm{loop}I_\mathrm{circ}/\Phi_0$ is the screening parameter. In the case $\beta_{\simeq}0$, the self-inductance of the DC-SQUID can be neglected and $\Phi \simeq \Phi_e$. In this case, the maximum transport current of the DC-SQUID is

$$I_s^\mathrm{max} = 2I_c \left|\cos\left(\pi \frac{\Phi_e}{\Phi_0}\right)\right|, \tag{1.54}$$

and can be modulated by applying an external magnetic flux Φ_e. In this regime, the DC-SQUID can be viewed as a single Josephson junction with maximum supercurrent modulated by an external magnetic flux. We can then express a flux-tunable inductance, $L_s(\Phi_e)$, of the DC-SQUID [47],

$$L_s(\Phi_e) = \frac{\Phi_0}{4\pi I_c \left|\cos\left(\frac{\pi\Phi_e}{\Phi_0}\right)\right|} = \frac{L_c}{\left|\cos\left(\frac{\pi\Phi_e}{\Phi_0}\right)\right|}, \tag{1.55}$$

This implies that the DC-SQUID can be regarded as a flux-tunable inductance, and we can exploit it as a nonlinear building block in superconducting circuits.

1.3.3 Josephson parametric amplifiers

A flux-driven JPA [48, 49] is a superconducting resonator that consists of a coplanar waveguide (CPW) short-circuited to ground via a direct current superconducting quantum interference device. The JPA can be used to achieve parametric amplification of microwave signals and to generate squeezed states. Since the physical dimensions of the CPW is comparable to microwave wavelengths, we should describe the CPW with a distributed-element model as shown by the schematic in Fig. 1.3. Furthermore, we can neglect losses in the superconducting CPW and use the telegrapher's equations to derive its characteristic impedance [50],

$$Z_c = \frac{L_0}{C_0}, \tag{1.56}$$

where L_0 and C_0 are the inductance and capacitance per unit-length.

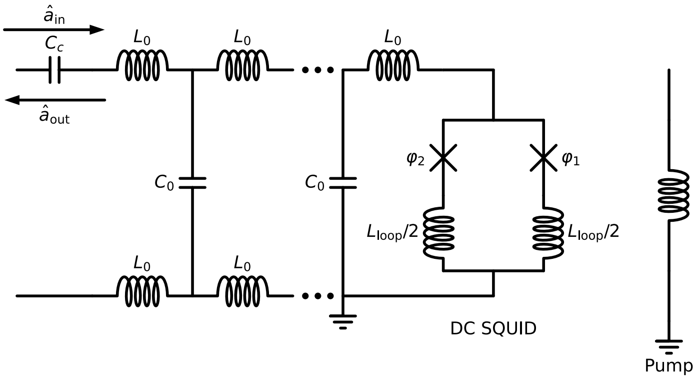

Figure 1.3: Circuit diagram of the JPA that consists of a CPW resonator short-circuited to ground via a DC-SQUID. The crosses denote Josephson junctions.

We apply boundary conditions on the waves propagating through the transmission line to create a resonator: at one end, the CPW is capacitively coupled with capacitance C_c, which defines the external quality factor and hence the coupling to external fields. At the other end, the CPW is short-circuited to the ground. This creates a quarter-wavelength resonator with electrical length d. The fundamental resonance frequency is given by [50],

$$f_{\text{res}} = \frac{1}{\sqrt{L_{\text{res}} C_{\text{res}}}}, \tag{1.57}$$

where have defined the resonator inductance $L_{\text{res}} = d\, L_0$ and the resonator capacitance $C_{\text{res}} = d\, C_0$. We observe that changing the resonator inductance L_{res} with the application of an external magnetic flux through the DC-SQUID, as in Eq. 1.55, would change the resonance frequency of the JPA. Therefore, the resonance frequency becomes tunable with an external flux.
The resonator can be characterized by its loaded quality factor Q_L, defined as [50]

$$Q_L = 2\pi \frac{\text{average energy stored}}{\text{energy loss per cycle}} = \frac{\omega_{\text{res}}}{\gamma_{\text{int}} + \gamma_{\text{ext}}}, \tag{1.58}$$

where ω_{res} is the angular resonance frequency. The constants γ_{int} and γ_{ext} are the internal loss-rates and the external coupling factor, defined in the previous section. The internal quality factor, $Q_{\text{int}} = \omega_{\text{res}}/\gamma_{\text{int}}$, provides information about internal losses of the resonator. The external quality factor $Q_{\text{ext}} = \omega_{\text{res}}/\gamma_{\text{ext}}$ determines the coupling strength to the signal port, which mainly depends on the coupling capacitance. The loaded, internal and external quality factors are related by

$$Q_L = \frac{Q_{\text{int}} Q_{\text{ext}}}{Q_{\text{ext}} + Q_{\text{int}}}. \tag{1.59}$$

The internal and external quality factors can be extracted by experimentally measuring the complex reflection coefficient of the JPA, as explained in Chapter 3. The full quantum-mechanical model and the Hamiltonian operator used to describe the JPA are presented in Chapter 4.

1.4 Summary

In this chapter, we presented the fundamental theory needed to understand the following chapters of this thesis work. In the first section, we described the theoretical framework needed to describe the physical features of propagating quantum microwaves. We defined the concepts of density matrices and quasi-probability distributions. In the second section, we introduced the tools needed to explore the dynamics of the mode of a microwave cavity. We briefly illustrated the quantum Langevin equation for the field operator and the master's equation for the field density matrix. We concluded the section with a discussion on the numerical techniques used to solve the above-mentioned equations. In the third section, we briefly illustrated the basic theory of Josephson junctions and JPAs.

Chapter 2

Tomographic methods for propagating quantum microwaves

As explained in Chapter 1, the state of a quantum system is a mathematical object that encodes all the information relative to the state, such as density matrices or quasi-probability distributions. In the framework of quantum mechanics, we can reconstruct the state of a quantum system by performing different measurements on many identical copies of the system itself: this procedure is called quantum tomography. For a detailed and formal introduction to this broad field, we refer the reader to Ref. [51].
This chapter is organized as follows: in the first section, 2.1, we schematically introduce the heterodyne detection scheme used in this thesis to perform quantum tomography of propagating quantum microwaves. In the following section, 2.2, we introduce the basic concepts relative to positive operator-valued measures (POVMs) sets related to quantum measurements. In the third section, 2.3, we introduce the iterative maximum likelihood estimation (IMLE) protocol, originally developed by J. Rehacek and Z. Hradil [52]. In the fourth section, 2.4, we show the numerical simulation of the IMLE protocol on the measurement introduced in Sec. 2.1, for a particular state of light. The concluding section of this chapter, 1.5, explores the possible improvements which can be obtained by adding a low-noise cryogenic pre-amplifier in the heterodyne detection scheme.

2.1 Heterodyne dectetion and tomography

The heterodyne detection scheme allows for the simultaneous sampling of two orthogonal quadratures of a propagating quantum microwave signal. In our experiments, the microwave signal consists in the steady-state radiation emitted by a quantum device (either a JPA or a JPC) operating at cryogenic temperatures. The field describing the propagating field is labeled as $\hat{a}$. In order to be detected by room-temperature electronics, the field $\hat{a}$ is amplified by a low-noise phase-insensitive amplifier.

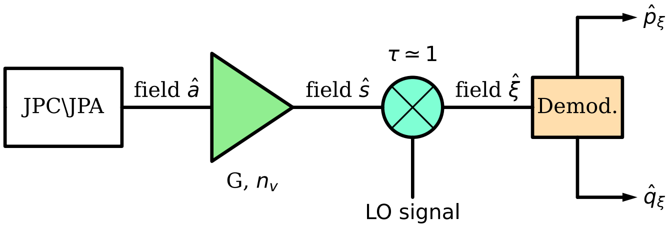

Figure 2.1: Schematic of the heterodyne measurement scheme used in this thesis work. The steady-state field $\hat{a}$ emitted from either the JPC and the JPA is amplified by a phase-insenstive amplifier (green triangle) with gain G and number of noise photons n_v. The resulting mode, $\hat{s}$, is mixed with a strong local oscillator (LO) signal with an LO mixer (blue mixer), which can be modeled as a three ports device with transmissivity $\tau \simeq 1$. The output signal field, $\hat{\xi}$, is digitally demodulated, and the orthogonal quadratures $\hat{q}_\xi$ and $\hat{p}_\xi$, defined in equation 2.7, are measured. The measurement is performed using a field-programmable-gate-array (FPGA) card.

The amplified mode $\hat{s}$ is linked to the output mode of the quantum device, $\hat{a}$, by the relation introduced by Caves in his seminal work Ref. [53],

$$\hat{s} = \sqrt{G}\hat{a} + \sqrt{G-1}\hat{v}^\dagger, \tag{2.1}$$

where G is the total amplification provided by the amplifier and $\hat{v}$ is the thermal field describing the noise photons introduced by the amplification process. The total number of noise photons is defined as

$$n_v = \langle \hat{v}^\dagger \hat{v} \rangle. \tag{2.2}$$

The total number of noise photons is bounded by the Heisenberg uncertainty principle,

$$n_v \geq \frac{1}{2}. \tag{2.3}$$

The signal $\hat{s}$ is mixed to a strong local-oscillator (LO) signal, described by a field $\hat{\ell}$, using an LO mixer. The LO mixer can be modeled as a three ports device which outputs the mode $\hat{\xi}$ given by the linear relation

$$\hat{\xi} = \sqrt{\tau}\,\hat{s} + \sqrt{1-\tau}\,\hat{\ell}, \tag{2.4}$$

where τ is the transmissivity of the mixer. Combining the definitions of $\hat{\xi}$ and $\hat{s}$, we get

$$\hat{\xi} = \sqrt{G\tau}\left(\hat{a} + \sqrt{\frac{G-1}{G}}\,\hat{v}^\dagger + \sqrt{\frac{(1-\tau)G}{\tau}}\,\hat{\ell}\right). \tag{2.5}$$

In our experimental setup, $G \gg 1$ and $\tau \simeq 1$. Therefore, we can approximate the expression for the demodulated mode as

$$\frac{\hat{\xi}}{\sqrt{G}} \simeq \hat{a} + \hat{v}^\dagger. \tag{2.6}$$

In the last equation, we neglected the effect of the mode $\hat{\ell}$ since the prefactor $\sqrt{(1-\tau)/\tau G} \approx \sqrt{1/G} \rightarrow 0$. The mode $\hat{\xi}$ is recorded using a field-programmable-gate-array (FPGA). The sampled trace is then digitally demodulated in its quadrature components. In conclusion, the heterodyne detection scheme measures simultaneously the orthogonal quadratures $\hat{q}_\xi$ and $\hat{p}_\xi$ of the field $\hat{\xi}$, which are defined by the relation

$$\hat{\xi} = \frac{1}{\sqrt{2}} \left(\hat{q}_\xi + \mathrm{j}\hat{p}_\xi\right). \tag{2.7}$$

2.1.1 Tomography from histogram of $\hat{\xi}$

The histogram of the measured mode $\hat{\xi}$ can be used to evaluate the expectation values of the mode $\hat{a}$. Indeed, the histogram of the demodulated quadratures $\hat{q}_\xi$ and $\hat{p}_\xi$ approximates the Husimi Q-function Q_ξ of the mode $\hat{\xi}$. Therefore, it allows us to estimate the anti-normal ordered products of the kind

$$\langle \hat{\xi}^n \hat{\xi}^{\dagger^m} \rangle = \iint_{\mathbb{C}} d\xi \, Q_\xi(\xi) \xi^n \xi^{*^m}, \tag{2.8}$$

where n and m are arbitrary integers. The (n,m)-th anti-normal expectation value of the operator $\hat{\xi}$ can be related to anti-normal expectation values of the operator $\hat{a}$. Indeed, by using 2.6, we derive that

$$\langle \hat{\xi}^n \hat{\xi}^{\dagger^m} \rangle = G^{(n+m)/2} \sum_{k=0}^{n} \sum_{\ell=0}^{m} \binom{n}{k} \binom{m}{\ell} \langle \hat{a}^{n-k} \hat{a}^{\dagger^k} \rangle \langle \hat{v}^{\dagger^{(m-\ell)}} \hat{v}^{\ell} \rangle, \tag{2.9}$$

which is a set of linear equations in the anti-normal expectation values of $\hat{a}$. The linear equation can inverted numerically, and the anti-normal expectation values of the operator $\hat{a}$ can therefore be obtained. From these expectation values, the density matrix ρ_a describing the mode $\hat{a}$ can ideally be derived. To see how this is possible, we start by rewriting the generic anti-normal expectation value $\langle \hat{a}^n \hat{a}^{\dagger^m} \rangle$ in terms of the Husimi Q-function of the mode $\hat{a}$, Q_a,

$$\langle \hat{a}^n \hat{a}^{\dagger^m} \rangle = \iint_{\mathbb{C}} d\alpha \, Q_a(\alpha) \alpha^n \alpha^{*^m}. \tag{2.10}$$

By using the definition of the Husimi Q-function in terms of the density matrix ρ and by expanding ρ in the Fock basis, we obtain a set of linear equations for the entries of ρ, which reads as

$$\langle \hat{a}^n \hat{a}^{\dagger^m} \rangle = \sum_{k,l} \mathcal{A}_{n,m,k,l} \, \rho_{k,l}, \tag{2.11}$$

where

$$\mathcal{A}_{n,m,k,l} = \frac{1}{\sqrt{n!m!}} \iint_{\mathbb{C}} d^2\alpha \, e^{-|\alpha|^2} \alpha^{n+k} \alpha^{*^{m+k}}. \tag{2.12}$$

In conclusion, from the histogram of the mode $\hat{\xi}$, it is in principle possible to derive the density matrix. In practice, this approach has the drawback of requiring the solution of two different linear inversion problems. In particular, equation 2.11 requires the inversion of the four indexes tensor $\mathcal{A}_{n,m,k,l}$, which is a procedure prone to numerical instabilities and errors. In the following, we therefore focus on alternative numerical tomographic techniques, which do not require numerical inversion of large tensors.

2.1.2 Quantum efficiency

In this section, we introduce the concept of quantum efficiency, which is commonly used to quantify the performance of a heterodyne detection scheme. Formally, we define the quantum efficiency η of a heterodyne detection scheme as

$$\eta = \frac{1}{1 + 2n_v}, \tag{2.13}$$

where n_v is the total number of noise photons introduced by the phase-insensitive amplifier. As it is clear from the definition, the quantum efficiency is inversely proportional to the number of noise photons n_v. We observe that, since $n_v \geq 1/2$, the quantum efficiency of a heterodyne detection scheme is bounded as $\eta \leq 1/2$. This limit value $\eta = 1/2$ can be reached by an ideal quantum-limited phase-insensitive amplifier. Physically, this limit arises from the fact that, in a heterodyne detection scheme, we are measuring two orthogonal quadratures, $\hat{q}_\xi$ and $\hat{p}_\xi$, simultaneously, and therefore we are limited by the Heisenberg uncertainty principle; indeed, this limit is not present for detection schemes that involve the measurement of only one quadrature at the time, such as the homodyne detection scheme [54].

2.2 Quantum measurements and POVMs

This section is dedicated to a brief introduction to the formalism of Positive Operator-Valued Measure (POVM) measurements which is necessary to understand the tomographic protocol explained in the following section; for a more complete and in-depth discussion on POVM measurements we refer the interested reader to Ref. [55].

Mathematically, given a Hilbert space $\mathcal{H}$ of dimension D, a POVM is a set of M operators $\left\{\hat{\Pi}_m\right\}_{m=1}^{M}$ acting on $\mathcal{H}$ and satisfying the following properties:

1. each operator $\hat{\Pi}_m$ is a positive operator, which means that $\hat{\Pi}_m$ is self-adjoint and that all the eigenvalues $\left\{\pi_m^{(k)}\right\}_{k=1}^{D}$ of $\hat{\Pi}_m$ are non-negative real numbers;
2. the set of the operators $\left\{\hat{\Pi}_m\right\}_{m=1}^{M}$ is a resolution of the identity operator, id est

$$\sum_{m=1}^{M} \hat{\Pi}_m = \mathbb{I}, \tag{2.14}$$

where $\mathbb{I}$ is the identity operator.

POVM sets are useful because they provide the most general framework to model measurements on quantum states. Indeed, for a measurement with M possible outcomes, labeled as $\{o_m\}_{m=1}^{M}$, we can associate to each outcome o_m a positive operator $\hat{\Pi}_m$. Given an arbitrary quantum state ρ, the probability p_m that an observer measures the outcome o_m can be computed using

$$p_m = \mathrm{Tr}\left(\hat{\Pi}_m \rho\right). \tag{2.15}$$

In general, a POVM set allows to theoretically predict the quantum state of the system after the measurement process is performed on it. Indeed, if the measurement outcome was associated with the operator $\hat{\Pi}_m$, the resulting density matrix can be written as a function of the projector $\hat{\Pi}_m$ associated to the outcome o_m,

$$\rho_m = \frac{\sqrt{\hat{\Pi}_m}\,\rho\,\sqrt{\hat{\Pi}_m}}{\mathrm{Tr}\left(\hat{\Pi}_m \rho\right)}. \tag{2.16}$$

2.3 Iterative maximum likelihood stimation

The main advantage of the iterative maximum likelihood estimation (IMLE), compared to standard maximum likelihood estimation approaches, resides in its numerical efficiency and straightforward implementation; it also has the advantage of being adaptable to any kind of measurement data, as long as the POVM implemented by the measurement scheme is known. This section is organized as follows: in the first subsection 2.3.1, we introduce the essential theory behind this protocol, including its motivation in terms of more general concepts of classical information theory; we provide also the sketch of the algorithm to implement the IMLE protocol. The more formal details are omitted from our treatment: for these details, we refer the interested reader to the original paper in Ref. [52]. The second subsection 2.3.2 describes the statistical and numerical procedure that can be used to estimate the uncertainties on the entries of the reconstructed density matrix.

2.3.1 Description of the protocol

In order to reconstruct the density matrix, the IMLE protocol assumes that many copies of an unknown quantum state have been measured using a set of M measurement operators $\{\hat{\Pi}_j\}_{j=1}^{M}$, which are assumed to form a POVM, with the properties listed in section 2.2. From the repeated measurements, we obtain the outcomes frequencies $\{f_j\}_{j=1}^{M}$, where f_j is the observed frequency of the outcome associated to the operator $\hat{\Pi}_j$.

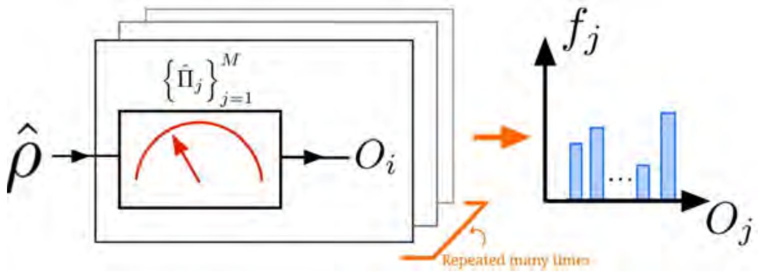

Figure 2.2: Schematic of the quantum measurement process as explained in the main text. An unknown quantum state $\hat{\rho}$ is measured using a POVM $\{\hat{\Pi}_j\}_{j=1}^{M}$. The measurement is repeated many times and the outcomes are stored. Finally, for each possible outcome O_j, we compute the measurement frequency f_j.

For an arbitrary density operator $\hat{\rho}$, the likelihood that $\hat{\rho}$ represents the density operator of the measured state is given by the measured frequencies $\{f_j\}_{j=1}^{M}$ and reads

$$\mathbb{L}[\hat{\rho}] = \prod_{j=1}^{M} \left(p_j[\hat{\rho}]\right)^{f_j}, \tag{2.17}$$

where $p_j[\hat{\rho}]$ is the *a-priori* probability of measuring the outcome associated to $\hat{\Pi}_j$. The *a-priori* probability can be computed according to the Born rule

$$p_j[\hat{\rho}] = \mathrm{Tr}\left(\hat{\Pi}_j \hat{\rho}\right). \tag{2.18}$$

The goal of the IMLE algorithm is to find the density operator $\hat{\rho}_{MLE}$ which maximizes the likelihood. Formally,

$$\hat{\rho}_{MLE} = \underset{\hat{\rho}}{\mathrm{argmax}}\, \mathbb{L}[\hat{\rho}]. \tag{2.19}$$

Why maximizing the likelihood? The idea of maximizing the Likelihood function can be motivated by classical Information Theory. In this context, we are dealing with two discrete probability distributions: the distribution of the measured frequencies $\{f_j\}_{j=1}^{M}$, which we label F, and the unknown distribution of *a-priori* probabilities $\{p_j\}_{j=1}^{M}$, defined in equation 2.18 and which we label P. The problem of reconstructing the most-likely density matrix is mathematically equivalent to the problem of finding the distribution P which shares the most similar statistical content with the distribution F. A possible way to quantify the difference in the information content of two between P and F is by using their Kullback-Leibler divergence. This quantity, first introduced by S. Kullback and R. A. Leibler in Ref [56], is defined as

$$D(F, P) = \sum_{j=1}^{M} f_j \log \frac{f_j}{p_j}. \tag{2.20}$$

The problem of minimizing this quantity with respect to the a-priori probabilities p_j is equivalent to maximizing the term

$$\sum_{j=1}^{M} f_j \log p_j, \tag{2.21}$$

which is just the natural logarithm of the Likelihood defined in equation 2.17.

How to maximize the Likelihood? In order to maximize the Likelihood, we introduce the operator $R(\hat{\rho})$, defined as

$$R(\hat{\rho}) = \sum_{j=1} \frac{f_j}{p_j(\hat{\rho})} \hat{\Pi}_j. \tag{2.22}$$

It can be proved that, starting from an arbitrary initial guess $\hat{\rho}_0$, the succession of density matrices

$$\hat{\rho}_{k+1} = R(\hat{\rho}_k)\hat{\rho}_k R(\hat{\rho}_k) \tag{2.23}$$

has monotonically increasing Likelihood, id est $\mathbb{L}[\hat{\rho}_{k+1}] > \mathbb{L}[\hat{\rho}_k]$. Also, it is important to note that each density operator computed using equations 2.22 and 2.23 is by construction self-adjoint, unit-trace and positive-semidefinite. This feature of the Iterative Maximum Likelihood Estimation protocol ensures that each reconstructed density operator is indeed a physical one. Coming back to equation 2.23, we observe that in the limiting case for which $\hat{\rho_k}$ represents the exact density matrix of the unknown quantum state, the a-piori probabilities coincides with the measured outcome frequencies f_j,

$$f_j = p_j(\hat{\rho}_k) \tag{2.24}$$

and then

$$R = \mathbb{I} \Longrightarrow R(\hat{\rho}_k)\hat{\rho}_k R(\hat{\rho}_k) = \hat{\rho}_k, \tag{2.25}$$

where $\mathbb{I}$ is the identity matrix.

The algorithm The last observations allow us to formulate the algorithm for the Iterative Maximum Likelihood Estimation.

1. We fix a maximum number of iterations N_{max}, a small threshold ϵ and an initial guess for the density matrix to reconstruct. The choices of N_{max} and ϵ depend on the precision we want to achieve on the reconstruction and the numerical complexity we are able to tolerate. In our experiments, we fixed the initial guess to the maximally mixed quantum state of dimension $\mathcal{D}_c$,

   $$\hat{\rho}_0 = \frac{\mathbb{I}}{\mathcal{D}_c}. \tag{2.26}$$

   We also set the iteration number $k = 0$.

2. If $k < N_{max}$, we compute the operator $R(\hat{\rho}_k)$ given the set of measurement operators, $\hat{\Pi}_j$, and the measured frequencies f_j, using equation 2.22.

3. From $R(\hat{\rho}_k)$, we compute the density matrix $\hat{\rho}_{k+1}$, using equation 2.23, and the likelihood $\mathbb{L}[\hat{\rho}_{k+1}]$, using 2.17.
4. If the relative change in Likelihood is smaller than ϵ, *i.e*

$$\frac{\mathbb{L}[\hat{\rho}_{k+1}] - \mathbb{L}[\hat{\rho}_k]}{\mathbb{L}[\hat{\rho}_k} < \epsilon, \tag{2.27}$$

the protocol has converged and outputs the density operator $\hat{\rho}_{k+1}$. If that is not the case, we increase k by one and go back to point 2.

5. If $k = N_{\max}$ the protocol has reached the maximum number of iterations without converging. In this case, it outputs the last obtained density matrix.

Numerical complexity

The algorithm outlined in the last section has been implemented in Python during this thesis work.

As a side note, we also comment on its numerical complexity. The full protocol is repeated, at worse, $N_{\max}$ times; for each iteration, the protocol computes $M + 2$ matrix product: two of them are needed for the estimation of the density matrix ρ_{k+1} and, the other M are needed to evaluate the a-priori probabilities $\left\{p_j\right\}_{j=1}^{M}$. The numerical complexity of each matrix multiplication is $O(D_c^{\mu})$, where μ is a constant between 2.3 and 3 and depends on the algorithmic implementation of the matrix product. Using the Coppersmith-Winograd algorithm [57], $\mu \simeq 2.37$. In conclusion, the whole algorithm has a numerical complexity of

$$O\left(N_{max} \cdot (M+2) \cdot D_c^{2.37}\right) \simeq O\left(N_{max} \cdot M \cdot D_c^{2.37}\right) \tag{2.28}$$

Finally, the complexity of the protocol scales linearly with the number of projectors but as a power with respect to the cut-off dimension of the quantum system D_c. This characteristic makes the protocol more difficult to implement for highly populated quantum systems, wich require larger cut-off dimensions D_c.

2.3.2 Estimation of uncertainties

The goal of this section is to present a simple and robust statistical method to determine the statistical uncertainties δ on the reconstructed density matrix $\hat{\rho}_{MLE}$. We define δ as the matrix of the uncertainties of $\hat{\rho}_{MLE}$, in the sense that the entries δ_{ij}, with i,j integer indeces, represent the statistical uncertainty of the (i,j)th-element of $\hat{\rho}_{MLE}$.

To estimate δ, we follow the method proposed by A. Lvovsky in Ref. [58]. The method proceeds as follows: from the most likely density matrix $\hat{\rho}_{MLE}$, we can generate N sets of simulated measurement data: we label the set of simulated data $\mathcal{S}_1, \ldots \mathcal{S}_N$. In practice, this can be achieved using a random number generator with a probability distribution computed from equation 2.18. From each one of those sets $\mathcal{S}_k$ of simulated data, with $k \in \{1, \ldots, N\}$, we can reconstruct the most-likely density matrix $\tilde{\rho}_k$ using the IMLE protocol outlined above. In general, $\tilde{\rho}_k$ will be slightly different from $\hat{\rho}_{MLE}$. Then, from the simulated density matrices $\left\{\tilde{\rho}_k\right\}_{k=1}^{N}$, we can finally estimate the statistical uncertainties on $\hat{\rho}_{MLE}$ by computing the average of the errors

$$\delta = \frac{1}{N}\sum_{k=1}^{N}\left(\rho_{MLE} - \tilde{\rho}_k\right). \tag{2.29}$$

2.3.3 IMLE applied to heterodyne detection

In this section, we describe the IMLE tomography method applied to the heterodyne detection scheme introduced in section 2.1. The goal of this section is to present a numerically useful expression for the POVM $\left\{\Pi_j\right\}_{j=1}^{M}$ for the heterodyne detection. In particular, we derive an expression for the POVM which depends only on the experimental parameters that characterize the detection scheme: the total gain of the amplification chain G and the number of noise photons introduced by the amplification process n_v. In terms of quasi-probability distributions, equation 2.6 allows to express the Q-function of the measured mode Q_ξ as the complex-plane convolution between the P-function of the noise mode P_v and the Q-function of the quantum signal mode Q_a. In the high-gain limit, the convolution, proved by M.S. Kim in [59], reads as

$$Q_\xi(\beta) = \frac{1}{G}\int_{\mathbb{C}} d^2\alpha\, P_v\left(\frac{\beta}{\sqrt{G}} - \alpha\right) Q_a(\alpha), \tag{2.30}$$

where $P_v(\alpha) = \mathcal{N}\exp\left(-|\alpha|^2/n_v\right)$ is the Glauber-Sudarshan P-function for the noise mode $\hat{v}$. In the heterodyne detection scheme, the sampled quadrature operators have a continuous spectrum and the POVM is given by a continuous set of hermitian operators $\hat{\Pi}(\beta)$ satisfying

$$\int_{\mathbb{C}} d^2\beta\, \hat{\Pi}(\beta) = \mathbb{I}, \tag{2.31}$$

where the integration is extended to th whole complex plan. To obtain an expression for $\hat{\Pi}(\beta)$, for $\beta \in \mathbb{C}$, we start rewriting equation 2.30 by replacing the definition of Q_a in terms of the unknown density operator $\hat{\rho}_a$ of the quantum mode. We obtain

$$Q_\xi(\beta) = \frac{1}{\pi G}\mathrm{Tr}\left(\hat{\rho}_a \int_{\mathbb{C}} d^2\alpha\, P_v\left(\frac{\beta}{\sqrt{G}} - \alpha\right)|\alpha\rangle\langle\alpha|\right). \tag{2.32}$$

Comparing equation 2.32 to the general equation for the *a-priori* probabilities 2.18, we identify

$$\hat{\Pi}(\beta) = \frac{1}{\pi G}\int_{\mathbb{C}} d^2\alpha\, P_v\left(\frac{\beta}{\sqrt{G}} - \alpha\right)|\alpha\rangle\langle\alpha|. \tag{2.33}$$

Using the definition of the P-function presented in Chapter 1, the expression 2.33 for the measurement operator $\hat{\Pi}(\beta)$ can be rewritten as

$$\hat{\Pi}(\beta) = \frac{1}{G\pi}\hat{D}\left(\frac{\beta}{\sqrt{G}}\right)\hat{\rho}_\nu\hat{D}^\dagger\left(\frac{\beta}{\sqrt{G}}\right). \tag{2.34}$$

Since the noise mode occupies a thermal state, the equation 2.34 relies on just two parameters to be determined experimentally: the average noise mode photon occupation $\bar{n}_\nu$ and the amplification chain gain G. In practice, both are extracted from the *planck-spectroscopy* measurement, explained Chapter 3.

2.4 Numerical simulation of heterodyne protocol

This section summarizes the results obtained by implementing the Iterative Maximum Likelihood Estimation reconstruction protocol, using the heterodyne detection POVM 2.34, on a set of simulated measurement data. We simulate the protocol against a state belonging to the family of even cat-states $\left|C^+(\beta)\right\rangle$, defined as

$$\left|C^+(\beta)\right\rangle = \mathcal{N}\left(\left|\beta\right\rangle + \left|-\beta\right\rangle\right), \tag{2.35}$$

where $\mathcal{N}$ is a normalization factor and $\left|\beta\right\rangle$ is a coherent state. Without loss of generality, we considered the case $\beta \in \mathbb{R}$. The reason for this choice is that *cat-states* are quantum states with rich features such as reflection symmetry in the phase space, Wigner negativity, and interference fringes in the phase-space, as shown in Figure 2.3. Therefore, these states can be used as a good benchmark to test the capabilities of the designed reconstruction protocol. In particular, we choose an even cat state corresponding to $\beta = 1.5$. This choice is motivated by the fact that the photon number of the even cat state $\left|C(\beta = 1.5)\right\rangle$ is still low enough to not introduce any numerical overhead in the simulation.

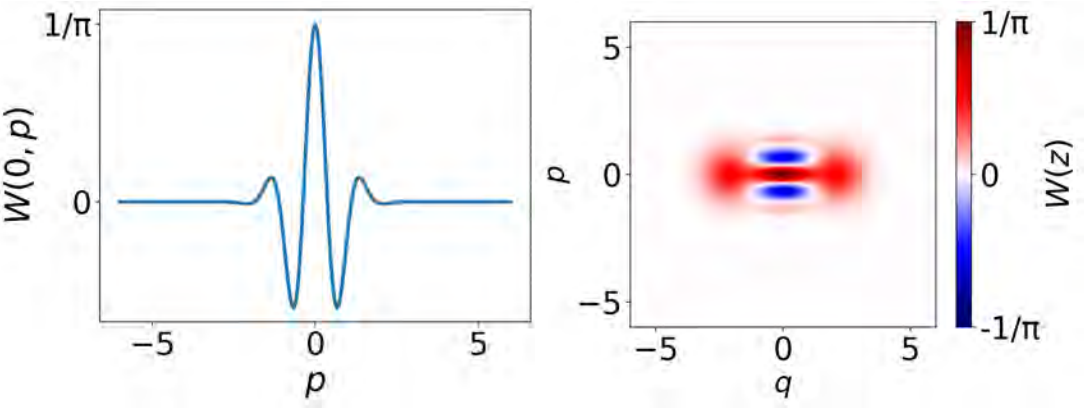

(a) (b)

Figure 2.3: (a) Cross section of the Wigner function $W(z)$ of the target state $\left|C^+(1.5\right\rangle$. (b) Wigner function $W(z)$of the target state $\left|C^+(1.5\right\rangle$.

2.4.1 Simulation of measurement outcomes

To simulate the protocol, we first need to store in an efficient and accurate way the information encoded in the density matrices and phase-space distributions. For this, it is necessary to

1. Fix a cut-off dimension for the infinite-dimensional Hilbert space for quantum states of light, which we label D_c. Since the quantum mechanical properties of density matrices are independent of the chosen basis, we conventionally choose to work in the *Fock-states* basis. In this way, the generic (n, m)-th element of a density matrix ρ is given by

$$\rho_{n,m} = \langle n|\rho|m\rangle, \tag{2.36}$$

   where $n, m \in \{1, \dots, D_c\}$.

2. Discretize the axes q and p of the phase space. Then, it is necessary to fix
   a) a cut-off for of both axes, which we label as L;
   b) a discretization step $\Delta\ell$.

   The discretized axes are labeled respectively as $\vec{q}$ and $\vec{p}$.

3. Given the discretizations of the q and p- axes of the phase-space, the discretized phase space, labeled as $\mathcal{S}$, is given by the cartesian product of $\vec{q}$ and $\vec{p}$ defined as

$$\mathcal{S} = \{(q_n, p_m) \text{ such that } q_n \in \vec{q}, p_m \in \vec{p}\}. \tag{2.37}$$

   $\mathcal{S}$ is then a grid of N^2 cells each one of area $\Delta\ell^2$.

Determination of D_c As explained in Chapter 1, D_c is fixed by the requirement that

$$D_c \gg \bar{n} \tag{2.38}$$

where $\bar{n}$ is the average photon occupation of the target state we want to analyze. For even cat states $\left|C^+(\beta)\right\rangle$,

$$\bar{n}(\beta) = |\beta|^2 \frac{1 - e^{-2|\beta|^2}}{1 + e^{-2|\beta|^2}}, \tag{2.39}$$

and then $\bar{n} \approx 2.2$ for the even cat-state with $\beta = 1.5$. To make the condition expressed in equation 2.38 more quantitative, we study how the numerical estimated average photon number population of the target state, labeled as $\tilde{n}$, compares to the exact analytical value, $\bar{n} = 2.20$, for different cut-off dimensions D_c. In particular, we use the logarithmic error

$$\log_{10}\delta = \log_{10}|\bar{n} - \tilde{n}(D_c)|, \tag{2.40}$$

as a figure of merit. The numerical simulation, summarized in Fig. 2.4, indicates that, when the cut-off dimension is $D_c = 12$, $\log_{10}\delta \approx -4$, which is good enough for the scope of the following discussion.

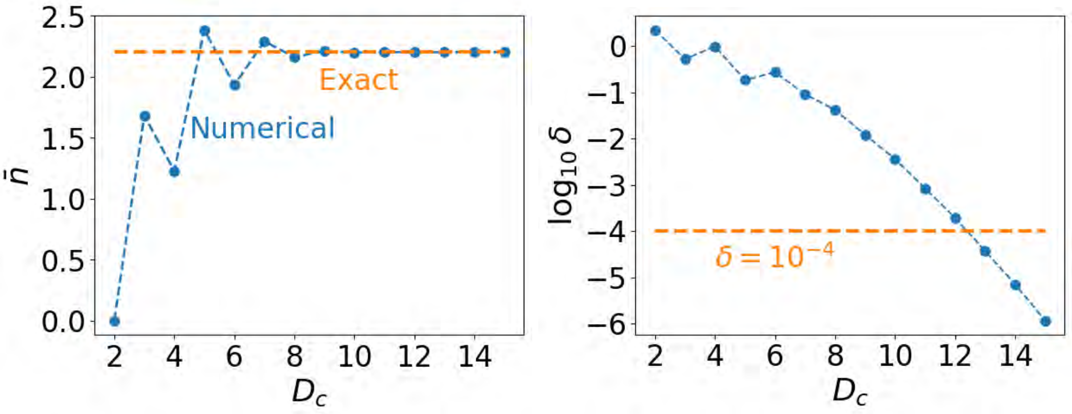

(a) **(b)**

Figure 2.4: (a) Numerical estimated (blue markers) photon population of the target state $|C^+(1.5)\rangle$ as function of the cut-off dimension D_c versus the exact analytical estimation obtained from equation 2.39. (b) Logarithmic error as a function of the cut-off dimension D_c. We note that when $D_c = 12$, the error is approximately 10^{-4}.

Determination of L and $\Delta\ell$ Once we have determined the cut-off dimension D_c, we determine the cut-off length for q and p-axes, L. This quantity is chosen to discretize only the relevant part of the phase space. We start by numerically evaluating the marginal distributions along the axes q and p, which we label respectively $F_1(q)$ and $F_2(p)$, for the target cat-state $|C^+(1.5\rangle$. Those are defined as

$$\begin{aligned} F_1(q) &= |\langle q|C^+(1.5)\rangle|^2 \\ F_2(p) &= |\langle p|C^+(1.5)\rangle|^2, \end{aligned} \tag{2.41}$$

where $|q\rangle$ and $|p\rangle$ are respectively the eigenvectors of the position operator $\hat{q}$ and the momentum operator $\hat{p}$. The two functions can be computed using the built-in functions of the open-source python package "QuTiP" [41], which provides several numerical routines for quantum optics. After the computation of F_1 and F_2, we evaluate the logarithms $\log_{10} F_1(q)$ and $\log_{10} F_2(p)$, as shown in Figure 2.5. We observe that, when $|q| > 6$, we have $\log_{10} F_1(q) < -8$ and when $|p| > 4$, we have $\log_{10} F_2(p) < -7.5$. This means that there is almost no quantum information encoded in the region of the phase space in which $|q| > 6$ and $|p| > 4$. For this reason, we fix the cut-off L for both axes to $L = 6$. Given the choice of L, we set the discretization step for the axis $\Delta\ell = 0.4$, in order to discretize the phase space in $30 \times 30 = 900$ cells. The value of $\Delta\ell$ is big enough to implement efficiently the protocol.

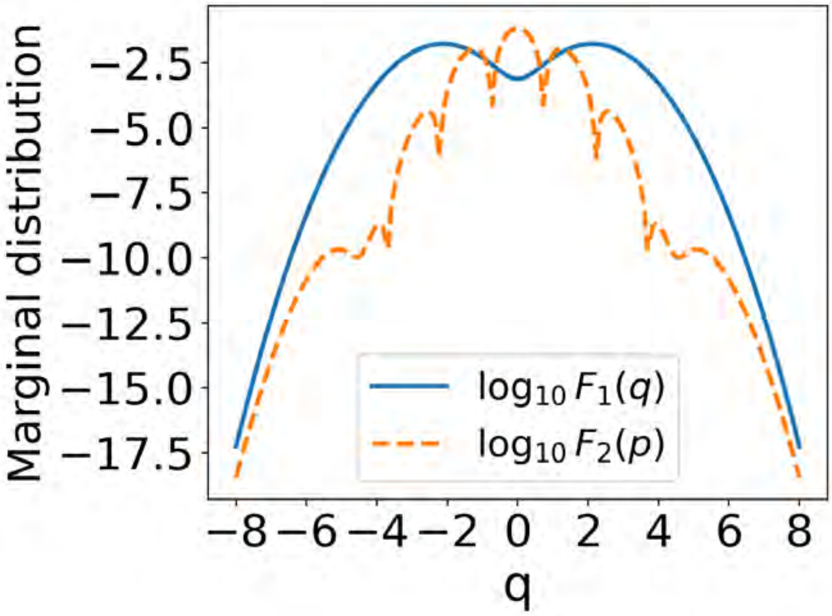

Figure 2.5: Base-10 logarithm of the marginal distributions along q axis (blue solid line) and p axis (orange dashed line) for the even cat state $\left|C^+(\beta)\right\rangle$ with $\beta = 1.5$.

Simulation of heterodyne measurement To test the IMLE tomographic protocol, we need a set of simulated measurements corresponding to the POVM defined in 2.34. In this section, we describe how to obtain a set of measurement data which simulates the heterodyne detection scheme described in 2.1. The procedure is the following:

1. we compute the truncated density matrix ρ_0 of dimension $D_c \times D_c$, where $D_c = 12$, corresponding to the target state $\left|C^+(\beta)\right\rangle$ with $\beta = 1.5$. The density matrix encodes the information relative to the target state in the Fock states basis;

2. from the discretized axes size L and spacing $\Delta\ell$, which were determined in the previous section, we build the discretized phase-space grid $\mathcal{S}$;

3. we set the values for the amplifier gain G and the photon noise number n_ν. For each point $\beta_{n,m} = q_n + ip_m$ in the discretized phase-space $\mathcal{S}$, we compute the associated projector $\hat{\Pi}_{n,m} = \hat{\Pi}(\beta_{n,m})$ using equation 2.34;

4. for each point $\beta_{n,m}$ in the discretized phase-space $\mathcal{S}$, we compute the a-priori probability $P_{n,m}$ of measuring the quadratures q_n and p_m at the same time. This probability is computed using the Born rule

$$P_{n,m} = \mathrm{Tr}\left(\Pi_{n,m}\rho_0\right). \tag{2.42}$$

   These probabilities are stored in a matrix P;

5. using a (pseudo-)random number generator, we can extract a couple of integer numbers (n,m) from the probability distribution defined by the matrix P. The element of the

discretized phase-space $\mathcal{S}$ with indeces (n,m) is the outcome of the simulated heterodyne detection. One possible choice as a random number generator is "rv discrete", included in the open-source library "SciPy" [60].

The full set of measured phase-space points can be obtained by repeating the quantum measurement process (random number generation) a large number of times. In our simulation, we set this number 10^6.

2.4.2 Discussion of simulation results

In this section we discuss the results obtained by numerically simulating the IMLE protocol for the heterodyne detection scheme described in the previous sections. For our simulation, we used the following numerical parameters:

Parameter	Value
β	1.5
D_c	12
$\Delta\ell$	0.4
L	6
N^2	900

The estimation of all these parameters was explained in the previous sections. The simulation was performed by fixing the gain G and then sweeping the quantum efficiency η from the minimum value, 0%, to the maximum value, 50%. The gain G was then varied from 10 dB to 40 dB. For every couple of values (η, G) we simulated the reconstruction protocol using 10^6 measurements, obtaining each time a different reconstructed density matrix $\rho(\eta, G)$. From any reconstructed matrix $\rho(\eta, G)$, we

1. reconstructed the Wigner function $W_{\eta,G}(z)$ in the discretized phase-space;
2. computed the fidelity $F(\eta, G)$ with respect to the target state $\left|C^{+}(\beta)\right\rangle$;
3. computed the negative volume $V_N(\eta, G)$.

The IMLE protocol is implemented by setting maximum number of iterations to 30 and the numerical parameters for the protocol termination ϵ to 10^{-4}. First, we look at the simulated results for the *Fidelity* $F(\eta, G)$. The results are plotted in Figure 2.6.

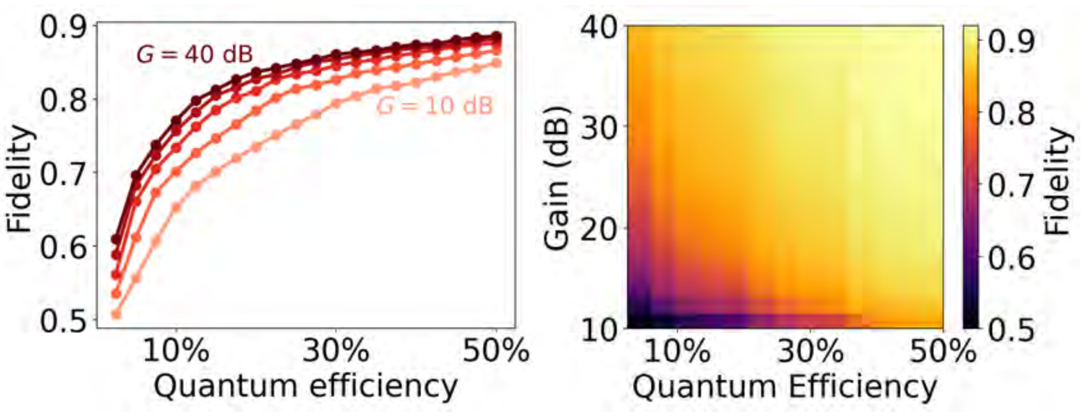

(a) **(b)**

Figure 2.6: (a) Fidelity of the reconstructed density matrix as function of the quantum efficiency η for different gain G values. The darkest the shade of red of the curve, the highest G. (b)Same data but summarized in a color-map.

First, we observe that, for any value of η, $F(\eta, G)$ increases by increasing the Gain G; this increase gets noticeably less important for higher values of the quantum efficiency η. For instance, we observe that when $\eta = 10\%$ and $G \approx 10$ dB, the Fidelity of the reconstructed state is $F \approx 60\%$. Keeping fixed the value of η, but increasing G to 40 dB hields a Fidelity $F > 70\%$. Instead, when the $\eta \approx 30\%$, the Fidelity jumps from $F \approx 75\%$ ($G = 10$ dB) to $F \approx 80\%$ ($G = 40$ dB). When $\eta \to 50\%$, the Fidelity approaches 90%, for all values of the Gain G. When η goes to 0%, the reconstructed state is just thermal noise; in this case, the Fidelity does not drop to zero, because the thermal noise mode has a finite overlap with the target-state $\left|C^{+}(1.5)\right\rangle$.

We also measure the negative volume V_N as a function of η and G. The negative volume is measured to benchmark the ability of the protocol to reproduce non-classical features of the observed mode of light. The results for the negative volume V_N are plotted in Fig. 2.7. The negative value shows qualitatively the same trend of the Fidelity. In particular, for every set value of the quantum efficiency η, the reconstructed negative volume is an increasing function of the gain G provided by the amplification chain. In Fig. 2.8, we show the reconstructed Wigner functions for the target state $\left|C^{+}(1.5)\right\rangle$, for different values of the parameters G and η used in our simulations. The reconstructed Wigner functions show the same features of the exact Wigner function: phase-space symmetry, Wigner negativity and interference fringes.

2.5 Improve quantum efficiency using a pre-amplifier

In this section, we briefly review a possible solution that can be used in order to improve the quantum efficiency of a heterodyne detection scheme.

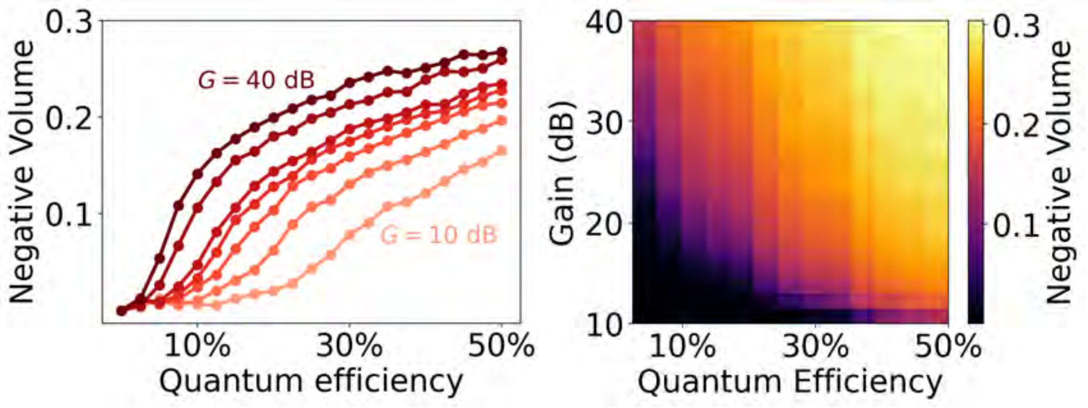

(a) **(b)**

Figure 2.7: (a)Negative volume of the reconstructed density matrix as function of the quantum efficiency η for different gain G values. The darkest the shade of red of the curve, the highest G. (b)Same data but summarized in a color-map.

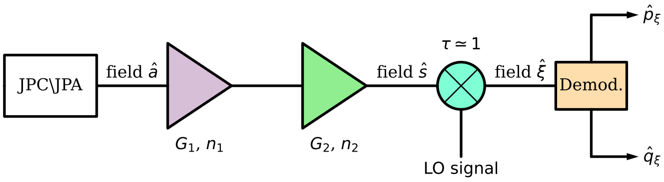

Figure 2.9: Modified heterodyne detection scheme including the pre-amplifier (purple triangle).

To improve the quantum efficiency of the heterodyne detection scheme, a possible solution consists in introducing a low-noise cryogenic pre-amplifier. The heterodyne detection is modified as shown in Figure 2.9. We label G_1 and G_2 the gains of the pre-amplifier and the amplifier respectively. In an analogous way, n_1 and n_2 indicate the number of noise photons introduced by the pre-amplifier and the amplifier respectively. To understand the modifications due to the presence of the pre-amplifier, we start by noting that, in experiments, $G_2 \approx 30 - 40$ dB usually. In this case we can assume that $(G_2 - 1)/G_2 \approx 1$ and then the output mode $\hat{\xi}$ can be approximated as

$$\hat{\xi} \approx \sqrt{G_1 G_2}\left(\hat{a} + \sqrt{\frac{G_1 - 1}{G_1}}\hat{v}_1^\dagger + \frac{\hat{v}_2^\dagger}{\sqrt{G_1}}\right), \tag{2.43}$$

where $\hat{v}_1$ and $\hat{v}_2$ are the noise modes of the pre-amplifier and the amplifier respectively. The last equation implies that the setup with the pre-amplifier can be modeled as a single effective phase-insensitive amplifier with total gain $G_1 \cdot G_2$ and noise mode $\hat{v}_T^\dagger$ given by

$$\hat{v}_T^\dagger = \sqrt{\frac{G_1 - 1}{G_1}}\hat{v}_1^\dagger + \frac{\hat{v}_2^\dagger}{\sqrt{G_1}}, \tag{2.44}$$

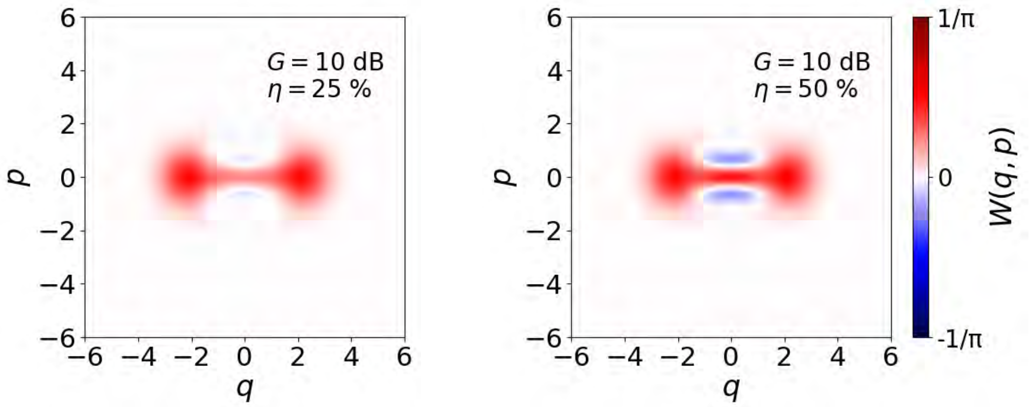

(a) $G = 10$ dB, $\eta = 0.25$ **(b)** $G = 10$ dB, $\eta = 0.5$

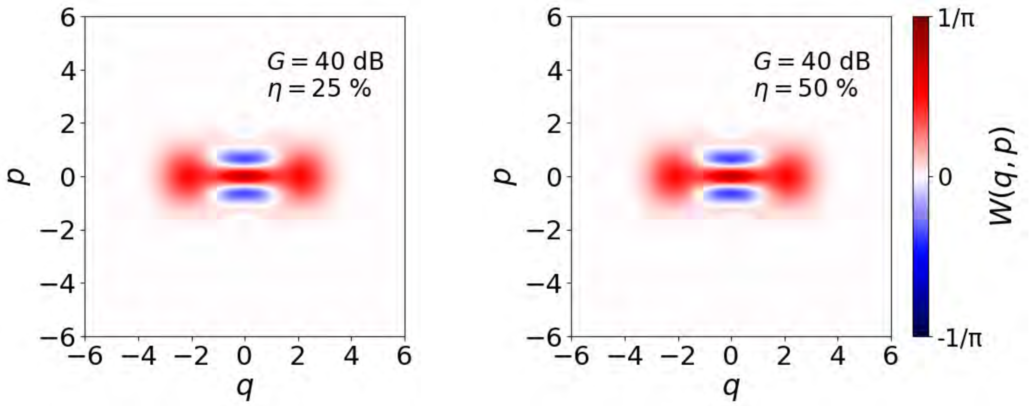

(c) $G = 40$ dB, $\eta = 0.25$ **(d)** $G = 40$ dB, $\eta = 0.5$

Figure 2.8: Wigner function of the target state reconstructed for different values of η and G.

The noise mode $\hat{v}_T^\dagger$ has a total noise photon population given by

$$n_T = \langle \hat{v}_T^\dagger \hat{v}_T \rangle = \frac{G_1 - 1}{G_1} n_1 + \frac{n_2}{G_1}. \tag{2.45}$$

In the limit of large pre-amplifier gain, $G_1 \to \infty$, we have $n_T \to n_1$, and then the total quantum efficiency reaches asymptotically the quantum efficiency of the pre-amplifier. The pre-amplifier improves the measurement noise properties if, by definition, $n_T < n_2$, which means $\eta_T > \eta_2$, i.e. the total quantum efficiency with the pre-amplifier is bigger than the quantum efficiency of the second amplifier alone. From equation 2.45, we see that this condition is verified when

$$\frac{G_1 - 1}{G_1} (n_1 - n_2) < 0. \tag{2.46}$$

Therefore, if the pre-amplifier is less noisy than the second amplifier, for any pre-amplifier gain $G_1 > 1$ (in linear units), the pre-amplifier improves the noise properties of the measurement setup.

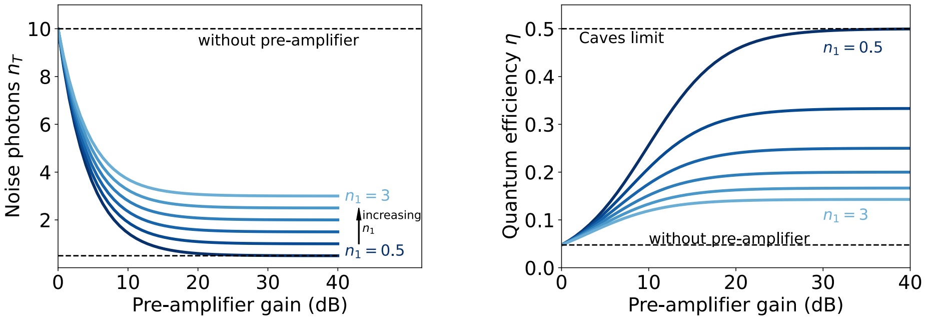

(a) **(b)**

Figure 2.10: (a)Total number of noise photons n_T as function of the pre-amplifier gain G_1 (measured in dB) for different values of the preamplifier quantum efficiency η_1. (b) Quantum efficiency of the whole setup η_T as a function of the pre-amplifier gain G_1 for different values of the preamplifier quantum efficiency η_1. For both plots, we assumed that the noise introduced by the second amplifier is $n_2 = 10$. The preamplifier quantum efficiency η_1 is ranged from 14% (light blue line) to 50% (dark blue line).

2.6 Summary

In this chapter, we described the techniques used to perform quantum tomography on propagating quantum microwaves. In the first section, we explained the details on the heterodyne detection scheme; in the second one, we briefly introduced the concept of POVM applied to quantum measurements. In the third section, we described the iterative maximum likelihood detection scheme applied to the heterodyne detection scheme. In the third section, we simulated the IMLE protocol for the heterodyne measurement scheme for the even cat-state $\left|C(\beta)\right\rangle$ with $\beta = 1.5$. We concluded the chapter by explaining the possible improvements that can be obtained by adding a low-noise cryogenic pre-amplifier in a heterodyne detection scheme.

Chapter 3

Experimental techniques

In this chapter, we focus on the experimental techniques used throughout this work to generate and measure weak quantum microwaves. In the first section, 3.1.1, we describe the setup used in our experiments, focusing on both the cryogenic and room-temperature components. In the following section, 3.2, we explain how quantum microwaves are detected and how the effects of the amplification chain effects taken in to account. The last section, 3.4, concludes the chapter with a description of the necessary measurements to properly calibrate the superconducting devices used in our setup.

3.1 Cryogenic setup

In this section, we describe the cryogenic experimental setup used during this master's thesis. In the first subsection, we briefly explain the working principle of the dilution cryostat which was used to reach the low temperatures required for generating propagating quantum microwaves. Then, we illustrate the samples used for our experiments. Lastly, we talk about the input and output lines connected to our setup.

3.1.1 Dilution cryostat

To generate propagating quantum microwaves we need ultra-low temperatures. To this end, we use a ^{3}He/^{4}He dilution cryostat, which was designed and built at the Walther-Meissner-Institut. A photo image of the cryostat is shown in Fig. 3.1. This cryostat reaches around 40 mK at the sample stage. Such low temperatures are necessary to avoid the effects of thermal noise photons. Indeed, the thermal photon occupation for a signal at the carrier frequency f in the thermal equilibrium with temperature T can be computed from the Planck equilibrium distribution [61]

$$\bar{n} = \frac{1}{e^{hf/k_bT} - 1}, \tag{3.1}$$

where h is the Planck constant and k_b is the Boltzmann constant. The equation 3.1 computed for $T = 40$ mK and $f = 5$ GHz gives $\bar{n} \leq 2 \times 10^{-4}$. The cryostat is enclosed by a metallic dewar. The dewar is filled with liquid nitrogen (77 K) and liquid helium (4.2 K), which are separated by vacuum layers. The helium and nitrogen reservoirs provide a temperature of 4 K for the inner vacuum chamber (IVC). During our experiments, the pressure in the IVC chamber was

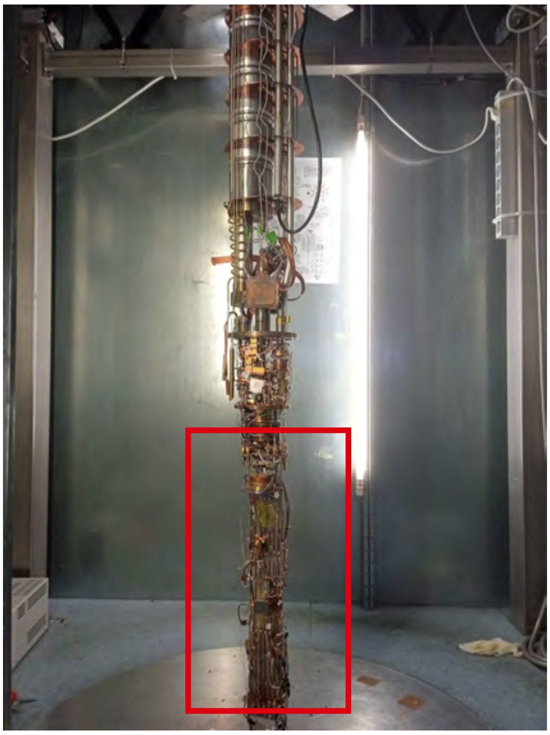

Figure 3.1: Photo image of the dilution cryostat with the experimental setup mounted. The sample stage is indicated by the red box.

measured to be below 10^{-4} mbar. The mixture is further cooled by the 1K pot, still, continuous, and step heat exchangers, before entering the mixing chamber (MXC), which is the coldest stage of the cryostat. In the MXC, the two phases of the mixture, i.e. the concentrated phase with pure ^{3}He and the diluted phase with 6.6% ^{3}He and 93.4% ^{4}He, coexist and are physically separated because of their different densities. From the bottom of the MXC, a tube connects the diluted phase to the still. The still has a temperature of around 700 mK and is pumped by a turbomolecular pump (TMP). In the MXC, the ^{3}He evaporates much faster than the ^{4}He in the diluted phase. In order to keep the balance between the two phases, part of the ^{3}He in the concentrated phase is resolved in the diluted phases. This process absorbs heat from the environment and cools down the MXC to about 40 mK. A more detailed description of the structure and working principle of the dilution cryostat can be found in Ref. [1]. An illustration of the dilution cryostat is shown in Fig. 3.2.

3.1.2 Sample stage

The sample stage is attached to the MXC. The schematic corresponding to the sample stage is reported in Fig. 3.4. A photo image of the sample state is shown in Fig. 3.3. The input line A22, described in 3.1.3, is connected to a coaxial switch (N1812UL from Keysight). By default, the switch is in the state "A", in which the signal from the input line goes into a 4 − 8 GHz circulator (CIC4-8A from Low Noise Factory) and then enters a Josephson parametric converter (JPC), which was operated in a one-port configuration. The signal reflected from the JPC is

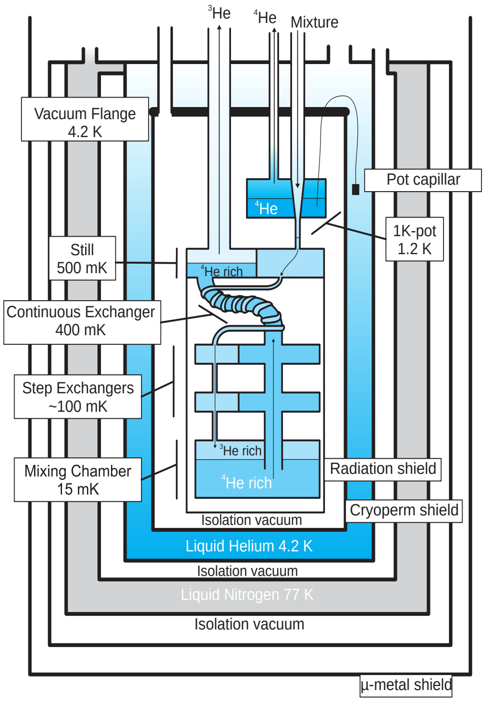

Figure 3.2: Scheme of the wet dilution cryostat used in our experiments. The drawing was realized by M. A. A. Caballero and was originally included in Ref. [1]

filtered by a low-pass filter (DC-6400 MHz mini-circuits VLF 6400+). The low-pass filter is connected to another circulator. The signal port of a Josephson parametric amplifier (JPA) is connected to the circulator as illustrated in Fig. 3.4. The pump port of the JPA is connected to an SGS100A microwave source, which provides the pump signal at twice the JPA frequency. The pump signal flows through the A20 input line

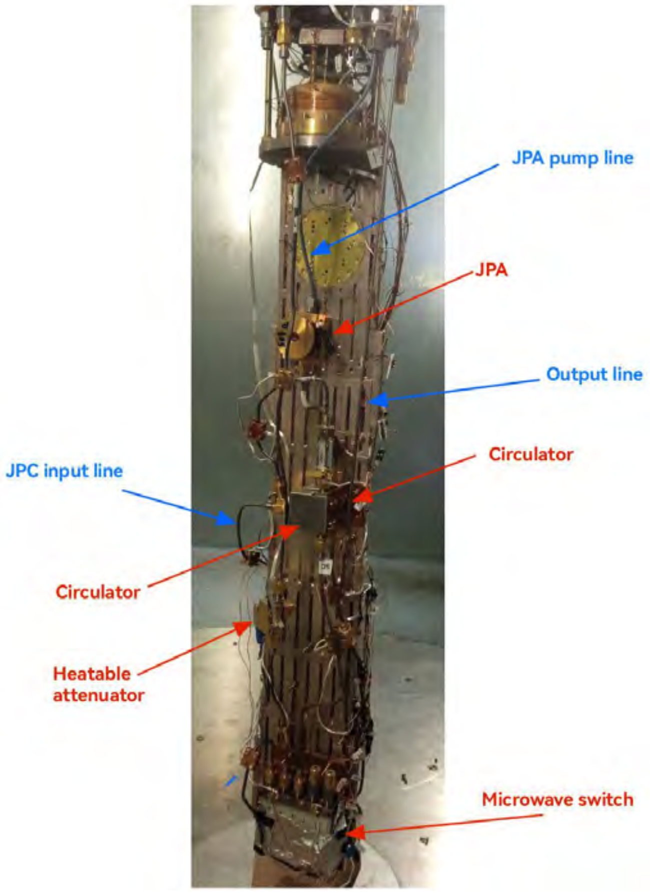

Figure 3.3: Photo image of the sample-stage cryogenic setup.

All connections at the sample stage level, with the exception of the pump cable for the JPA, are implemented using superconducting cables (SC-219/50- NbTi-NbTi) manufactured by Coax Co., Ltd [62]. These cables have an inner conductor and outer conductor made of niobium titanium (Nb-Ti), while the dielectric layer is made of polytetrafluoroethylene (PTFE). The outer conductor has a diameter of 2.19 mm. Due the superconducting properties of NbTi, such cables have low microwave losses at cryogenic temperatures. Indeed, the datasheet estimates an expected attenuation smaller than 0.3 dB/m for frequencies ranging from DC to 20 GHz. The cable that transports the pump signal for the JPA is a minibend cable manufactured by HUBER+SUHNER [63]. This cable has an attenuation of 2 dB/m for signals at frequency 10 GHz. All the microwave components and the superconducting devices are additionally thermalized by using silver wires connected to the mixing chamber. These wires are bent into suitable shapes and annealed at 900°C to improve their heat conductivity.

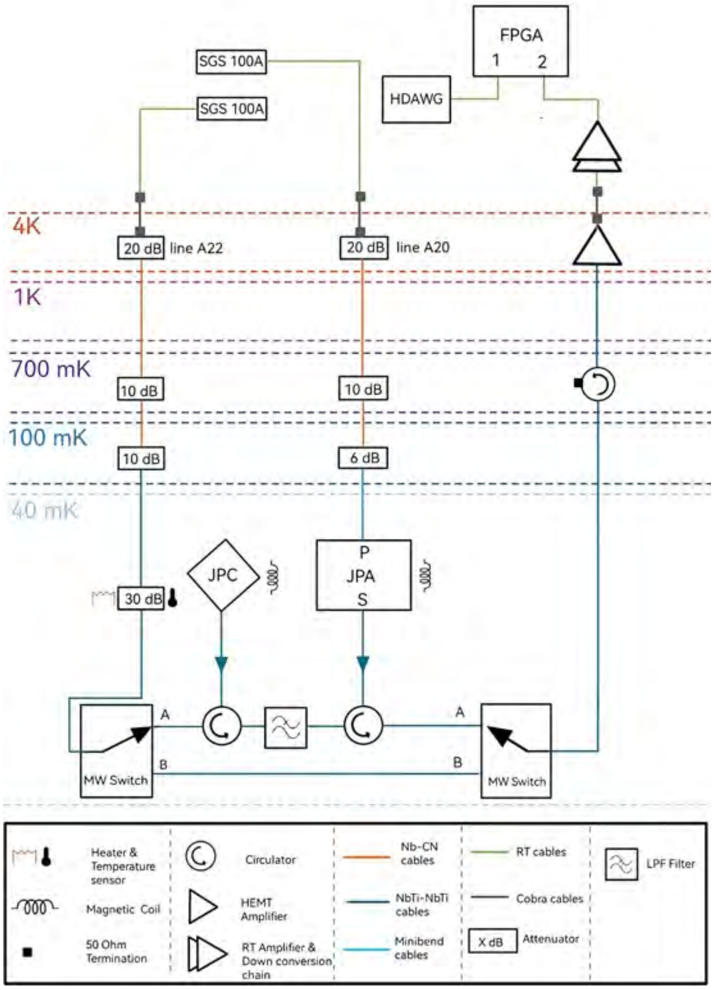

Figure 3.4: Full experimental setup used in our experiments. All devices are referenced to a rubidium frequency standard (not shown). Two magnetic coils set on top of both the JPA and the JPC. The magnetic coils allow to change the resonance frequencies of both devices by changing magnetic flux trough them. Both coils are connected to a room-temperature dirrect current generator (not shown). The structure of the down-conversion chain is explained in detail in the following sections.

Devices

During this thesis work, we use two superconducting devices designed and fabricated in-house: a JPC and a JPA. In this section, we discuss how these devices are connected inside of our experimental setup. The devices, as shown in Fig. 3.5, are placed inside two sample boxes. On top of each sample boxe, we a superconducting magnetic coil is attached. Each coil is connected to an ADCMT 6241A high-precision direct current source. The current sources have a resolution of 1 nA and are used to tune the frequency of both superconducting devices by generating magnetic flux trough the corresponding DC-SQUIDs. Moreover, he JPC is placed in an aluminum shield to protect it from the unwanted effects of the magnetic fields generated by the magnetic coil attached to JPA. The shield is then covered with an aluminum foil to completely cover the device. The JPC chip, 3.6, is made of a Josephson ring modulator (JRM) which is a loop of four nominally identical Josephson junctions shunted by four linear geometric inductances. The JRM is connected to two superconducting microwave resonators. In our experiments, the JPC is operated in a single port configuration, which means that only one of the two superconducting resonators is connected to the external environment. The JPC, which can be used as a three-wave mixing device, is described in great detail in Ref. [64].

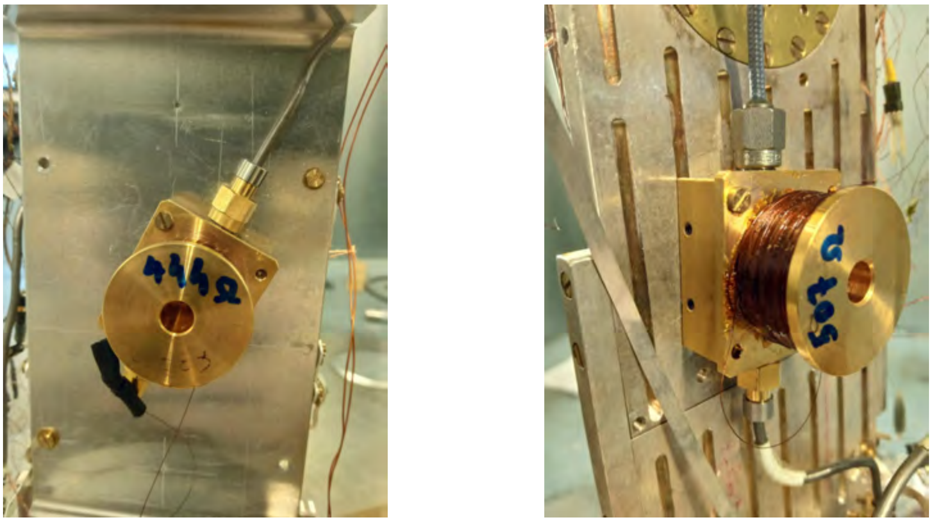

(a) Photo of the connected JPC sample-box.

(b) Photo of the connected JPA sample-box.

Figure 3.5: Panel (a) shows a photo of the sample box containing the JPC. The device is connected in a single port configuration to the input line A22. Panel (b) shows a photography of the sample box containing the JPA. The JPA is connected to the pump line (input line A20) with a minibend cable at the top of the photo and to the signal line, lower part of the photo, with a superconducting NbTi cable.

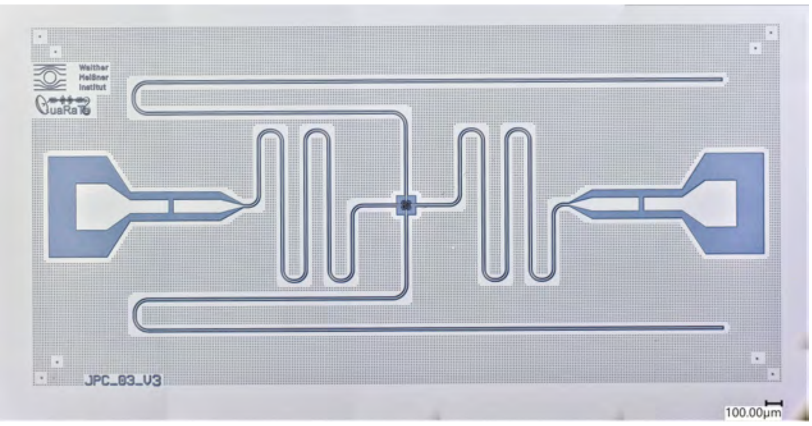

Figure 3.6: Photo image of the JPC Chip.

The JPA chip, showed in Figure 3.7, is made by a $\lambda/4$ microwave resonator short-circuited with a DC-SQUID to the ground. The DC-SQUIDs are be used to tune the JPA and JPC frequencies as explained in section 1.3.

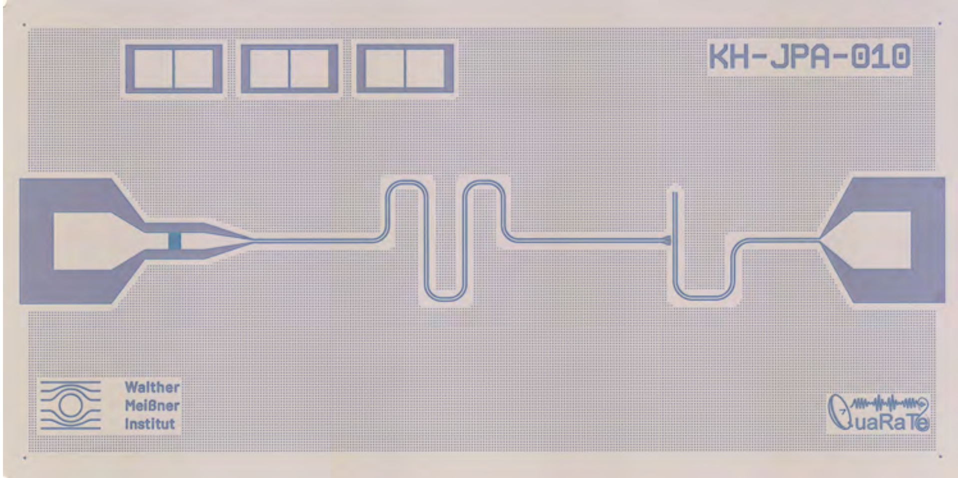

Figure 3.7: Photo image of the JPA chip.

3.1.3 Input and output lines

Input lines

Our setup uses two input lines. Up to the 4K stage, we use astrocobra-flex 31086S cables (from HUBER+SUHNER). The connection from the 4K stage to the 100 mK Stage is made using coaxial cables with internal and outer conductors made of niobium and cupronickel Nb-CN. In ordert to gradually suppress the thermal noise coming from the environment external to the cryostat, several attenuators are placed in the input line. In particular, for the input line A22, we have a total of 70 dB of attenuation distributed along the different temperature stages to protect the sample stage from external thermal noise. We note that the input line used for the pump signal (A20) of the JPA has a much lower attenuation (36 dB) in order to allow for high pump powers being applied to the device.

Output lines

As showed in Figure 3.4, the setup has only one output line. To minimize the losses, the connection up to the first amplifier, which lies in the 4K stage, is made using two NbTi/NbTi coaxial cables. Before entering the amplifier, the signal passes through 4-8 GHz circulator (LNF-CIC4-8A from Low Noise Factory). One port of the circulator is terminated with a 50Ω load. The load is thermalized by connecting it to the cryostat with an annealed silver cable. The circulator used in this configuration allows the quantum signal coming from the sample stage to propagate with a small insertion loss (0.3 dB) and suppresses the signals coming from the other direction (21 dB isolation). After the circulator, the signal is amplified by a high electron mobility transistor (HEMT) amplifier, which was manufactured by TTI. This HEMT amplifier has a specified gain of 40-44 dB in the 4-8 GHz range when operated at 4K. At the 4K stage, connections to room temperature are made using copper coaxial cables and astrocobra-flex 31086S cables.

3.2 Data acquisition and processing

This section describes how the measured data is digitally acquired and then processed. First, in 3.2.1, we describe the room temperature setup, which is used to downconvert propagating microwaves signals coming from the cryostats to the MHz regime. Then, in 3.2.2, we explain how the down-converted signal is digitized, demodulated, and filtered to extract relevant physical information. For these steps we rely on a field-programmable gate array (FPGA) with an internal analog-to-digital converter (ADC). For a detailed explanation of the working principles of FPGAs, we refer to Ref. [65].

3.2.1 Room temperature setup

The outgoing microwave signal with frequency f_{RF} ($4-6$ GHz) is detected using the setup presented in Fig. 3.8. First, the signal is amplified by a room-temperature microwave amplifier (AFS5 from Miteq), which provides a gain of 41.5 dB. This amplifier is followed by an isolator (ECI04-5 from EPX microwave) and a bandpass filter (VBFZ $5500-S+$ from MiniCircuits). This filter has a bandwidth of 1.4 GHz centered at 5.5 GHz. Inder to allow for the sampling by the FPGA (described in section 3.2.2), the signal needs to be down-converted to an intermediate frequency f_{IF} in the MHz regime. Therefore, a strong (16 dBm) microwave signal, referred to as local oscillator (LO), at frequency $f_{\mathrm{LO}} = f_{\mathrm{RF}} + f_{\mathrm{IF}}$ (generated by an SGS100A source from Rohde&Schwarz), is mixed with the incoming signals at an image-rejection mixer (IRM4080B from Polyphase microwave). This mixer filters the unwanted signals at frequency $2f_{\mathrm{RF}} + f_{\mathrm{IF}}$, thus improving the signal-to-noise ratio.

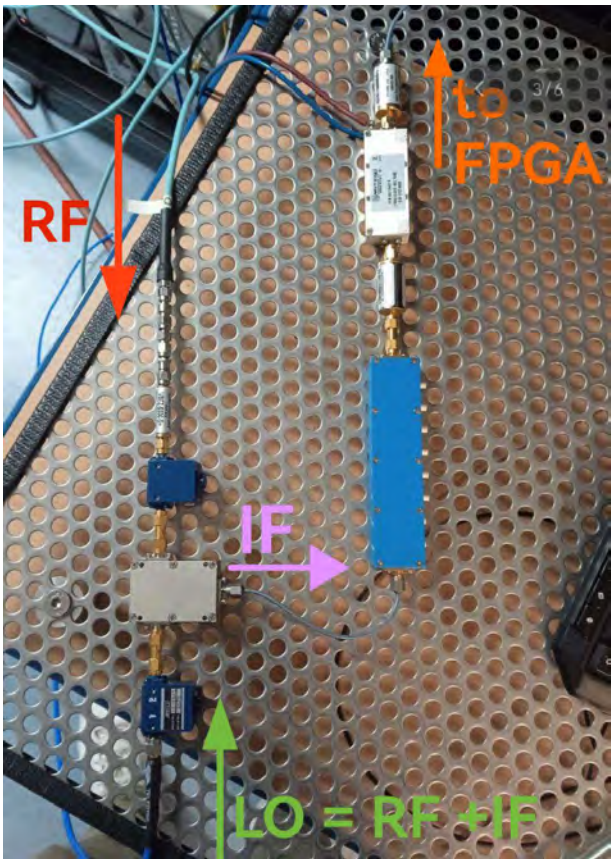

Figure 3.8: Photography of the room temperature setup for the signal down-conversion.

After the image-rejection mixer, the signal at $f_{\rm IF}$ frequency is attenuated by a step attenuator (ESA2-1-10/8-SFSF from EPX microwave). The step attenuator is used to regulate the amplitude of the signals measured at the FPGA after amplification. This step is necessary to make use of all the vertical range of the internal ADC of the FPGA, thus reducing the effects of quantization errors. In our experiments, the level of attenuation was set to 8 dB. Then, the signal goes through a low-pass filter (DC-50 MHz) and, then, it is amplified with an IF amplifier of nomina gain 58.7 dB (model AU 1447 from Miteq). Lastly, the signal is again filtered with a low-pass filter with cut-off frequency of 50 MHz, to avoid distortions introduced by higher frequency components, before being digitalized by the FPGA. All the devices are referenced to a 10 MHz reference signal coming from a rubidium frequency standard. To avoid undesired interference with this 10 MHz reference, the intermediate frequency $f_{\rm IF}$ is set to 12.5 MHz. A schematic of the setup is shown in Fig. 3.9.

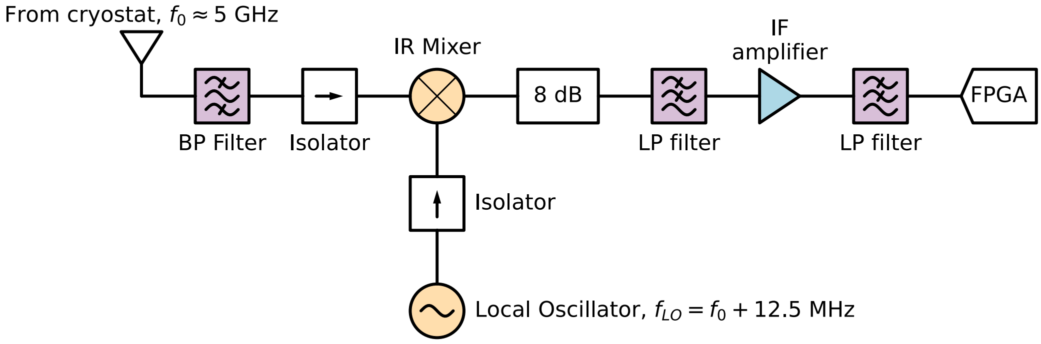

Figure 3.9: Schematic of the room temperature microwave receiver.

3.2.2 Data digitization

The down-converted IF signal is digitized using a PXIe-5775 NI FPGA [66]. The front panel of the FPGA is equipped with three input ports. The first two (AI0 and AI1) are the inputs for the two analog channels of the internal ADC of the FPGA (ADC-12DJ3200, from *Texas Instruments*) . The third one is the input port for the 10 MHz reference signal, as the FPGA is referenced to the same rubidium reference as the devices described in section 3.2.1. The front panel connections of the FPGA are shown in Fig. 3.10. The FPGA digitizes the signals at the input of both channels with a sampling frequency of f_s = 200 MHz and a 12-bit vertical resolution over a full scale range of 1.25 V.

The first analog channel of the FPGA (labeled as AI 0) is connected to the output of the down-conversion chain (labeled as DCC in Fig. 3.10) described in section 3.2.1. The second analog channel (AI 1) is connected to the output channel of an arbitrary waveform generator (HDAWG from Zurich Instruments). The arbitrary waveform generator has a vertical precision of 16-bit and a time resolution of 0.4 nanoseconds. The signal from th HDAWG is used to define the time window for the data acquisition of duration t_w. The third port (REF CLK IN) is connected to the common 10 MHz rubidium reference.

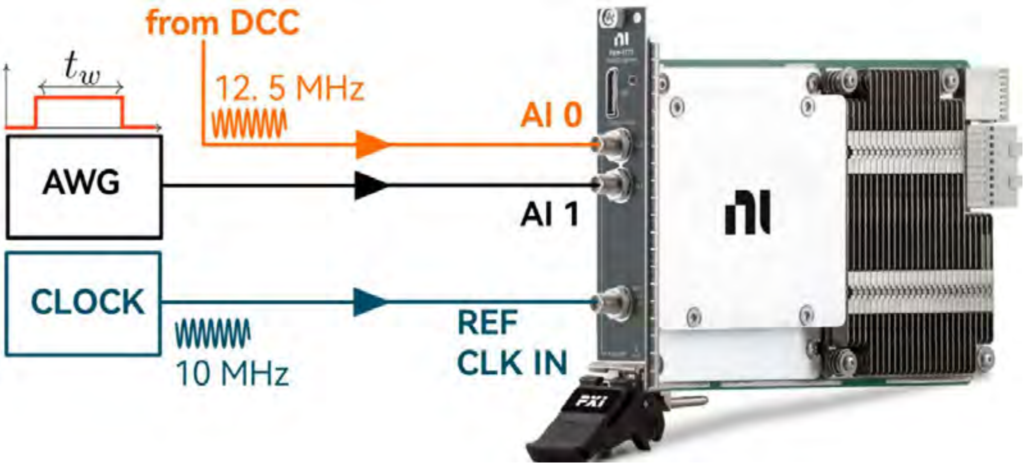

Figure 3.10: Front panel connections of the NI PXIe-5775 FPGA used in our experiments. The orange line indicates the propagating signal coming from the down-conversion chain (DCC). The signal has a carrier frequency $f_{\mathrm{IF}} = 12.5$ MHz. The black line indicates the boxcar pulse (described in 3.2.2 of length t_w generated by the HDAWG. The amplitude of the boxcar pulse is fixed to 100 mV. The green line indicates the 10 MHz clock signal coming from the common rubidium source.

FPGA Image

A part of this thesis work was dedicated to the development of the FPGA code, referred to as the FPGA Image, which defines the internal data procession inside of the FPGA. This Image was developed using the LabView programming language and the proprietary framework provided by National Instruments to program NI FPGAs, LabView FPGA.

Implementation The fundamental logic element of the FPGA Image is the single clock timed loop (SCTL) [67]. While the FPGA is running, every instruction of the SCTL is executed sequentially once. The SCTL is then repeated with a given rate, the data clock rate, which is fixed to 200 MHz for our device. In our FPGA image, the logic of each loop is straightforward. During each iteration of the loop, the FPGA reads one sample from each analog channel, s_0 and s_1. Since the amount of available memory (BRAM) inside the FPGA is limited and the internal ADC is continuously acquiring data from the analog inputs, we need to select the digitized points we want to store. As mentioned before, we use the second analog channel (AI 1) to define a measurement window of duration t_w. At the input of AI 1, we always send a boxcar pulse generated by the HDAWG with an amplitude fixed to 100 mV and a temporal width t_w, which can be varied depending on how many points we want to acquire. Basically, the digitized points from the down-conversion chain, s_0, are saved in memory only if they are recorded while the s_1 signal is above a fixed amplitude threshold. These points are loaded on a First-In-First-Out (FIFO) memory. In this way, during the measurement window, we acquire one point for each cycle of the SCTL. The sampling frequency of our setup is $f_s = 200$ MHz. The number of sampled points during a time window is $N = \lfloor f_s \cdot t_w \rfloor$, where the floor function $\lfloor x \rfloor$ denotes the biggest integer smaller than x. For example, a time window with duration $t_w = 100\,\mu$s allows to sample $N = 2 \cdot 10^4$ points. For steady-state measurements, the FIFO was designed to hold up to 2^{21} sampled points, which is equivalent to a total duration $t_w \approx 10$ ms. The data stored in the FIFO is locally saved before being sent to the measurement PC using a TCP/IP channel.

Limitations in FPGA Programming The main limitation of FPGA programming is the available block RAM (BRAM) memory. For the PXIe-5775 model used in this work, the available BRAM is 38.8 Megabits (4.65 Megabytes). Currently, the FIFO is designed to contain as much as $2^{21} = 2.097.152$ of sampled points. Since every point occupies a memory of 12 bits and the FIFO can contain only 2^m sample, the available BRAM prevents further optimization in this direction.

IQ demodulation

The sampled trace is divided into sub-traces of $N = 16$ points each. Since the digitized IF signal propagates with a carrier frequency of $f_{\mathrm{IF}} = 12.5$ MHz and is sampled with a frequency $f_s = 200$ MHz, we note that each sub-trace corresponds to exactly one period of the sampled signal. From each sub-trace, we estimate one point in the (I, Q) plane. This means that from a raw trace that contains 2.097.152 points, we obtain up to 131.072 demodulated (I,Q) points. Following Ref. [68], we estimate the I and Q values via numerical integration, using

$$\begin{aligned} I &= \frac{2}{N}\sum_{k=0}^{N-1} s_k \cdot \sin\left(k \cdot \Delta\varphi\right), \\ Q &= \frac{2}{N}\sum_{k=0}^{N-1} s_k \cdot \cos\left(k \cdot \Delta\varphi\right), \end{aligned} \tag{3.2}$$

where $\Delta\varphi = 2\pi f_{\mathrm{IF}}/f_s$ is the phase acquired by the signal between two consecutive samplings, which depends only on f_{IF} and f_s. In our case $\Delta\varphi = \pi/8$. The computation of the (I, Q) value is performed using a Python program. To make the computation more efficient we perform a single numerical integration by defining

$$z = I + \mathrm{j}Q = \frac{1}{8}\sum_{k=0}^{N-1} s_k \cdot e^{\mathrm{j}k\pi/8}. \tag{3.3}$$

Then, the (I,Q) components are extracted as the real and imaginary party of z, respectively. In case of very large datasets, a small but significant numerical improvement consists in replacing the sum in equation 3.3 with a scalar product [69]. In practice, we store each sub-trace in an array $\vec{s} = (s_0, \dots, s_{15})$ and the phasor in a vector $\vec{\varphi} = 1/8\left(1, e^{\mathrm{j}\pi/8}, \dots, e^{\mathrm{j}15\pi/8}\right)$ and compute

$$z = \vec{s} \cdot \vec{\varphi}. \tag{3.4}$$

FIR Filtering

A finite impulse response (FIR) filter is a linear, shift-invariant filter, with an impulse response sequence $h\,[n]$. The output function $y\,[n]$ to an arbitrary time-trace of demodulated points function $z\,[n]$ is given by the convolution [70]

$$y\,[n] = z * h = \sum_{k=0}^{n} z\left[k\right] h\left[n-k\right]. \tag{3.5}$$

Digital FIR Filters are used to remove the effects of off-resonant noise in a numerically efficient way. For our experiments, we use a broad FIR filter of width 6 MHz. The choice of the filter width is crucial for our experiments. Indeed, an FIR filter with frequency bandwidth Δf, introduces significant correlations between every $f_{\mathrm{IF}}/\Delta f$ consecutive points of our sampled signal. While this is a natural feature of all FIR filters, we want to avoid as much as possible creating correlations between consecutive pairs of (I,Q)-points since our tomographic protocol relies on the assumption of independent samplings of I and Q quadratures. The filter coefficients are computed using the Python package *scipy.signal*. We designed the FIR filter with window type "Hamming".

3.3 Reference state reconstruction

This section is dedicated to the experimental and theoretical techniques used to calibrate the effects of the amplification chain on the propagating quantum microwave signals. In the first subsection, 3.3.1, we illustrate the experimental realization and the theoretical foundations behind the photon number calibration factor (PNCF) measurement, which allows us to estimate:

- the amount of noise introduced by the amplification chain;
- the conversion factor between the number of photons in the propagating quantum microwave signal and the detected power at the FPGA.

In the second subsection 3.3.2, we introduce a different approach to measure the number of noise photons, which improves both the accuracy and the required amount of time compared to the PNCF measurement.

3.3.1 Experimental calibration of the amplification chain

In this section, we discuss the experimental realization and the theoretical foundations behind the PNCF measurement. This section is organized as follows: we start by illustrating the experimental setup needed to perform the PNCF measurement and, after that, we briefly describe the theoretical model used to interpret the experimental results from the PNCF. We conclude this section with the analysis of the experimental data obtained during the PNCF measurement .

Calibration of the Photon Number Conversion Factor

To calibrate the amplification chain, we need a photon source that emits a known number of photons in the transmission line at millikelvin temperatures. For this purpose, we employ a 30 dB attenuator, which acts as a black-body emitter of thermal radiation [71]. The attenuator is placed in an oxygen-free high thermal conductivity (OFHC) copper holder. On its side, we fix a heater and a calibrated temperature sensor. The heater is controlled by an external PID-controlled loop which allows the temperature of the attenuator T_{att} to be varied in a broad range between 60 mK and 550 mK. The temperature is monitored in real time using the calibrated temperature sensor. In Figure 3.11, we show how the 30 dB attenuator is connected in our setup. The attenuator is placed on the input line of the JPC. It is connected to the mixing chamber (MXC) and to the rest of the setup using two NbTi/NbTi coaxial cables which ensure low losses for the emitted thermal signals and good thermal isolation from the MXC. In addition to that, we use a silver ribbon cable to weakly couple the attenuator to the mixing chamber plate. This silver ribbons allows for the temperature of the attenuator to go back to around 60 mK after heating it, while the weakness of this thermal coupling does not allow the mixing chamber to be overheated when the attenuator temperature is raised, thus, keeping the remaining part of the setup constantly at 60 mK.

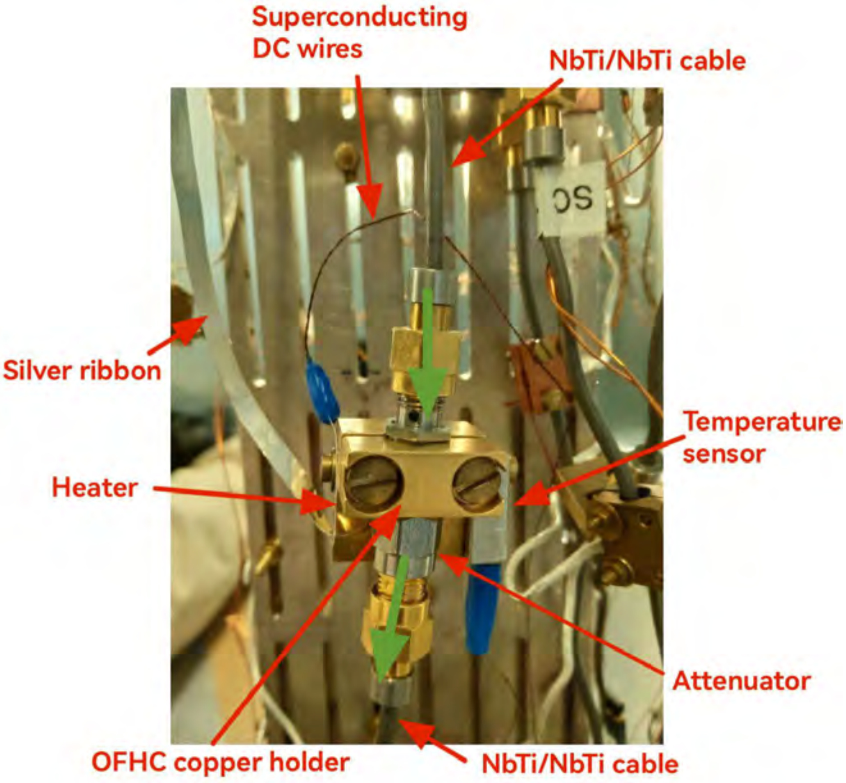

Figure 3.11: Photo image of the heatable attenuator used in the cryogenic set-up.

Theoretical model: neglecting cryogenic losses

In this section, we briefly describe a theoretical model which can be used to describe the PNCF measurement, in the case with no cryogenic losses. These losses will be considered later. In the ideal case, the thermal mode emitted by the heatable attenuator, $\hat{a}$, is not subject to any losses before reaching the HEMT amplifier. In this idealized scenario, we can model the whole amplification chain (which is composed by the HEMT amplifier, the room temperature amplifier and the down-conversion chain) as a phase-insensitive amplifier with a gain factor G and noise operator $\hat{v}$. The noise operator $\hat{v}$ describes thermal gaussian noise with photon number $\langle \hat{v}^\dagger v \rangle = n_v$. Formally , by following the convention introduced in Chapter 2, the output signal $\hat{\xi}$ digitized by FPGA is given, by the

$$\hat{\xi} = \sqrt{G}\hat{a} + \sqrt{G-1}\hat{v}^\dagger. \tag{3.6}$$

At the FPGA, the signal is demodulated in its I and Q components. The average power $P_\xi = \langle I^2 + Q^2 \rangle$ detected by the FPGA is a function of the temperature T_{att} of the heatable attenuator. To see this, we start by noting that the measured power at the FPGA can be computed from the statistics of the mode $\hat{\xi}$ as

$$\langle I^2 + Q^2 \rangle = h\, f_0\, \Delta\, R\, \langle \hat{\xi}^\dagger \hat{\xi} \rangle, \tag{3.7}$$

where f_0 is the signal carrier frequency, h is the Planck constant, Δ is the detection bandwidth, and $R = 50\ \Omega$ is the input impedance of the FPGA. This formula can be understood as follows: the product $h\, f_0$ corresponds to the power per unit of bandwidth and per unit photon for the measured mode $\hat{\xi}$. Therefore, the product $hf_0\, \Delta\, \langle \hat{\xi}^\dagger \hat{\xi} \rangle$ is the power measured at the FPGA. The input impedance R is needed for dimensional reasons, since the measured amplitude is in Volts^2. If we insert equation 3.6 in equation 3.7 we obtain

$$\langle I^2 + Q^2 \rangle \approx \kappa G \left(n_a(T_{\mathrm{att}}) + n_v + 1 \right), \tag{3.8}$$

where $\kappa = h\, f_0\, \Delta\, R$ is the PNCF and $n_a = \langle \hat{a}^\dagger \hat{a} \rangle$ is a function of the attenuator temperature T_{att}. Here we use, $(G-1)/G \simeq 1$ since $G \gg 1$ in our experiments. If we use equation 3.1, we can write

$$\langle I^2 + Q^2 \rangle (T_{\mathrm{att}}) = \frac{\kappa G}{2} \left(\coth\left(\frac{hf_0}{2k_b T_{\mathrm{att}}} \right) + 2\left(n_v + \frac{1}{2} \right) \right). \tag{3.9}$$

The quantity $T_{\mathrm{cr}} = hf_0/2k_b$ has the units of a temperature and its called *crossover temperature*. For $T_{\mathrm{att}} \gg T_{\mathrm{cr}}$, the hyperbolic cotangent is equation 3.9 is approximated by a linear relation corresponding to the classical regime of Nyquist noise. For $T_{\mathrm{att}} \simeq T_{\mathrm{cr}}$, quantum fluctuations become measurable. In our experiments ($f_0 \approx 5$ GHz) we expect to observe deviations from classical predictions to happen for $T_{\mathrm{att}} \leq 120$mK.

Theoretical model: including cryogenic losses

Equation 3.9 is valid only in the case of zero cryogenic losses between the heatable attenuator and the HEMT amplifier, which is a bad approximation. In particular, every microwave component we have along the signal path contributes to some extent to the losses of the mode operator $\hat{a}$. In general, a single lossy microwave component can be described by a three-port device with transmission coefficient $\eta < 1$. The output mode $\hat{t}$ of a lossy microwave component can be computed as

$$\hat{t} = \sqrt{\eta}\hat{a} + \sqrt{1-\eta}\hat{u} \tag{3.10}$$

where $\hat{u}$ describes the noise introduced by vacuum fluctuations. Therefore, the transmitted power is given by

$$P_t = \eta P_a, \tag{3.11}$$

and η therefore is related to the attenuation L (measured in dB) of the lossy component by

$$\eta = 10^{-L/10}. \tag{3.12}$$

Given this observation, we improve the model 3.9 by including the losses of each microwave component. We number them from 1 to K, with transmission coefficients from η_1 to η_K. Our phenomenological model is depicted in Fig. 3.12. The mode at the output of the j-th beam splitter is labeled $\hat{a}_j$, while, the input of the j-th beam splitter is the output of the $(j-1)$-th one, $\hat{a}_{j-1}$. The relation between output and input of each microwave component is given by

$$\hat{a}_j = \sqrt{\eta_j}\,\hat{a}_{j-1} + \sqrt{1-\eta_j}\,\hat{u}_j, \tag{3.13}$$

where $\hat{u}_j$ describes the vacuum fluctuations entering the second port of the j-th beam splitter. The power at the output of the j-th beam splitter is therefore

$$P_j = \eta_j P_{j-1}. \tag{3.14}$$

Therefore, by induction, transmitted power P_K at the end of the chain is

$$P_K = \left(\prod_{j=1}^{K} \eta_j\right) P_a = \eta_{\text{eff}} P_a, \tag{3.15}$$

where $\eta_{\text{eff}} = \eta_1 \times \eta_2 \times \cdots \times \eta_K$ is the total transmittivity of the lossy chain. Finally, we include the effects of η_{eff} in the calibration of the amplification chain, by replacing the term with n_a with $\eta_{\text{eff}} n_a$ in Eq. 3.8. With straightforward algebraic steps, we derive

$$\langle I^2 + Q^2\rangle(T_{\text{att}}) = \frac{\kappa G \eta_{\text{eff}}}{2}\left(\coth\left(\frac{hf_0}{2k_b T_{\text{att}}}\right) + \frac{2}{\eta_{\text{eff}}}\left(n_v + \frac{1}{2}\right) + \frac{1-\eta_{\text{eff}}}{\eta_{\text{eff}}}\right). \tag{3.16}$$

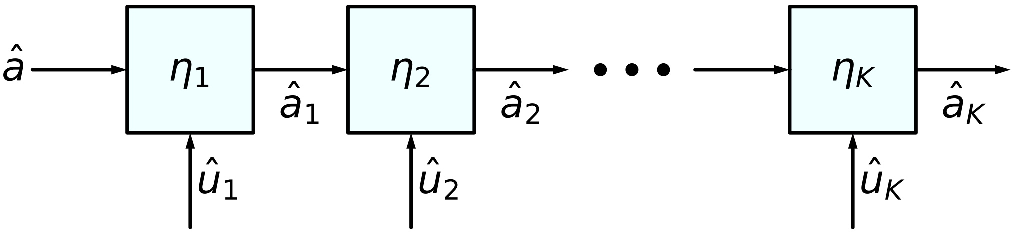

Figure 3.12: Phenomenological model for a chain of K lossy microwave components numbered from 1 to K. Each component is described by its transmittivity η_j.

In our case, we estimated the effective transmission coefficient η_{eff} from the datasheets of the microwave components along the signal path. For the sample boxes we used 0.5 dB of losses. Also, we counted five times the insertion losses of the circulators. We neglected the losses of the superconducting cables, since they are negligible compared to the other components.

Devices	Losses (dB)
Circulators	0.9
Low-pass filter	0.5
Sample boxes	1
Microwave switches	0.6
Total losses	2.7

The total cryogenic losses, in decibels, are estimated to be $L = 2.7$ dB; in linear units the total transmittivity is

$$\eta_{\text{eff}} = 10^{-L/10} = 0.57. \tag{3.17}$$

Measurement of the PNCF

To estimate the parameters κG and n_v entering in equation 3.16, we measured the average power detected by the FPGA, $\langle I^2 + Q^2 \rangle$, for different values of the heatable attenuator temperature T_{att}. As written before, the temperature T_{att} is by means of the heater attached to the 30 dB attenuator on the input line and it is controlled from an external PID control loop. To ensure a proper thermalization of the setup, we performed a preliminary measurement to find an optimal amount of time for the setup to reach the thermal equilibrium. First, we set the attenuator temperature to a high value, $T_{\text{att}} = 550$ mK. When the sample stage reaches $T_{\text{att}} = 550$ mK, we wait for one minute. After that, we record the power arrived at the FPGA. In our case, we collect 1667 traces of 32.768 (I, Q) points over 10.59 minutes; for each trace, we measure the power $\langle I^2 + Q^2 \rangle$, obtaining a single array of 1667 averages. The results are shown in Fig. 3.13.

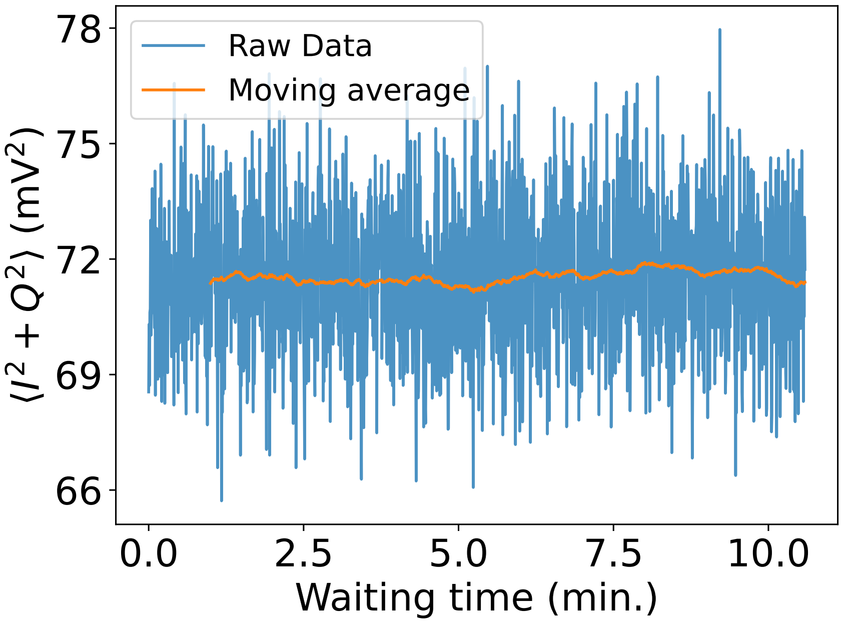

Figure 3.13: Plot of the power measurement. The blue curve indicates the measured fluctuations, while the orange solid line corresponds to the averaged value over 1 minute.

From Fig. 3.13, it is clear that even after a relatively brief time interval of two minutes, the thermal fluctuations in the measured signal are stable, which means that the heatable attenuator is properly thermalized at 550 mK.
Therefore, we set the waiting time to 2 minutes. After the measurement of the thermalization time, we swept the attenuator temperature from 540 mK to 70 mK. Six temperature points were spaced by 60 mK from 540 mK to 120 mK. The remaining T_{att} values were 90 mK, 80 mK and 70 mK. For each temperature point, we recorded 1667 traces of 32.768 (I,Q) points, as we did for the thermalization time measurement. The measured power $\langle I^2 + Q^2 \rangle$ is fitted against T_{att} using the model specified by Eq. 3.16; the unknown parameters are the PNCF factor, $G\kappa$, and the number of noise photons n_ν. The cryogenic losses were accounted for using $\eta_{\text{eff}} = 0.57$, as explained before. For the carrier frequency, we fixed $f_0 = 5.09$ GHz by setting the room temperature local oscillator to $f_{\text{LO}} = (5.09 + 0.0125)$ GHz. The results of this measurement are shown in Fig. 3.14.

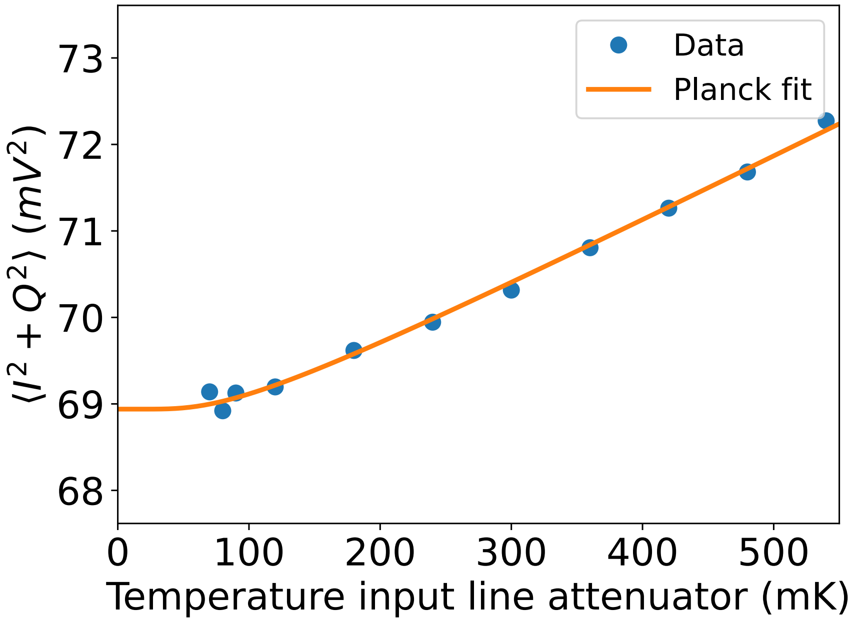

Figure 3.14: PNCF calibration measurement. Blue dots corresponds to the experimental data, red line corresponds to the fitted model according to Eq. 3.15.

From Fig. 3.14, we note that the saturation of the signal fluctuations starts to emerge around $T_{att} \approx 120$ mK as we expected from the theoretical model. From the fit, we w estimate

$$\begin{aligned} G\kappa &= 3.4 \pm 0.2\,\mathrm{mV}^2, \\ n_\nu &= 19.5 \pm 1.3\,\text{photons}. \end{aligned} \tag{3.18}$$

The relative errors on both quantities are respectively 5.8% for the PNCF factor, $G\kappa$, and 6.7% for the noise photon number n_ν.

3.3.2 Reference state reconstruction from histograms

Despite the PNCF measurement provides a fairly accurate estimation of the noise photon number n_ν (relative error smaller than 10%), it suffers from some drawbacks:

1. The measurement can be time-consuming due to the time we have to wait for the temperature to stabilize.
2. Fitting the low-temperature saturation predicted by equation 3.16 is challenging, because the lowest temperature reached by the attenuator are usually quite close to the crossover temperature T_{cr}. This means that only a small part of the hyperbolic cotangent curve is visible beyond the "elbow" at $T_{\mathrm{att}} \approx T_{\mathrm{cr}}$, as it can be seen from Fig. 3.14.

In this section, we present an alternative measurement, which can be used to estimate the photon noise number n_ν. This measurement relies only on the slope of the PNCF measurement. In this sense, the time advantage is clear since we have to measure the received power $\langle I^2 + Q^2\rangle$ only for a handful of temperature points T_{att} to get a precise estimation of the slope $G\kappa$. The idea of the measurement is very simple: with the heater turned off, we measure at the FPGA the (I,Q) points of the fluctuations coming from the cryostat. Since the heater is off, the mode $\hat{a}$, which is amplified by the amplification chain, is described by a weak thermal gaussian state with low photon number $n_a \leq 2 \times 10^{-4}$. In the following, we therefore assume that the mode $\hat{a}$ describes vacuum fluctuations. The (I,Q) points of the amplified mode $\hat{\xi}$ are collected in a 2D histogram with 100×100 bins. The probability distribution of the (I,Q) points can be estimated theoretically using the Q-function Q_ξ of the observed field, described by the mode operator $\hat{\xi}$. From equation **??**, we derive that the distribution probability of the measured mode $\hat{\xi}$ is

$$Q_\xi(I,Q) = \mathcal{N} \exp\left(-\frac{(I^2+Q^2)}{\kappa G(n_v + 1/2)}\right), \tag{3.19}$$

where $\mathcal{N}$ is a normalization factor fixed by the requirement that $\int Q_\xi = 1$. We note that Eq. 3.19 is based on the assumption that the field mode $\hat{a}$ describes vacuum fluctuations. In principle, this assumption can be relaxed by assuming that the mode $\hat{a}$ describes weak thermal fluctuations corresponding to the temperature of the MXC, $T \simeq 40 - 70$ mK, id est a gaussian thermal state with number of photons $n_a \simeq 2 \times 10^{-4}$. In this case, Eq. 3.19 can be modified by inserting in Eq. 2.30 the Husimi Q-function of a thermal state with photon number n_a instead of the Q-function of the vacuum state. We observe that, in our case, we don't observe any measurable variation in the estimation of n_v and its statistical error by using this approach. By fitting the measured 2D Histogram with the theoretical distribution 3.19, we can get a more accurate estimate of n_v. The measured histogram with the contour lines of the fitted gaussian are plotted in Fig. 3.15. From

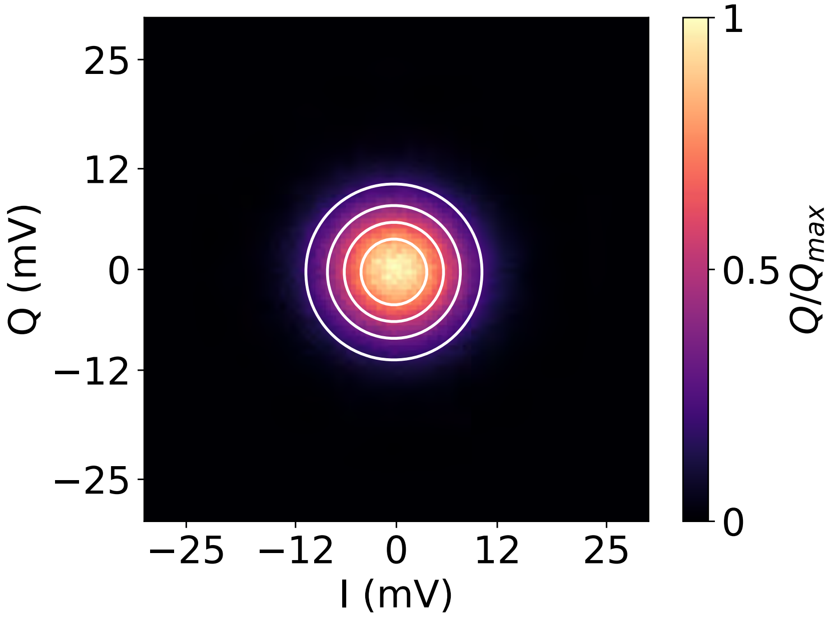

Figure 3.15: Color map of the 2D Histogram of the measured mode $\hat{\xi}$ and contour plot of the fitted theoretical model (solid white lines). Both functions are normalized to the maximum value.

the numerical fit, we obtain a new estimate for n_v,

$$n_v = 19.44 \pm 0.06 \ \text{photons} . \tag{3.20}$$

The value of n_v is compatible with the one measured previously. The accuracy of the measurement is higher by a factor of 22. In Fig. 3.16 we show the cross-section of both the measured histogram and the fitted probability distribution along the $Q = 0$ axis.

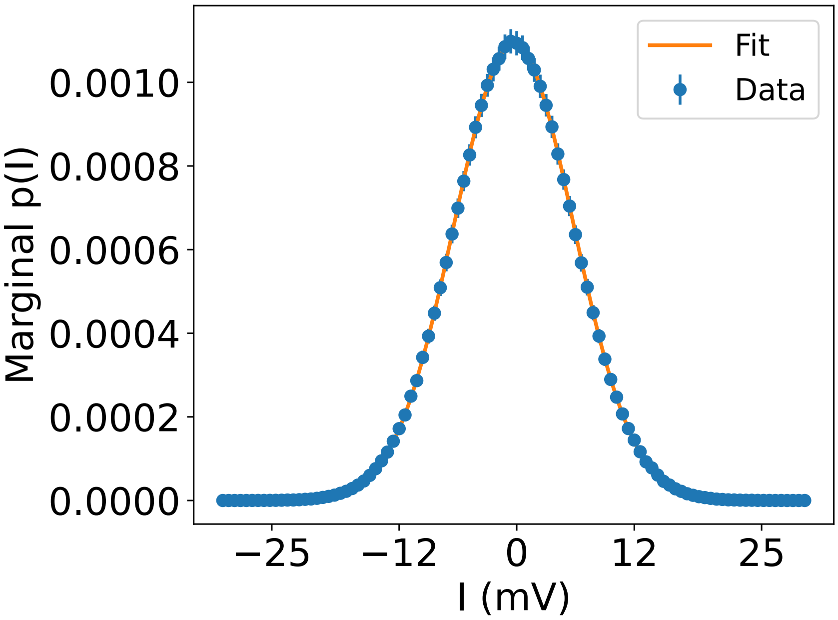

Figure 3.16: Marginal distribution $p(I)$ of the measured histogram (blue dots) and gaussian fit (orange solid line) for the reference state. Both datasets are normalized to the maximum value of the measured histogram.

Another advantage of this method is that it confirms, within the experimental accuracy, the Gaussian distribution of the noise mode operator $\hat{v}$ introduced by the amplification chain. The *Gaussianity* for the mode $\hat{v}$ was also confirmed by the analysis of the Shannon entropy [72] of the measured distribution. Indeed, as proposed by Hyvärinen and Oyla in Ref. [73], we use the Shannon entropy [72] of the measured distribution to test its *Gaussianity*. In order to do so, we start by computing the marginal distribution of the measured histogram along the I-axis, $p(I)$, by integrating the coordinate along the orthogonal axis for the Q coordinate. The marginal distribution $p(I)$ is fitted to a one-dimensional gaussian function, as shown Fig 3.16. At this point, the Shannon entropy of the marginal distribution $p(I)$, labeled as $\mathbb{H}\left[p\right]$ is computed from its definition [72]

$$\mathbb{H}\left[p\right] = -\int dI \, p(I) \log\left(p(I)\right). \tag{3.21}$$

The computed entropy is compared with the expected Shannon entropy for one-dimensional gaussian distribution [74],

$$\mathbb{H}_{\text{expected}} = \frac{1}{2} \log\left(2\sigma^2 \pi e\right), \tag{3.22}$$

where σ is the standard deviation extracted from the gaussian fit. We obtain,

$$\begin{aligned} \mathbb{H}_p &= 3.227 \pm 0.005, \\ \mathbb{H}_{\text{expected}} &= 3.223 \pm 0.002, \end{aligned} \tag{3.23}$$

which are equal within their statistical error. Since, for a given standard deviation σ, the gaussian distribution *maximizes* the Shannon entropy [74, 72], the extracted value imply that, within the experimental errors, the marginal distribution $p(I)$ is a gaussian distribution. The statistical error on $\mathbb{H}_p$ was computed by evaluating the integral

$$\int dI\, \delta\left\{p(I)\right\} \left(1 + \log\big(p(I)\big)\right), \tag{3.24}$$

where $\delta\left\{p(I)\right\}$ indicate the statistical error on the marginal distribution $p(I)$. The integral was obtained by using standard error propagation [75] on Eq. 3.21.

This procedure is then repeated for the marginal distributions $p_\theta(I_\theta)$, obtained by integrating the measured integral along the angle $\theta + \pi/2$ in the (I,Q)-plane, for 31 angles evenly distributed between 0 and π. In Fig. 3.17 , we plot the relative difference $\delta_{\mathbb{H}}$, defined as

$$\delta_{\mathbb{H}} = \frac{\left|\mathbb{H}_p - \mathbb{H}_{\text{expected}}\right|}{\mathbb{H}_p}, \tag{3.25}$$

as a function of all the considered values of θ. We observe that the entropies $\mathbb{H}_p$ and $\mathbb{H}_{\text{expected}}$ are compatible within their statistical errors, id est the experimental data suggest that each marginal distribution p_θ is a gaussian distribution. Since the only two-dimensiaonal function which has only gaussian marginals distributions is a gaussian itself, we conclude that noise mode $\hat{v}$ is well-described by gaussian statistics.

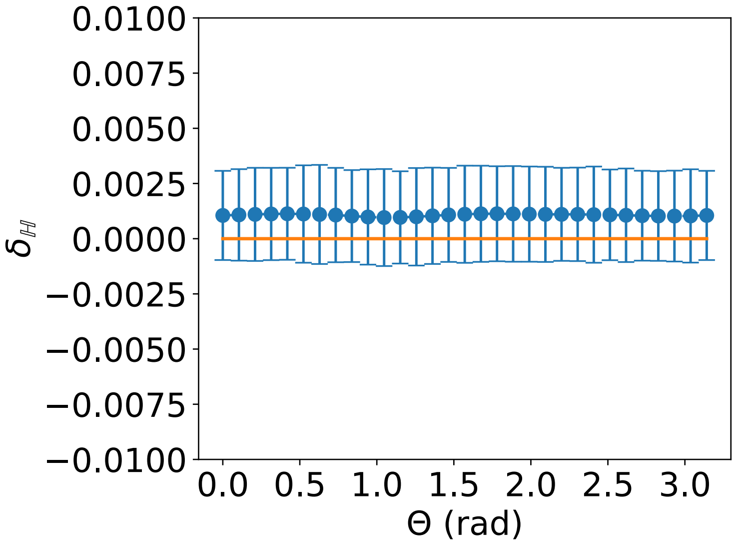

Figure 3.17: Relative difference $\delta_{\mathbb{H}}$ as a function of the angle θ. The relative difference $\delta_{\mathbb{H}} \simeq 10^{-3}$ for all the values of θ. The blue dots indicate the extracted values. The orange solid line refers to the value $\delta_{\mathbb{H}} = 0$..

3.4 Calibration of superconducting quantum circuits

In this section, we describe the spectroscopic measurement performed on the superconducting devices used in this thesis. In particular, by analyzing the reflection coefficient of each device, we measure their resonance frequency and quality factors. This section is organized as follows: in the subsection 3.4.1 we briefly describe the theoretical model and the practical implementation of our measurement. Next, in the subsection 3.4.2, we present present the experimental results for the JPC. In the last subsection 3.4.3, we present the experimental results for the JPA.

3.4.1 The reflection coefficient

In the following sections of this chapter, characterize our devices using the model of linear resonators with resonance frequency f_0 and internal and external quality factors Q_{int} and Q_{ext}. We define the angular resonance frequency ω_0, the external and internal coupling constants as

$$\begin{aligned} \omega_0 &= 2\pi f_0, \\ \gamma_i &= \frac{\omega_0}{Q_{int}}, \\ \gamma_e &= \frac{\omega_0}{Q_{ext}}. \end{aligned} \tag{3.26}$$

We also define the total coupling constant

$$\gamma = \gamma_i + \gamma_e. \tag{3.27}$$

The complex reflection coefficient Γ is

$$\Gamma(\omega) = 1 - \frac{\mathrm{j}\gamma_e}{\mathrm{j}\,(\omega - \omega_0) + \gamma/2}. \tag{3.28}$$

The model described by equation 3.28 does not take into account possible effects caused by the external experimental environment. These effects may include: impedance mismatch, finite electric delay, and parasitic losses. To take these effects into account, we use the model introduced in Ref. [76],

$$\Gamma(\omega) = A e^{\mathrm{j}\alpha} e^{-\mathrm{j}\omega\tau} \left(1 - \frac{\mathrm{j}\gamma_e e^{i\phi}}{\mathrm{j}\,(\omega - \omega_0) + \gamma/2} \right) \tag{3.29}$$

where A describes possible attenuation/gain effects of the measurement setup, α describes possible phase-shifts, τ quantifies the electric delay, and ϕ takes into account the impedance mismatch. A complete calibration and fitting routine for this model is included in the Python package *resonator tools* [77] which was used to fit the experimental results described in this section.

The reflection coefficient is with a Vector-Network-Analyzer (VNA). The used VNA is the PNA 5222A manufactured by Keysight [78]. The device is controlled using an in-house driver developed using LabView programming language. One of the ports of the VNA, in our case port 1, is connected to the input line A22 going inside of the cryostat using a room-temperature RF cable. The port 1 connector is also equipped with a 40 dB attenuator to reduce the input power flowing in the experimental setup. The output line collects the reflected signal from the superconducting device and is connected using an RF room-temperature cable to port 2 of the VNA. In this configuration, the VNA measures the scattering coefficient S_{21} which accurately estimates the reflection amplitude of our superconducting devices.

3.4.2 JPC measurements

The spectroscopic parameters of the JPC are measured by sending a coherent tone with the power $P_{\mathrm{VNA}} = -130$ dBm, at the device. The coherent tone frequency is swept in a frequency range $\left[f_0 - f_{\mathrm{bw}}/2, f_0 + f_{\mathrm{bw}}/2\right]$ with center frequency, $f_0 = 5.09$ GHz, and bandwidth $f_{\mathrm{bw}} = 20$ MHz. In this frequency range, we measure $N = 801$ frequency values spaced by a constant frequency step $\Delta f \approx 25$ kHz. The scattering coefficient $S_{21}(\omega)$ is averaged three times. Since the JPC is a flux-tunable device, we repeat the measurement by sweeping the value of the bias current through the superconducting coil on top of the JPC sample box. The coil current is swept from $-50\,\mu$A to $50\,\mu$A with a constant step of $2\,\mu$A. In Fig. 3.18 we show the measured JPC resonant frequency as a function of bias current. The resonance frequency is tunable in a 12.5 MHz wide range from 5.0825 GHz to 5.0950 GHz. In Fig. 3.18, the resonance frequency was estimated by measuring the frequency value of the dip in the magnitude of the reflection coefficient.

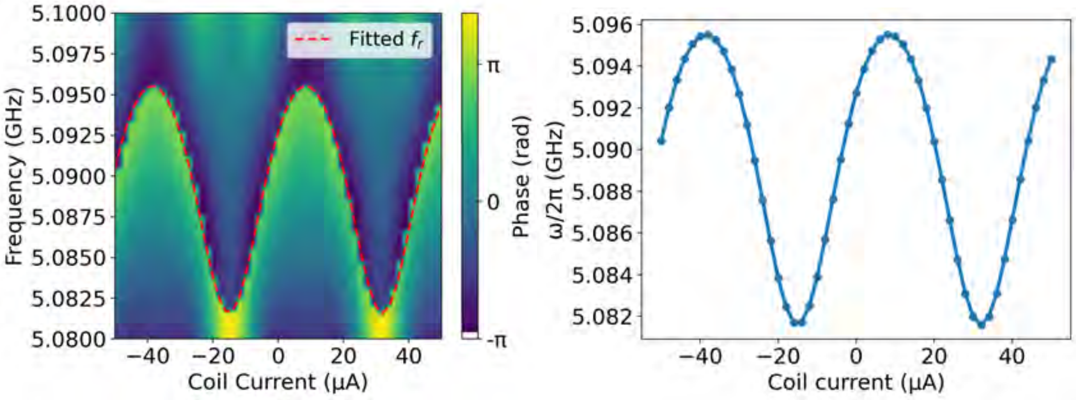

(a) (b)

Figure 3.18: JPC spectroscopic measurement as a function of the coil current. Panel (a) illustrates the phase of the reflected signal. The dotted red line indicates the fitted resonance frequencies. Panel (b) shows the fitted resonance frequencies as a function of the coil current.

For each value of the coil current, the measured scattering coefficient is fitted using the model 3.29 to precisely extract the parameters Q_i, Q_e and f_0. An exemplary fit of the magnitude and phase responses for the coil current value of 30 μA is shown in Fig. 3.19.

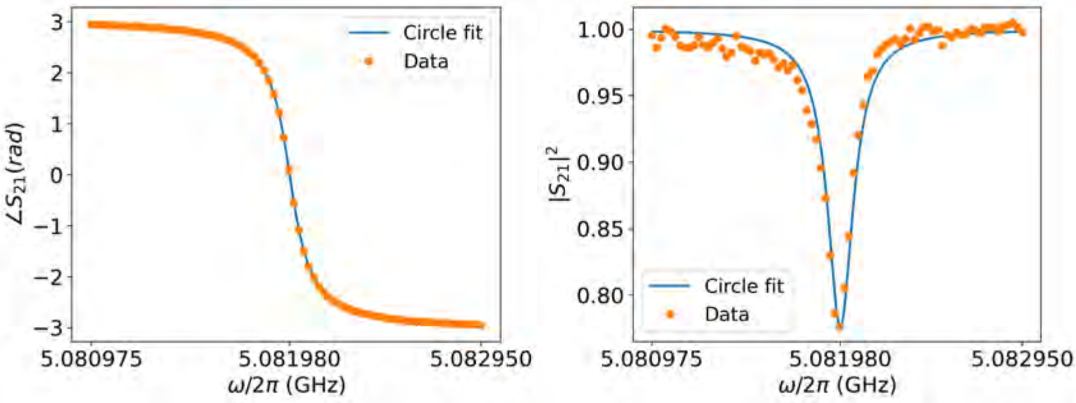

(a) (b)

Figure 3.19: Exemplary fit of the phase (Fig. a) and magnitude (Fig. b) of the scattering coefficient S_{21} for the JPC, fitted using equation 3.29. In this case, the coil current was set to $I_c = 30\,\mu$A and the VNA input power was set to $P_{VNA} = -20$ dBm.

The fitted values for the quality factors as a function of the coil current are shown in Fig. 3.20. In particular, we show the fitted values for the external Q_e and loaded Q_l quality factors. From the figure, we observe that both quantities are almost independent from the value of the coil current. The external quality factor fluctuates around $Q_e = (3.33 \pm 0.04) \times 10^4$, and the loaded one fluctuates around $Q_l = (2.99 \pm 0.03) \times 10^4$.

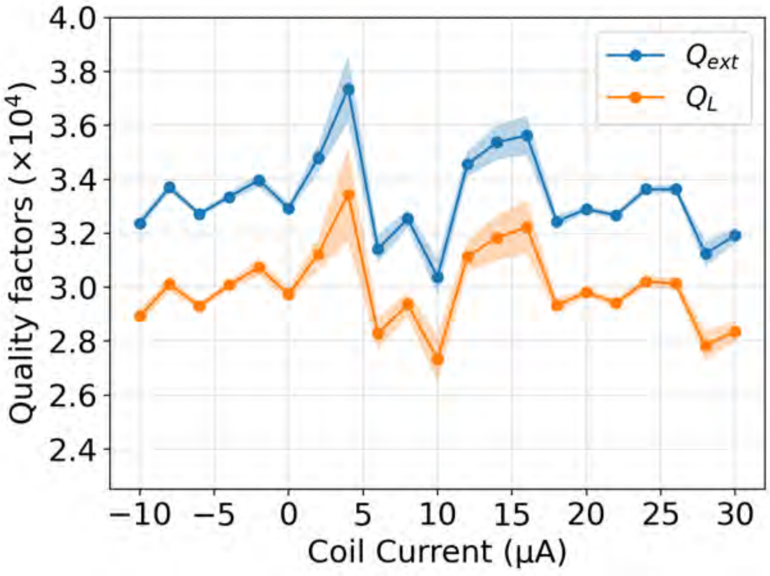

Figure 3.20: Fitted external (blue line) and loaded (orange line) quality factors as a function of the coil current. The VNA power was set to $P_{VNA} = -130\text{dBm}$. The shaded region indicates the statistical error on the fitting routine.

The average value of the internal quality factor can be computed as

$$Q_i = \frac{Q_e Q_l}{Q_e - Q_l} = \left(2.97 \pm 0.05\right) \times 10^5. \tag{3.30}$$

The relative errors for the quality factors are respectively 1.03% for Q_{ext}, 1.05% for Q_l and 1.59% for Q_i. From the measured quality factors, we can evaluate the external and total coupling factors γ_e and γ using Eqs. 3.26 and 3.27. As expected, the coupling constants values fluctuate around a constant mean. We measure

$$\begin{aligned} \gamma &= 1.07 \pm 0.02 \text{ MHz} , \\ \gamma_e &= 0.96 \pm 0.01 \text{ MHz} . \end{aligned} \tag{3.31}$$

The coupling constants γ and γ_{ext} are plotted against the coil current in Fig. 3.21.

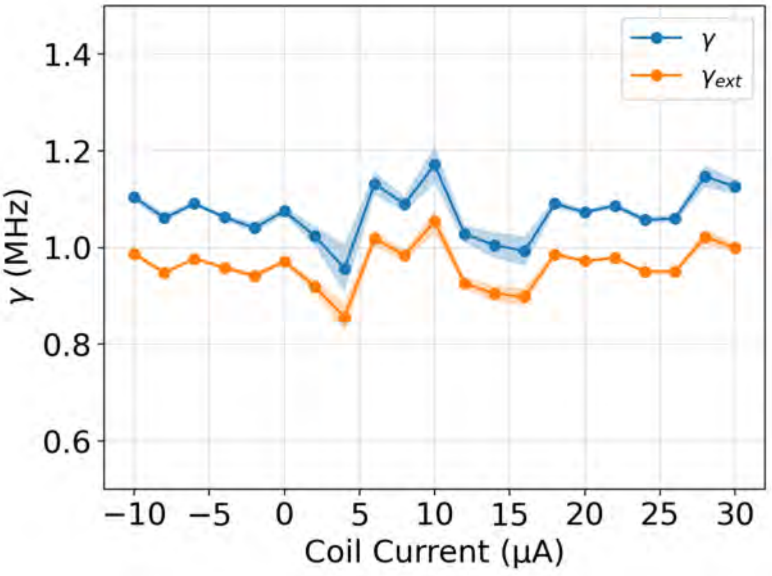

Figure 3.21: Coupling constants of the JPC as a function of the bias current.

The average lifetime of the JPC $\tau_{\mathrm{JPC}} = 1/\gamma$, defined in Chapter 1, is computed as

$$\tau_{\mathrm{JPC}} = 0.93 \pm 0.02 \qquad \mu\mathrm{s}. \tag{3.32}$$

3.4.3 JPA measurements

The spectroscopic parameters of the JPA are measured by sending a coherent tone of power $P_{\mathrm{VNA}} = -115$ dBm, at the device. The coherent tone frequency is swept in a frequency range $\left[f_0 - f_{\mathrm{bw}}/2, f_0 + f_{\mathrm{bw}}/2\right]$ with a center frequency $f_0 = 5.0$ GHz and bandwidth $f_{\mathrm{bw}} = 2$ GHz. In this frequency range, we measure $N = 401$ frequency values with an IF frequency bandwidth of 40 Hz. In Fig. 3.22, we plot the phase of the reflection coefficient as a function of the frequency and coil current values. The frequency of the JPA can be tuned in a broad range from 5.3 GHz to 4.5 GHz.

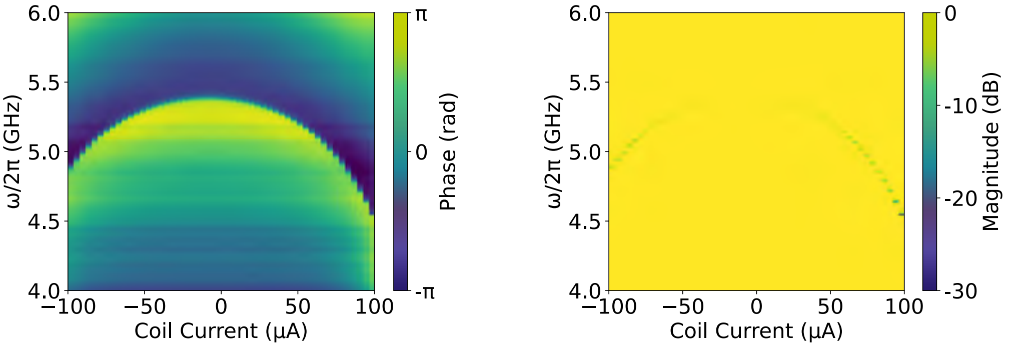

(a)

(b)

Figure 3.22: JPA spectroscopy. Panel (a) shows the phase of the reflection coefficient, measured in radians, as a function of the VNA tone frequency and the coil current. In panel (b), the magnitude of the complex reflection coefficient, is measured in decibels.

In this case, the model 3.29 does not converge. Therefore, we only fit the phase of the reflection coefficient as a function of the frequency, for all the coil currents values. This approach is limiting, in the sense that allows us to estimate precisely only the loaded quality factor of the resonator Q_l. We use the model from Ref. [76],

$$\vartheta(f) = \vartheta_0 + 2\arctan\left[2Q_l\left(1-\frac{f}{f_r}\right)\right], \tag{3.33}$$

where $\vartheta(f)$ is the phase of the reflection coefficient as a function of the frequency, f_r is the resonance frequency and $\vartheta_0 = \vartheta(f_r)$ is the phase offset. In Fig. 3.23, the fit 3.33 is shown for the coil current value of 68 μA. The fitted resonance frequencies are plotted as a function of the coil current values and are also shown in Fig. 3.23.

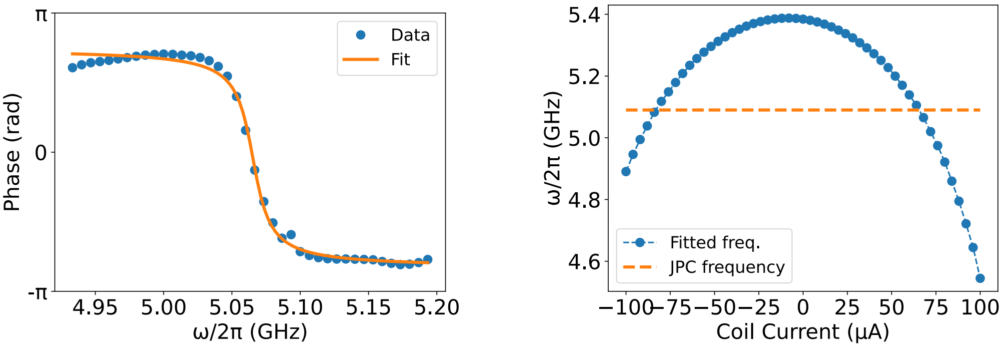

(a)

(b)

Figure 3.23: Panel (a), fit 3.33 for the phase of the reflection coefficient. The data shown correspond to the coil current value of 68 μA. Panel (b) shows the extracted resonance frequencies. The orange dashed line indicates the frequency of the JPC for a JPC coil current of 0 μA. The error bars of the exctracted frequencies are smaller than the marker size.

From the fit 3.23 we estimate the resonance frequency and the loaded quality factor of the

JPA as a function of the coil current. From the knowledge of the loaded quality factor Q_l and the resonance frequency, we estimate the decay rate γ, defined as

$$\gamma = 2\pi \frac{f_0}{Q_l}. \tag{3.34}$$

In Fig. 3.24, we show the loaded quality factor Q_l and the decay rate γ as a function of the coil current.

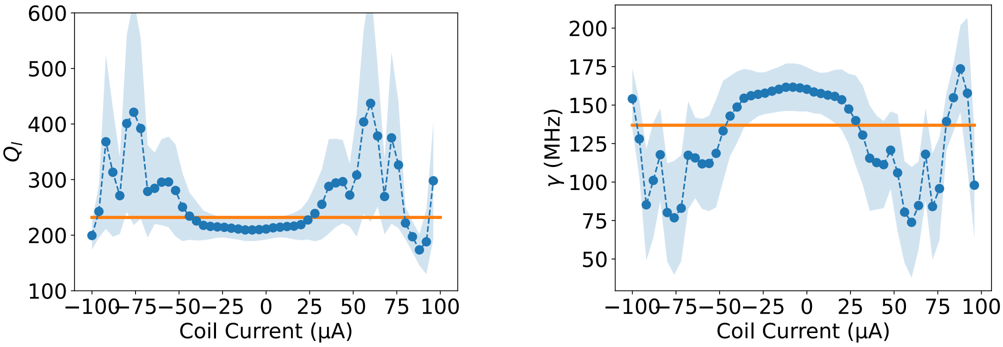

(a) **(b)**

Figure 3.24: Loaded quality factor Q_l, panel (a), estimated from fit 3.33 and total decay rate γ as a function of the coil current. In both plots, the blue-shaded region indicates the statistical error on the measured quantity, estimated as three times the standard deviation of the fit's estimators. In both plots, the orange solid line indicates the weighted average of the measured values weighted inversely to their respective statistical errors.

The mean values of Q_l and γ, weighted by the inverse of their statical errors, are respectively

$$\begin{aligned} \gamma &= 136 \pm 31 \text{ MHz} , \\ Q_l &= 232 \pm 51. \end{aligned} \tag{3.35}$$

The photon life-time $\tau = 1/\gamma$ is plotted as a function of the coil current in Fig. 3.25. The measured average photon lifetime is

$$\tau = 7 \pm 2 \text{ ns} . \tag{3.36}$$

The measured average photon lifetime is much smaller than the time resolution we can reach in our experiments, which is fixed by the inverse of the IF frequency $f_{\mathrm{IF}} = 12.5$ MHz. Indeed, with the room-temperature setup discussed before, we are able to measure one (I,Q) point for each period of the IF signal, which implies that our effective temporal resolution is 80 nanoseconds. For this reason, exploring the time-transient dynamics of the JPA chip is not possible unless we increase the IF frequency.

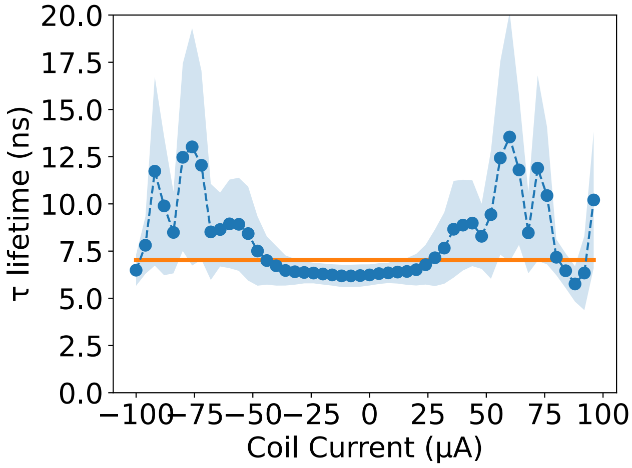

Figure 3.25: Average photon lifetime τ as function of the coil current. The blue-shaded region indicates the statistical error on the measured quantity, estimated as three times the standard deviation of the fit's estimators. The orange solid line indicates the weighted average of the measured values weighted inversely to their respective statistical errors.

3.5 Summary

In this chapter, we present the experimental techniques necessary for our thesis work. In the first section, we illustrate the setup used in this work, focusing on the cryogenic setup needed in order to generate the quantum states of light of interest. In the second section, we describe how the propagating microwave signals coming from the cryostat are digitized, demodulated and filtered. In particular, we describe the FPGA Image which was developed during this thesis work. In the third subsection, we illustrate the experimental method used to characterize the properties of the amplification chain. In particular, we show that, within the experimental errors, the amplification process generates gaussian noise. In the last section, we analyze the spectroscopic parameters of the superconducting devices in our setup, by measuring the complex reflection coefficient.

Chapter 4

Theory of Kerr non-linear resonators

In this chapter, we illustrate the theoretical model which can be used to interpret the experimental results obtained in this thesis work. The chapter is divided into three sections. In the first section, we derive a phenomenological single-mode Hamiltonian to describe the superconducting quantum devices used in our thesis: a JPA and a JPC operated in a single port configuration. The second section describes the theory behind the experiments involving the JPC. In an analogous way, the third section describes the theory behind the experiments involving the JPA.

4.1 Phenomenological Hamiltonian for superconducting quantum devices

In this section, we describe the theoretical framework used to model the superconducting quantum devices used in this thesis. In particular, we use a *lumped-element* model, in which we neglect the spatial extensions of our components, to derive a phenomenological Hamiltonian for our devices. The lumped element model is, of course, an approximation and it is not as accurate as a more complete *distributed-element* model, since the physical dimensions of our devices are comparable to the wavelength of the microwaves used during our experiments. Despite that, the use of the *lumped-element* model is justified by the following observations:

1. in our experiments, we assume to interact with only one of the quantum modes of the superconducting devices, i.e, we assume the validity of the single-mode approximation. This assumption is justified by the results of the reflection measurements performed on both our superconducting devices: indeed, for both of them, only one resonance frequency can be detected in the frequency range of interest. Moreover the JPC is used in a single port configuration, therefore we interact directly with only one of the two resonators in it;

2. in the single-mode approximation, the *lumped-element* and the *distributed-element* models converge to formally identical Hamiltonian operators [79]. The difference between the two models relies in different equations to estimate the parameters entering the Hamiltonian operators. In our experiments, we don't estimate them *a-priori*;

3. the lumped-element approach can also be justified *a posteriori*, since our experiments, shown in Chapter 5, agree with the theoretical predictions based on this approach.

The circuit under consideration includes the superconducting resonator, which is treated here as an LC-circuit with resonator inductance L_{res} and resonator capacitance C_{res}. These parameters can be estimated as

$$L_{\text{res}} = dL_0, \qquad C_{\text{res}} = dC_0, \tag{4.1}$$

where d is the lenght of the superconducting device and L_0 and C_0 are the inductance and capacitance per unit lenght, respectively. The angular resonance frequency ω_{res} of the bare superconducting resonator is given by

$$\omega_{\text{res}} = \frac{1}{\sqrt{L_{\text{res}} C_{\text{res}}}}. \tag{4.2}$$

For both the JPA and the JPC, we treat the DC-SQUID and the loop of Josephson junctions as single Josephson junctions with tunable critical current I_c, as explained in Chapter 1 for the DC-SQUID. We label the critical current of the effective Josephson junctions I_c. We also define the Josephson energy [45] of the effective Josephson junction as

$$E_J(\Phi_{\text{ext}}) = \frac{\Phi_0 I_c(\Phi_{\text{ext}})}{2\pi}, \tag{4.3}$$

where Φ_0 is the flux-quantum and we made explicit that the critical current I_c can be modulated by applying an external magnetic flux Φ_{ext}. Possible capacitive effects of either the the DC-SQUID of the JPA or the loop of junctions of the JPC are taken in account by a capacitance C_J. A schematic of the lumped-element model is shown in Fig. 4.1.

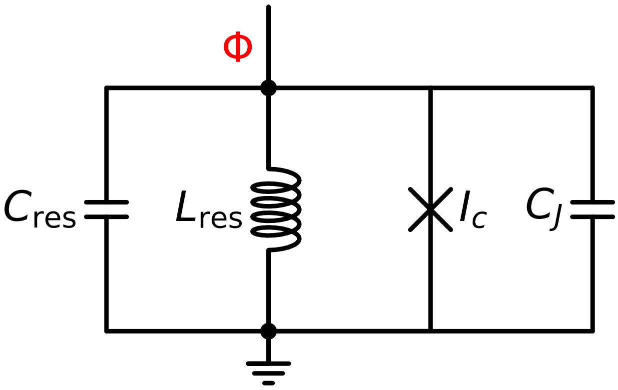

Figure 4.1: Lumped element model of the superconducting quantum devices used in this thesis.

Using a standard approach in circuit quantization [80], we define the canonical flux-node canonical variable Φ. We only need to define one canonical coordinate Φ since all the elements of the circuit under consideration are in parallel. Also, since we are considering a lumped element model, we neglect the dependence of Φ on the spatial coordinates and we allow it to only be a function of the time t. In terms of Φ, we can estimate the energy stored in each circuital component. Therefore, we can write down the circuit *Lagrangian* $\mathcal{L}(\Phi, \dot{\Phi})$ as

$$\mathcal{L}(\Phi, \dot{\Phi}) = \frac{C_\Sigma}{2}\dot{\Phi}^2 - \frac{\Phi^2}{2L_{\mathrm{res}}} + E_J(\Phi_{\mathrm{ext}}) \cos\left(\frac{\pi\Phi}{\Phi_0}\right), \tag{4.4}$$

where $C_\Sigma = C_J + C_{\mathrm{res}}$ is the total capacitance and Φ_{ext} is the external magnetic flux which modulates the critical current of the effective Josephson junction. To obtain the Hamiltonian function of this system, we introduce the canonical variable [81] conjugate to Φ, Q defined as

$$Q = \frac{\partial \mathcal{L}}{\partial \dot{\Phi}} = C_\Sigma \dot{\Phi}, \tag{4.5}$$

we note that Q has the physical dimensions of a charge. By performing a Legendre transform [82] of the Lagrangian function $\mathcal{L}$ with respect to Q, we obtain the classical Hamiltonian function of the system,

$$\mathcal{H}(\Phi, Q) = \frac{Q}{2C_\Sigma} + \frac{\Phi^2}{2L_{\mathrm{res}}} - E_J(\Phi_{\mathrm{ext}}) \cos\left(\frac{\pi\Phi}{\Phi_0}\right) \tag{4.6}$$

We can go from this classical Hamiltonian function to a Hamiltonian operator by transforming the classical variables Q and Φ in quantum operators $\hat{Q}$ and $\hat{\Phi}$ satisfying the canonical commutation relation [80],

$$\left[\hat{\Phi}, \hat{Q}\right] = \mathrm{j}\hbar\mathbb{I}, \tag{4.7}$$

where $\mathbb{I}$ denotes the identity operator. To obtain a simpler expression, when $\Phi \ll \Phi_0$, we can expand the cosine potential of the effective Josephson junction and keep only the terms up to fourth order,

$$\hat{H} = \frac{\hat{Q}}{2C_\Sigma} + \frac{\hat{\Phi}^2}{2L_{\mathrm{res}}} + \frac{\pi^2 E_J(\Phi_{\mathrm{ext}})}{2{\Phi_0}^2}\hat{\Phi}^2 - \frac{\pi^4 E_J(\Phi_{\mathrm{ext}})}{24\Phi_0^4}\hat{\Phi}^4. \tag{4.8}$$

In our experiments, $\Phi_{\mathrm{ext}} = \bar{\Phi}_{\mathrm{DC}} + \delta\Phi(t)$ where $\bar{\Phi}_{\mathrm{DC}}$ is set by direct current flowing in the superconducting coils attached to the devices, see Chapter 3, and $\delta\Phi(t)$ is a time-dependent external flux sent by using the pump-lines connected to our devices. In general, we assume that $\delta\Phi(t) \ll \bar{\Phi}_{\mathrm{DC}}$ and, therefore, we can use the first-order Taylor expansion

$$E_J(\Phi_{\mathrm{ext}}) = E_J(\bar{\Phi}_{\mathrm{DC}}) + \left|\frac{\partial E_J}{\partial \Phi_{\mathrm{ext}}}\right|_{\bar{\Phi}_{\mathrm{DC}}} \delta\Phi(t). \tag{4.9}$$

Whit this in mind, we can rewrite Eq. 4.8 as

$$\hat{H} = \frac{\hat{Q}^2}{2C_\Sigma} + \frac{\hat{\Phi}^2}{2L_\Sigma} + \frac{\pi^2}{2\Phi_0^2}\left|\frac{\partial E_J}{\partial \Phi_{\mathrm{ext}}}\right|_{\bar{\Phi}_{\mathrm{DC}}} \delta\Phi(t)\hat{\Phi}^2 - \frac{\pi^4 E_J(\bar{\Phi}_{\mathrm{DC}})}{24\Phi_0^4}\hat{\Phi}^4, \tag{4.10}$$

where we neglected the term $\delta\Phi(t)\hat{\Phi}^4$ and we have defined the total inductance L_Σ as

$$\frac{1}{L_\Sigma} = \frac{1}{L_{\text{res}}} + \frac{\pi^2 E_J(\bar{\Phi}_{\text{DC}})}{\Phi_0^2}. \tag{4.11}$$

At this point, we introduce the cavity bosonic modes $\hat{b}$ and $\hat{b}^\dagger$ as

$$\begin{aligned} \hat{Q} &= \mathrm{j}\sqrt{\frac{\hbar C_\Sigma \omega_0}{2}}\left(\hat{b}^\dagger - \hat{b}\right), \\ \hat{\Phi} &= \sqrt{\frac{\hbar\omega_0}{2C_\Sigma}}\left(\hat{b}^\dagger + \hat{b}\right), \end{aligned} \tag{4.12}$$

where the resonance angular frequency ω_0 of the superconducting device is given by

$$\omega_0(\bar{\Phi}_{\text{DC}}) = \frac{1}{\sqrt{L_\Sigma(\bar{\Phi}_{\text{DC}})C_\Sigma}}. \tag{4.13}$$

In terms of the bosonic operators $\hat{b}$ and $\hat{b}^\dagger$, we can rewrite the Hamiltonian in Eq. 4.10 as

$$\hat{H} = \hbar\omega_0(\bar{\Phi}_{\text{DC}})\hat{b}^\dagger\hat{b} + \hbar g(\bar{\Phi}_{\text{DC}})\delta\Phi(t)\left(\hat{b} + \hat{b}^\dagger\right)^2 - \frac{\hbar K(\bar{\Phi}_{\text{DC}})}{6}\left(\hat{b} + \hat{b}^\dagger\right)^4, \tag{4.14}$$

where $g(\bar{\Phi}_{\text{DC}})$ describes the strength of the coupling between the superconducting quantum device and the time-dependent external flux $\delta\Phi(t)$ and $K(\bar{\Phi}_{\text{DC}})$ is the tunable Kerr non-linearity of the superconducting quantum devices. These parameters are defined as

$$\begin{aligned} g(\bar{\Phi}_{\text{DC}}) &= \frac{\pi^2}{4\Phi_0^2}\left|\frac{\partial E_J}{\partial \Phi_{\text{ext}}}\right|_{\bar{\Phi}_{\text{DC}}}\left(\frac{\hbar\omega_0}{C_\Sigma}\right), \\ K(\bar{\Phi}_{\text{DC}}) &= \frac{\pi^4 E_J(\bar{\Phi}_{\text{DC}})}{16\Phi_0^4}\left(\frac{\hbar\omega_0}{C_\Sigma}\right)^2. \end{aligned} \tag{4.15}$$

4.2 Single photon driven oscillator

In this section, we illustrate the necessary theory to understand the experimental results obtained by analyzing the output field emitted by the JPC, based on the results of the previous section. The section is organized as follows: in the first subsection, we introduce and motivate the Hamiltonian operator used to model the JPC. In the second subsection, we focus on the steady-state solutions of the system equation of motion. The solutions are obtained using both mean-field and numerical techniques. In particular, we predict that the emitted signal from the JPC presents *anti-bunching* in the steady-state regime, see section 4.2.2. The third and last subsection deals with the time-transient dynamics of the model. The purpose of the last subsection is to shed some light on some physical features that is not explored experimentally during this thesis work and can inspire future works.

4.2.1 Driven non-linear oscillator

In our experiments, the JPC is probed in reflection with a weak microwave coherent tone generated by an SGS100A microwave source. The signal arrives at the JPC through a microwave circulator which suppresses (21 dB isolation) the signal coming from the other direction. A simplified setup is depicted in figure 4.2. We model the JPC as a non-linear single-mode quantum oscillator, described by four effective parameters: its resonance frequency f_0, its internal and external coupling factors γ_{int} and γ_{ext} and its non-linearity K. The first three parameters are estimated by measuring the reflection coefficient of the device, while, in principle, K can be estimated from the observed dispersive shift [83]. The resonance frequency and the non-linearity enter explicitly in the model Hamiltonian, while the coupling constants describe the dissipation to the external environment, as explained in Chapter 1.

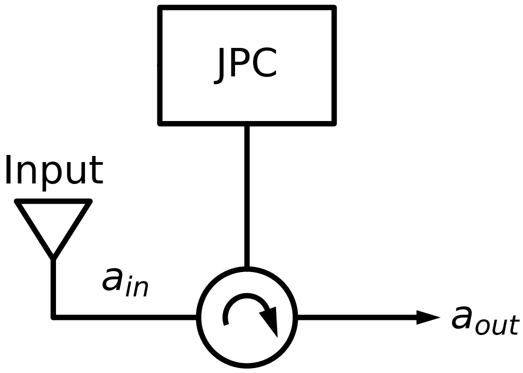

Figure 4.2: Simplified measurement scheme of the JPC.

We label $\hat{b}$ the operator describing the JPC-cavity mode. Starting from Eq. 4.14, the Hamiltonian of the JPC is assumed to be

$$H/\hbar = \omega_0 \hat{b}^\dagger \hat{b} - \frac{K}{6}\left(\hat{b} + \hat{b}^\dagger\right)^4, \tag{4.16}$$

where $\omega_0 = 2\pi f_0$. Also, we omitted the time-dependent flux $\delta\Phi(t)$ since it was not used for the JPC experiments. Moreover, we dropped the symbol $\bar{\Phi}_{\mathrm{DC}}$ for notation simplicity. Going in a frame rotating at the JPC resonance frequency f_0, the Hamiltonian can be simplified to

$$H/\hbar \approx -K\hat{b}^{\dagger 2}\hat{b}^2, \tag{4.17}$$

As explained in the first chapter, the input signal can be modeled by introducing a driving term in the rotated Hamiltonian operator, since it represents a classical signal,

$$H/\hbar = -K\hat{b}^{\dagger 2}\hat{b}^2 + \mathrm{j}\,\Omega\left(\hat{b}^\dagger - \hat{b}\right). \tag{4.18}$$

The term Ω is the *drive strength* and it is related to the input power P_{in} as explained in [83],

$$\Omega = \sqrt{\frac{\gamma_e P_{in}}{\hbar\omega_0}}. \tag{4.19}$$

Finally, the equation of motion for the intracavity mode $\hat{b}$ is given by

$$\frac{d}{dt}\hat{b} = 2\mathrm{j}K\,\hat{b}^{\dagger}\hat{b}^{2} - \frac{\gamma}{2}\hat{b} - \Omega. \tag{4.20}$$

The output mode $\hat{a}_{out}$ is given from the boundary condition

$$\hat{a}_{out} = \sqrt{\gamma_{ext}}\left(\Omega - \mathrm{j}\hat{b}\right). \tag{4.21}$$

4.2.2 Steady-state solution

In this subsection, we discuss the steady-state solution to the equation of motion for the mode $\hat{b}$. The steady-state solution is obtained by imposing that

$$\frac{d}{dt}\hat{b} = 0, \tag{4.22}$$

which gives us

$$2\mathrm{j}K\,\hat{b}^{\dagger}\hat{b}^{2} - \frac{\gamma}{2}\hat{b} - \Omega = 0. \tag{4.23}$$

Mean-Field solution

The mean-field (MF) steady-state solution is obtained by replacing the operator $\hat{b}$ with its expectation value $B = \langle\hat{b}\rangle$ in equation 4.23. Physically, this approximation is justified when the quantum fluctuations associated with $\hat{b}$, $\delta b = \sqrt{\mathrm{var}(\hat{b})}$, are much smaller than the average value B. The MF equation reads as

$$2\mathrm{j}K\,|B|^2 B - \frac{\gamma}{2}B - \Omega = 0 \tag{4.24}$$

The MF solution is useful to develop some intuition about our system. In general, it is not possible to solve equation 4.24 analytically. Therefore, we start by analyzing some simple limiting cases. First, we analyze the linear solution, obtained in the case $K = 0$. In this situation, the MF equation has a single solution given by

$$B_{K=0} = \langle\hat{b}\rangle = \frac{2\Omega}{\gamma}. \tag{4.25}$$

In the linear case, the input field Ω displaces the intracavity mode $\hat{b}$. The amplitude of the displacement scales linearly with the drive strength of the input field. For small, but non-zero non-linearity K, we can simplify equation 4.23 by replacing the term $|B|^2$ with $|B_{K=0}|^2 = 4\Omega^2/\gamma^2$.

In this case, the solution is given approximately by

$$B \approx \frac{\Omega}{8\mathrm{j}\,K\frac{\Omega^2}{\gamma^2} - \gamma/2}, \tag{4.26}$$

which holds true for weak input signals $\Omega \leq \gamma$. The solution 4.26 shows that the non-linearity K suppresses the displacement done by the field Ω in the intra-cavity field. To understand why this happens, we observe that equation 4.24 can be formally rewritten as

$$\left(2\mathrm{j}K|B|^2 - \frac{\gamma}{2}\right) B = \Omega, \tag{4.27}$$

in which it's clear that the nonlinear term $2K|B|^2$ acts as an effective frequency detuning. Since $|B|^2$ increases for stronger input fields, the resonance frequency of our system shifts, and thus the coherent tone is no longer resonant, leading to a reduced displacement of the intra-cavity field. This observation is generally used to measure the Kerr non-linearity, as described in Ref. [83].

Numerical solution

Despite providing useful insights on the role played by the non-linearity on the displacement of the intra-cavity field, the MF solution is based on an essentially classical theory and therefore cannot predict any quantum feature of the steady-state mode of the driven JPC. Therefore, this section is dedicated to the solution of the steady-state equation 4.23 without further approximations. The solutions of this equation are used to compute some expectation values that are relevant to the analysis of the quantum physical features of the driven JPC steady-state. The computations are performed as explained in section 1.3: the steady-state density matrix of the JPC is found by diagonalizing the matricization of the Liouvillan super-operator which describes the system. We focus on expectation values which require only up to the second moment of the cavity operator $\hat{b}$. The chosen steady-state expectation values are

1. mean photon number $n_b = \langle \hat{b}^\dagger \hat{b} \rangle$;
2. average displacement $B = \langle \hat{b} \rangle$;
3. second-order correlation function $g^{(2)}$, computed as

$$g^{(2)} = \frac{\langle b^\dagger b^\dagger b b \rangle}{n_b^2}; \tag{4.28}$$

4. deviation from mean-field prediction for the photon number, quantified by the parameter r, defined as

$$r = \frac{n_b}{|B|^2}. \tag{4.29}$$

   The more r deviates from $r = 1$, the more is system behavior different from the MF theory prediction.

Results of numerical simulations

For the numerical simulations, we choose $\gamma = 1$ MHz, which is similar to the measured value for the JPC. We express K and Ω as multiples of γ for simplicity. The steady-state solution is examined for $K/\gamma = \left[0, 0.5, 1, 1.5, 2, 2.5\right]$ and for Ω ranging from 0 to 5γ. The maximum value 5γ is chose to keep the cutoff dimension of the Hilbert space to $D_c = 100$.

In figure 4.3, we show the average cavity photon population and the average displacement amplitude as a function of the drive-strength Ω for different values of the non-linearity K. The results confirm our intuition: for higher non-linearities, the displacement of the intracavity field is suppressed due to the detuning between the cavity and the input field caused by the non-linearity.

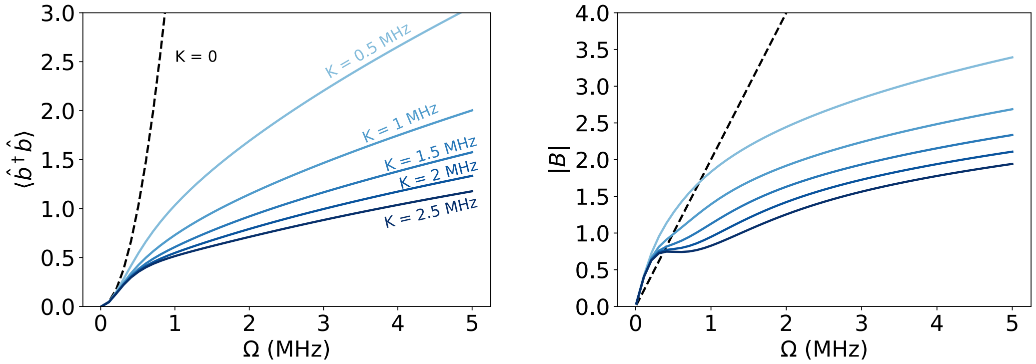

(a) **(b)**

Figure 4.3: Average cavity photon population, figure (a), and average displacement amplitude, figure (b) as function of the drive-strength Ω for different values of the non-linearity K.

Interestingly, as shown in figure 4.4, the second order correlation function $g^{(2)}$ of the steady-state is always smaller than 1 for the range of parameters considered. This implies that the light emitted by the JPC is *anti-bunched* and preserves some quantum features in the steady state. The second order correlation function $g^{(2)}$ gets smaller by increasing the non-linearity (going from light-blue to dark-blue curves in figure 4.4). For all the considered values of the non-linearity K, $g^{(2)}$ is an increasing function of Ω, reaching $g^{(2)} = 1$ asymptotically in the limit $\Omega \to 1$. This fact can be explained by noting that when $\Omega \to \infty$, eventually $\Omega \gg K$ and therefore the detuning between the cavity and the drive signal caused by the non-linearity becomes irrelevant. When that happens, the field inside the cavity is a displaced coherent state with good approximation, thus justifying $g^{(2)} = 1$.

The non-classicality of the light emitted in the steady-state is confirmed by the analysis of the r parameter. When the system is classical, $\hat{b}$ can be replaced by complex number, as it is assumed in the MF theory. In this case, the numerator and denominator in the definition of r are equal, and then $r = 1$. When quantum fluctuations are relevant, $\hat{b}$ cannot be approximated as a complex number. In this case, $\langle \hat{b}^\dagger \hat{b} \rangle \neq |\langle \hat{b} \rangle|^2$ and then the $r > 1$.

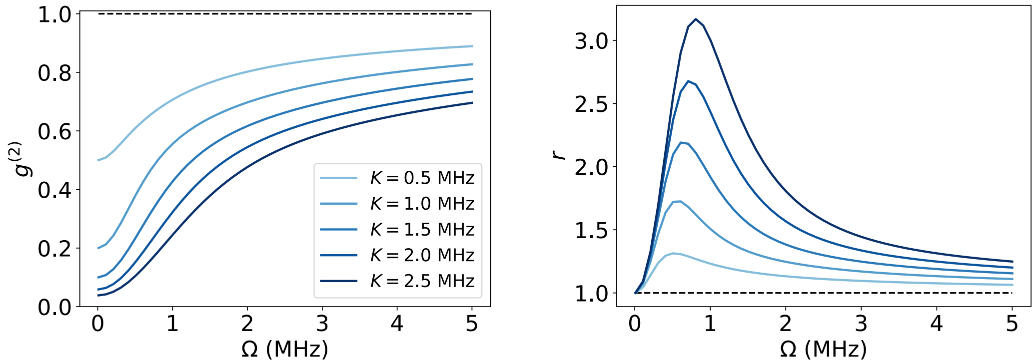

(a) **(b)**

Figure 4.4: Second order correlation function $g^{(2)}$, figure (a), and r-parameter, figure (b) as a function of the drive-strength Ω for different values of the non-linearity K.

For all values of K, r is peaked at intermediate values of $\Omega \approx \gamma$, before decreasing in the limit $\Omega \to \infty$, when the intra-cavity steady-state solution approaches a classical coherent state. In figure 4.5 we show the Wigner function of the steady-state solution for $K = 2$ MHz and $\Omega = \gamma = 1$ MHz. In this intermediate case, it is clear that the Wigner function is far from a Gaussian distribution. By looking at the photon number distribution for this state, we note that only the Fock states $|0\rangle$ and $|1\rangle$ significantly populated.

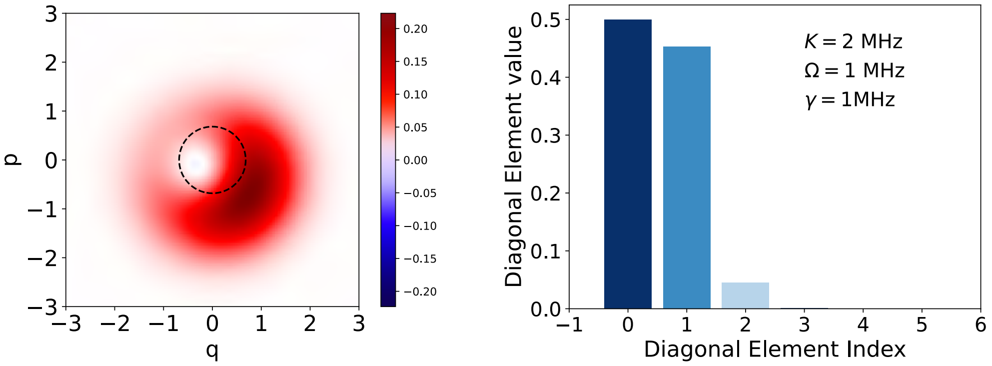

(a) **(b)**

Figure 4.5: Wigner function, figure (a), and photon-number distribution, figure (b), for $K = 2$ MHz and $\Omega = 1$ MHz. The black dashed line indicates the contour of the vacuum state $|0\rangle$.

4.2.3 Beyond steady-state: transient solutions

To obtain information about the time transient features of the system under consideration, we move to the Schroedinger picture and solve the master equation:

$$\frac{d}{dt}\rho(t) = \mathcal{L}\left(\rho(t)\right), \tag{4.30}$$

where $\rho(t)$ is the intra-cavity transient density matrix and $\mathcal{L}$ is the Liovillan super-operator defined in 1.43. In particular, we show that the anti-bunching predicted in the steady state is a consequence of quantum superposition effects in the transient time evolution. We focus on the case $K = 2$ MHz and $\Omega = 1$ MHz. This choice is motivated as follows: $K = 2$ MHz is a realistic value for the non-linearity of the device under consideration and $\Omega = 1$ MHz is around the value of the drive-strength for which the deviations of the steady-state solution from the MF theory are stronger, as we can clearly see for the simulation results of the r parameter. Also, the antibunching in the steady state is predicted for a wide range of parameters, as long as $K \gtrapprox \gamma$. Therefore we expect that the conclusions drawn for this particular case can be generalized for a wider set of parameters.

For the selected values of K and Ω we fix the dimensional cutoff of our system to $D_c = 40$. The relevant time scale for the system's dynamics is given by $1/\gamma \approx 1\ \mu$s. For this reason, discretize the time interval first by fixing the full simulation duration to $t_f = 5\ \mu$s, which is long enough for the system to reach the steady state, and then we divide it into 1000 steps. Therefore our simulation has a time resolution of 5 ns, which is short enough to capture the relevant transient dynamical features. The numerical solution of the time-dependent master equation is obtained using the master equation solver of the *QuTiP* package [41], which implements a fourth-order Runge Kutta method in a numerically efficient way.

As shown in figure 4.6, we started our analysis by plotting the correlation function $g^{(2)}$ and the displacement amplitude, $|\langle \hat{b} \rangle|$, as a function of time. We observe that $g^{(2)}(0) = 1$, as expected since we start from the vacuum state in the cavity. The correlation function $g^{(2)}(t)$ then quickly decreases, reaching its minimum value, $g^{(2)} = 0.28$, for t =1.805 μs. For longer times, the correlation function stabilizes slowly fluctuating around the steady-state value.

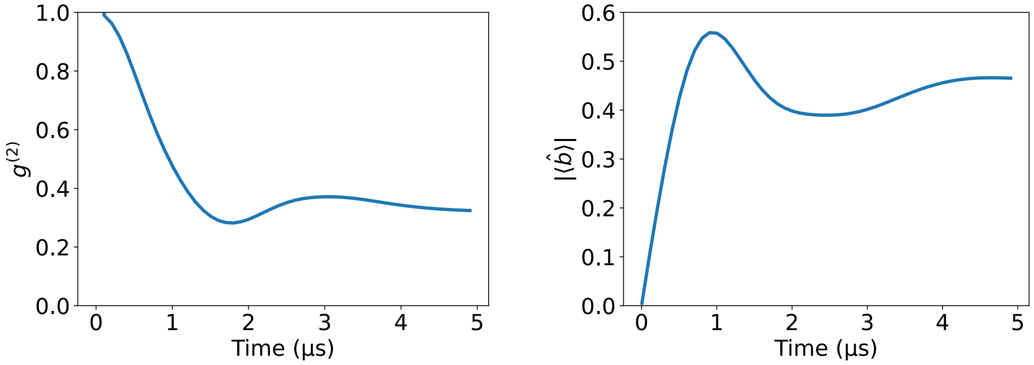

(a) **(b)**

Figure 4.6: Figure (a): $g^{(2)}$ correlation function for the transient cavity state as a function of time. Figure(b): Absolute value of the expectation value of the operator $\hat{b}$ as a function of time.

The displacement amplitude, for comparison, increases linearly from $t = 0$ to $t \approx 1\ \mu$s. For $t \gtrapprox 1\ \mu$s the number of noise photons in the cavity, shown in figure 4.7, is big enough to shift the resonance frequency of the JPC, thus decoupling the device from the resonant drive. When the cavity is off-resonance with the input drive, the number of photons inside of it starts to relax by the effect of the dissipation to the environment. This relaxation justifies the decrease of the displacement amplitude and the number of photons between $t = 1\mu$s and $t = 3\ \mu$s. By losing photons to the external environment, the detuning between the cavity and the external input field slowly reduces. When the external drive and the cavity are partially in resonance again, the photon number inside the cavity slightly increases together with the displacement amplitude between $t = 3\mu$s and $t = 5\ \mu$s before stabilizing around the steady-state value.

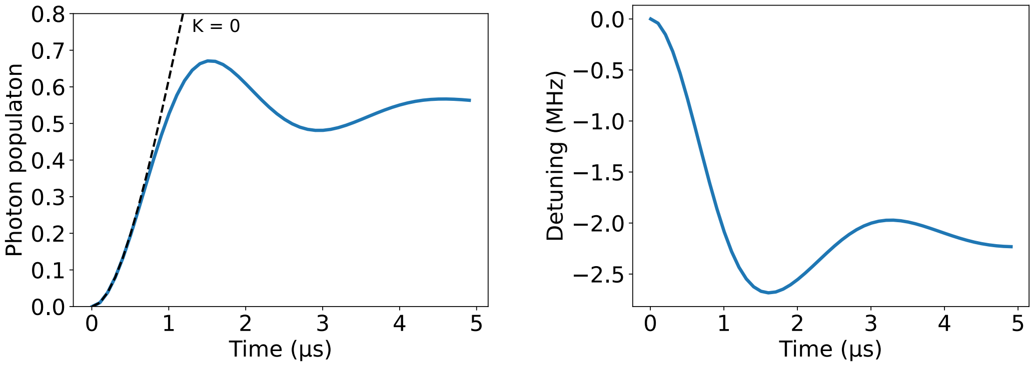

(a) **(b)**

Figure 4.7: Figure (a): Intra-cavity photon population $\langle\hat{b}^\dagger\hat{b}\rangle$ of time. The black dotted line indicates the analytical solution for the case $K = 0$. Figure(b): Detuning between the cavity and the input coherent tone as a function of time. The detuning is compute as $\Delta = -2K\langle\hat{b}^\dagger\hat{b}\rangle$.

At this point, we explored the role played by quantum superposition in the transient state dynamics. From the analysis of the steady state, it is clear that the steady-state photon distribution is almost equally split between the Fock states $|0\rangle$ and $|1\rangle$, as shown in figure 4.5. Inspired by this fact, we study the fidelity of the transient state with the superposition state $\left|\psi_{tar}\right\rangle$ defined as

$$\left|\psi_{tar}\right\rangle = \frac{1}{\sqrt{2}}\left(|0\rangle + |1\rangle\right). \tag{4.31}$$

The results are shown in figure 4.8, together with the negative volume of the transient state as a function of time. The negative volume is estimated from the Wigner W function of the transient state by

$$V_N = \iint \left|W(z)\right| - 1. \tag{4.32}$$

As expected, the fidelity reaches values up to 95%, for $t \approx 1.3\ \mu$s. Around the same time, the negative volume reaches its maximum value, $V_N \approx 0.1$. It is important to note, that the negative volume is substantially higher than 0 for a time internal longer than 1 μs and thus experimentally accessible. This observation confirms the link between quantum superposition and negativities in the Wigner function.

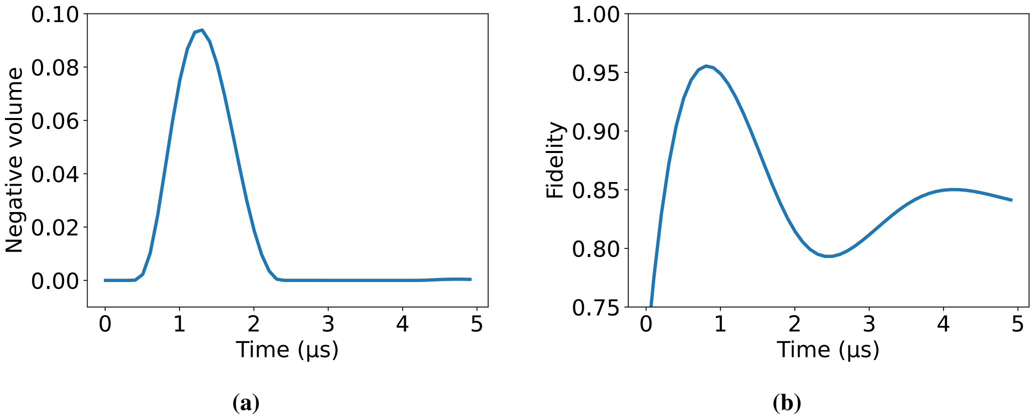

Figure 4.8: Figure (a): Negative volume of the transient state as a function of time. Figure (b): Fidelity of the transient state with respect to the pure state $\left|\psi_{tar}\right\rangle$ as a function of time.

In figure 4.9, we plot the purity of the transient state as a function of time. The purity is estimated by

$$P(t) = \mathrm{Tr}\left(\hat{\rho}(t)^2\right). \tag{4.33}$$

The purity of the system decreases quickly from $P = 1$ at $t = 0$ to the minimum value $P \approx 0.6$ when $t \gtrapprox 2$ μs. The system has its lowest value in purity when the detuning between the cavity and input drive is the biggest. After $t = 2$ μs, the purity increases slowly, with the same mechanics described for the photon number and the displacement amplitude. When the transient system state has fidelity $F \approx 95\%$ with the target state $\left|\psi_{tar}\right\rangle$, the purity is still high, $P \approx 0.8$.

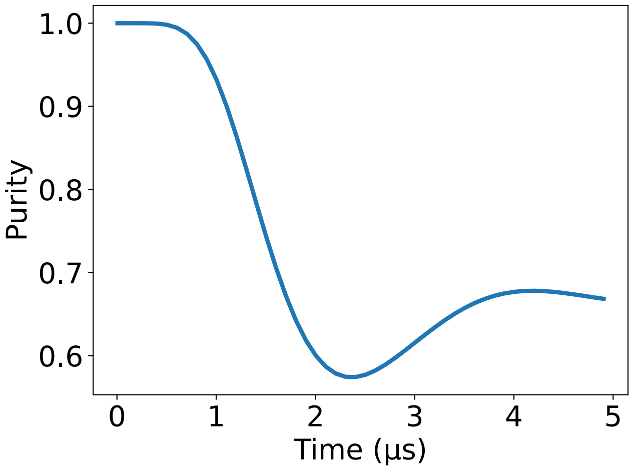

Figure 4.9: Purity of the transient state as a function of time.

We conclude the time-domain analysis by comparing the Wigner functions of the transient state at $t = 1.3\ \mu s$ and the Wigner function of the target state $\left|\psi_{tar}\right\rangle$, figure 4.10.

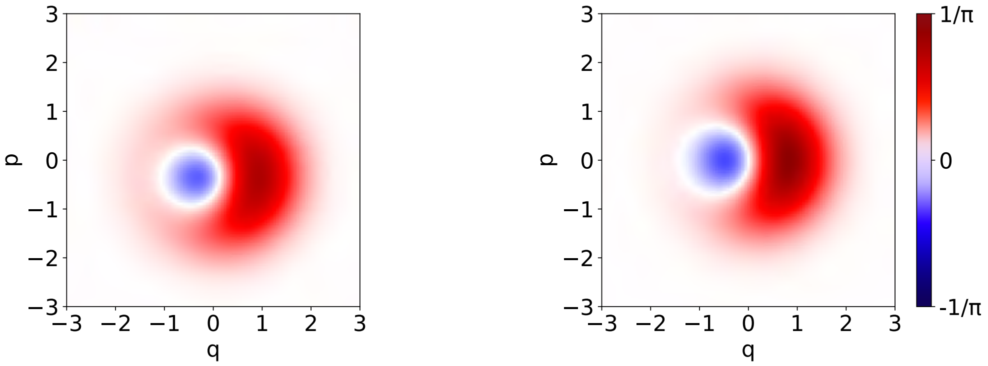

(a) **(b)**

Figure 4.10: Figure (a): Wigner function of the transient state for $t = 1.36\,\mu$s. The fidelity with the pure state $|\psi_{tar}\rangle$ is 92%. Figure (b): Wigner function of the pure state $|\psi_{tar}\rangle$.

4.3 Two-photon driven oscillator: Kerr Parametric Oscillator

In this section, we illustrate the necessary theory to understand the experimental results obtained by analyzing the output field emitted by the JPA. The section is organized as follows: in the first subsection, we describe the physics of the device in the linear regime, when the non-linearity can be neglected. In the second section, we explore analytically the effects of the non-linearity using the mean-field approximation. In the third and last section, we use the numerical techniques defined in the previous chapters to analyze the full quantum theory of the JPA physics, linking the linear and mean-field analytical theories.

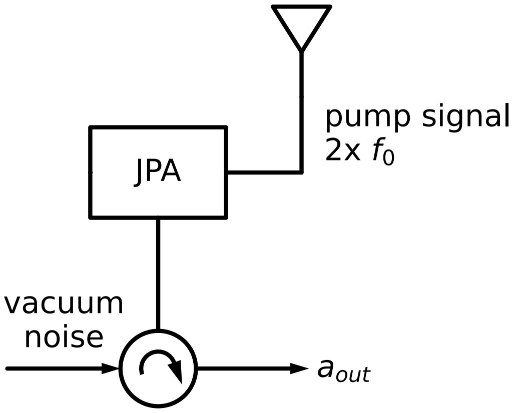

Figure 4.11: Simplified measurement scheme for the JPA.

Usually, the quantum features of the microwave radiation emitted by a JPA can be accounted for by modeling it with the Hamiltonian defined in Eq. 4.14. Here, we assume that the external time-dependent flux depends follows the time dependence:

$$\delta\Phi(t) = A\cos(2\omega_0 t + \phi), \tag{4.34}$$

where A is the pump amplitude, ϕ is the pump phase, and ω_0 is the resonance frequency of the superconducting device. In the following, we drop the symbol $\bar{\Phi}_{\mathrm{DC}}$ to simplify our notation. We also define the pump strength absolute value $|U|$ as

$$|U| = gA. \tag{4.35}$$

The Hamiltonian for the JPC therefore reads as

$$\hat{H}/\hbar = \omega_0 \hat{b}^\dagger \hat{b} + |U| \cos(2\omega_0 t) \left(\hat{b} + \hat{b}^\dagger\right)^2 - \frac{K}{6} \left(\hat{b} + \hat{b}^\dagger\right)^4 . \tag{4.36}$$

In a frame rotating with the JPA frequency ω_0, the Hamiltonian in the last equation implies to the Hamiltonian of a KPO [13, 79],

$$H_{KPO} = -K b^{\dagger^2} b^2 + U b^{\dagger^2} + U^* b^2. \tag{4.37}$$

where the complex pump amplitude U is given by $U = |U| e^{\mathrm{j}\phi}$. In the following, we set the pump phase to $\phi = 0$ and treat U as a real parameter.

4.3.1 Linear Theory

When the Kerr non-linearity K is not present, the Hamiltonian of the KPO is quadratic in the field operator $\hat{b}$ and, therefore, the equations of motion are linear. This feature greatly simplifies the study of the system's dynamics. Indeed, in this case, the Liovillian super-operator which appears in equation 1.41 is a *Gaussian Preserving Map* and the system's density matrix describes a single-mode gaussian state for any moment in time (proved in [84]). The covariance matrix $\mathbf{\Sigma}$ is defined in terms of the quadrature operators

$$\begin{aligned} \hat{q} &= \frac{b + b^\dagger}{\sqrt{2}} \\ \hat{p} &= \frac{b - b^\dagger}{\sqrt{2}\mathrm{j}} \end{aligned} \tag{4.38}$$

and be evaluated as

$$\mathbf{\Sigma} = \begin{pmatrix} \mathrm{var}(\hat{q}) & \langle \hat{q}\hat{p} + \hat{p}\hat{q} \rangle/2 \\ \langle \hat{q}\hat{p} + \hat{p}\hat{q} \rangle/2 & \mathrm{var}(\hat{p}). \end{pmatrix} \tag{4.39}$$

From the equation of motion of the mode $\hat{b}$, it is possible to prove that the equation of motion for the covariance matrix $\mathbf{\Sigma}$ is

$$\frac{d}{dt}\mathbf{\Sigma} = \boldsymbol{W}\mathbf{\Sigma} + \mathbf{\Sigma}\boldsymbol{W}^\dagger + \boldsymbol{F}, \tag{4.40}$$

where the matrices $\boldsymbol{W}$ and $\boldsymbol{F}$ are defined as

$$\boldsymbol{W} = \begin{pmatrix} -\gamma/2 & -2U \\ -2U & -\gamma/2 \end{pmatrix} \tag{4.41}$$

and

$$\boldsymbol{F} = \begin{pmatrix} \gamma/2 & 0 \\ 0 & \gamma/2 \end{pmatrix}. \tag{4.42}$$

From the definition, it is clear that equation 4.40 returns a physical covariance matrix only if

$$\det(\boldsymbol{W}) = 4\left(\frac{\gamma^2}{16} - U^2\right) \geq 0. \tag{4.43}$$

and thus the linear theory breaks down for $U > U_c = \gamma/4$. We refer to U_c as the pump-threshold. The equation for the steady state covariance matrix $\boldsymbol{\Sigma}_{ss}$ is given by taking the limit $t \to \infty$ in equation 4.40 and is a Lyapunov-type matrix [85],

$$\boldsymbol{W}\boldsymbol{\Sigma}_{ss} + \boldsymbol{\Sigma}_{ss}\boldsymbol{W}^{\dagger} = -\boldsymbol{F}. \tag{4.44}$$

which can be solved exactly and gives

$$\boldsymbol{\Sigma}_{ss} = \begin{pmatrix} \frac{\gamma^2/2}{16U^2-\gamma^2} & \frac{2U\gamma}{16U^2-\gamma^2} \\ \frac{2U\gamma}{16U^2-\gamma^2} & -\frac{\gamma^2/2}{16U^2-\gamma^2} \end{pmatrix}. \tag{4.45}$$

It is known experimentally that JPAs can be used to generate squeezed-vacuum states of microwave radiation. To do so, we start by defining the rotated covariance matrix

$$\boldsymbol{\Sigma}(\theta) = \boldsymbol{\Lambda}(\theta)\,\boldsymbol{\Sigma}\boldsymbol{\Lambda}(\theta)^T, \tag{4.46}$$

where $\boldsymbol{\Lambda}(\theta)$ is the rotation matrix,

$$\boldsymbol{\Lambda}(\theta) = \begin{pmatrix} \cos(\theta) & -\sin(\theta) \\ \sin(\theta) & \cos(\theta). \end{pmatrix} \tag{4.47}$$

The first entry of the rotated covariance matrix $\boldsymbol{\Sigma}(\theta)$ gives the variance of the rotated quadrature operator $q(\theta)$.

$$\mathrm{var}(q(\theta)) = \boldsymbol{\Sigma}(\theta)_{00} = \frac{\gamma}{8}\frac{\left(\gamma/4 - U\sin(2\theta)\right)}{\left(\left(\gamma/4\right)^2 - U^2\right)}. \tag{4.48}$$

Here we define the variance of an operator $\hat{O}$, $\mathrm{var}(\hat{O})$ as

$$\mathrm{var}(\hat{O}) = \mathbb{E}(\hat{O}^2) - \mathbb{E}(\hat{O})^2, \tag{4.49}$$

where $\mathbb{E}$ denotes the expectation value operator. Physically, the $\mathrm{var}(q(\theta))$ quantifies the spread of the Wigner function of the quantum state along the θ-axis of the phase space. When the variance $\mathrm{var}(q(\theta))$ is smaller than the variance of the vacuum fluctuations, $1/2$ photons, the system is in a squeezed-vacuum state. For any physical allowed value for the pump $U \leq U_c$, the variance $\mathrm{var}(q(\theta))$ is maximal for $\theta = 3\pi/4$ and minimal for $\theta = \pi/4$.

$$\begin{aligned}\mathrm{var}(q(\pi/4)) &= \frac{\gamma}{8\left(\gamma/4 + U\right)}\\ \mathrm{var}(q(3\pi/4)) &= \frac{\gamma}{8\left(\gamma/4 - U\right)}.\end{aligned} \tag{4.50}$$

In particular, we observe that for any value of the pump the variance along the axis $\theta = \pi/4$ is smaller compared to the one vacuum one. This means that for any $0 < U \leq U_c$, the system is in a squeezed vacuum state. When U approaches the critical value U_c, the variance along the axis $\theta = 3\pi/4$ diverges, going to infinity. For the axis, $\theta = \pi/4$, the variance $\mathrm{var}(q(\pi/4))$ does not go to zero but saturates to its minimum value $1/4$, which is half of the variance of the vacuum state. A quantity commonly used in experiments is the squeezing level $S(\theta)$ with respect to the vacuum, defined as

$$\begin{aligned}S(\theta) &= 10\log_{10}\left(\frac{\mathrm{var}(q(\theta))}{\mathrm{var}(q_{vac})}\right)\\ &= 10\log_{10}\left(2\mathrm{var}(q(\theta))\right).\end{aligned} \tag{4.51}$$

In terms of squeezing compared to the vacuum, when UU_c, the squeezing level is

$$\begin{aligned}S(3\pi/4) &= \infty\\ S(\pi/4) &= 10\log_{10} 2\mathrm{var}(q(\pi/4)) \approx -3\text{ dB}\end{aligned} \tag{4.52}$$

the saturation value of the squeezing along the $\pi/4$ axis is know as the 3dB-squeezing limit.

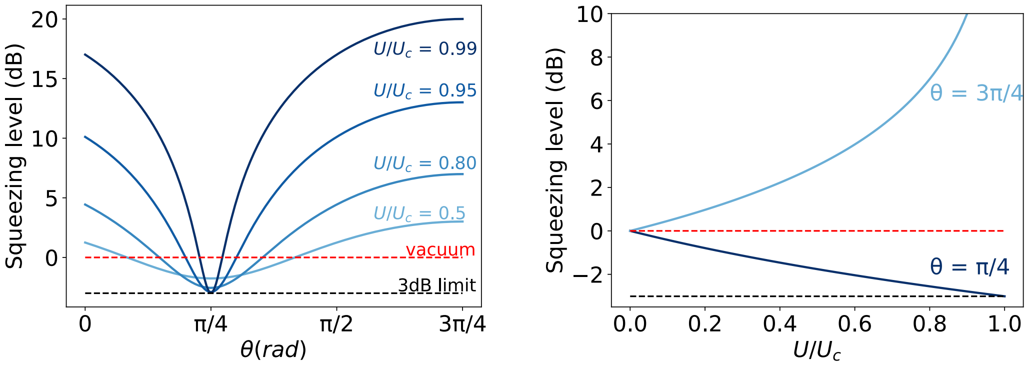

(a) **(b)**

Figure 4.12: Panel (a) shows the analytical squeezing level as a function of the quadrature θ for different values of the ratio U/U_c. Panel (b) shows the squeezing level for the quadratures $\theta = \pi/4$ (dark-blue line) and $\theta = 3\pi/4$ (light-blue line) as a function of the ratio U/U_c. The red dashed line indicates zero squeezing level (vacuum fluctuations) and the black dashed line indicates the −3 dB limit for the intracavity squeezing.

In conclusion, linear theory predicts that the intra-cavity mode $\hat{b}$ describes a squeezed vacuum state for any value of the pump below the threshold, $U \leq U_c$. For $U > U_c$, the theory breaks down and it is not possible to compute expectation values in the framework of Gaussian states. Physically, the breakdown of the linear theory can be interpreted using a simple qualitative argument. Indeed, if we consider the Hamiltonian H_{KPO} with $K = 0$, the system reaches a steady state because it can find an equilibrium between two competing process: the squeezing from the pump and the dissipation to the environment. Indeed, he pump creates two excitations in the system with a rate given by U. Due to the decay rate γ, the system loses a single excitation to the environment with a rate $\gamma/2$. When $2U < \gamma/2$, the system is able to dissipate in the environment the excitations coming from the pump, and then it can reach an equilibrium steady state. When $2U > \gamma/2$, the dissipation can't compensate for the rate of photon creation by the pump and therefore the system does not reach an equilibrium steady state. Indeed, using the covariance matrix formalism, we can estimate the steady-state number of photons in the cavity as

$$n = \langle \hat{b}^\dagger \hat{b} \rangle = \frac{1}{2} \frac{U^2}{\left(\gamma/4\right)^2 - U^2}. \tag{4.53}$$

As can readily be evaluated, the number of photons diverges for $U \to U_c$. This corroborates our interpretation of the dynamics of the system.

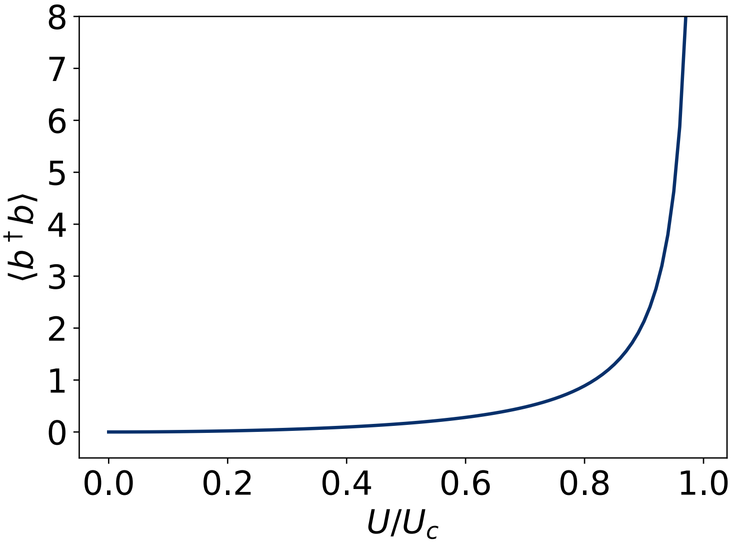

Figure 4.13: Steady-state cavity photon number $\langle \hat{b}^\dagger \hat{b} \rangle$ as a function of the ratio U/U_c

4.3.2 Mean-Field Theory

To understand the physics beyond the pump threshold, it is necessary to reintroduce the non-linearity K. From Chapter 1, we know that our cavity operator $\hat{b}$ obeys the *Quantum Langevin Equation* 1.39,

$$\frac{d}{dt} b = -\frac{\mathrm{j}}{\hbar} \left[H_{KPO}, b \right] - \frac{\gamma}{2} b + \mathrm{j} \sqrt{\gamma_e} a_{in} \tag{4.54}$$

the Hamiltonian H_{KPO} defined in equation 4.37 and γ_e and γ being respectively the external coupling factor and the decay rate of the KPO. Formally, the commutator $\left[H_{KPO}, b\right]$ can be evaluated as

$$\left[H_{KPO}, b\right] = -\frac{\partial H_{KPO}}{\partial b^\dagger} = 2\mathrm{j}Kb^\dagger b^2 - 2\mathrm{j}U\, b^\dagger. \tag{4.55}$$

Thus, the equation of motion for the cavity mode b is

$$\frac{d}{dt}b = 2\mathrm{j}Kb^\dagger b^2 - 2\mathrm{j}U\, b^\dagger - \frac{\gamma}{2}b + \mathrm{j}\,\sqrt{\gamma_e}a_{in}. \tag{4.56}$$

The mean-field steady-state equation reads

$$2\mathrm{j}\, K\, |B|^2\, B - 2\mathrm{j}\, UB - \frac{\gamma}{2}\, B = 0. \tag{4.57}$$

We rewrite $B = \sqrt{\bar{n}}e^{i\varphi}$, with $\bar{n} \in \mathbb{R}^+$ and $\varphi \in [0, 2\pi)$. In terms of the new parameters, we can easily evaluate the solutions to equation 4.57. Indeed, when $U \leq U_c = \gamma/4$, the system has only one steady state, corresponding to $\bar{n} = 0$. This is what we expect from linear theory, since we derived that when $U \leq U_c$ the intracavity state is not displaced and therefore $\langle\hat{b}\rangle = 0$.
Interestingly, when $U > U_c$, the system has two additional solutions for the steady state:

$$\begin{aligned} \varphi &= \frac{1}{2}\arcsin\frac{4\gamma}{U} + k\pi \ \text{ where } k = 0{,}1 \\ \bar{n} &= \frac{U}{|K|}\sqrt{1 - \left(\frac{\gamma}{4U}\right)^2}, \end{aligned} \tag{4.58}$$

which are symmetric by inversion in the phase space. A linearized stability analysis of these solutions, in [86], shows that below the pump-strength threshold $U \leq U_c$, the solution with $\bar{n} = 0$ is stable. When $U > U_c$, $\bar{n} = 0$ became unstable and the two solutions 4.58 are stable.
In the framework of the mean-field theory, the average photon number population $\bar{n} = |B|^2$ can be interpreted as the order parameter for a second-order phase transition [20]. Indeed, when $U \leq U_c$, $\bar{n} = 0$ and the mean-field theory predicts a single stable solution at the center of the phase space. When $U > U_c$, the situation changes drastically, since the system is described by two bistable solutions.

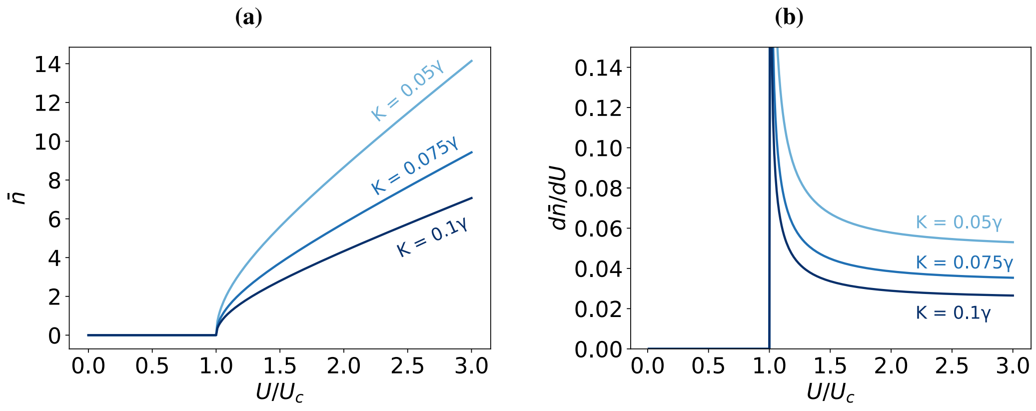

Figure 4.14: Panel (a) shows the steady state number of photons $\bar{n}$ as a function of the ratio U/U_c predicted by the Mean Field theory for different values of the non-linearity K. Panel (b) shows the derivative of $\bar{n}$ with respect to U/U_c as a function of U/U_c for different values of the non-linearity K.

4.3.3 Quantum theory

Quantum theory without dissipation

We start by observing that the displaced coherent states $|\alpha\rangle$, with $\alpha = \pm\sqrt{U/K}$, are degenerate eigenvector sof the KPO Hamiltonian, with associated eigenvalue $E_\alpha = U^2/K$. The subspace spanned by the coherent states $|\alpha\rangle$ and $|-\alpha\rangle$ is separated from the remaning part of the spectrum of the KPO hamiltonian by a finite energy gap E_{gap}. We refer to this subspace as the "degenerate subspace". Also, we note that all the superposition of the states $|\alpha\rangle$ and $|-\alpha\rangle$ are part of this subspace. In particular, the cat states

$$\begin{aligned} C^{+}(\alpha) &= \mathcal{N}\left(|\alpha\rangle + |\alpha\rangle\right), \\ C^{-}(\alpha) &= \mathcal{N}\left(|\alpha\rangle - |\alpha\rangle\right), \end{aligned} \tag{4.59}$$

are part of the degenerate subspace. The size of the energy spectrum gap E_{gap} increases as a function of U for all the values of K. This statement can be easily motivated by numerically diagonalizing the Hamiltonian of the KPO using the Lanczos method. In Fig. 4.15, we show the energy gap E_{gap} as a function of the pump strength U. In agreement with quantum perturbation theory, the gap scales quadratically in U for $U \ll K$ and it scales linearly in as a function of U for $U \gg K$.

The presence of the finite energy gap can be exploited to generate quantum superposition of displaced coherent states, such as cat-states, in the transient regime of the KPO, by exploiting the quantum adiabatic theorem [87]. This procedure was introduced theoretically by S. Puri et al. in [13] and experimentally verified by Z. Wang et al. in 2019 [15] in the microwave regime. The adiabatic theorem may also be used to generate controlled Rabi oscillatons between the coherent states $|\alpha\rangle$ and $|-\alpha\rangle$. This can be done by removing the degeneracy of the KPO Hamiltonian, by introducing a weak resonant driving term $\Omega\left(\hat{b}^\dagger + \hat{b}\right)$ in the KPO Hamiltonian. If the resonant

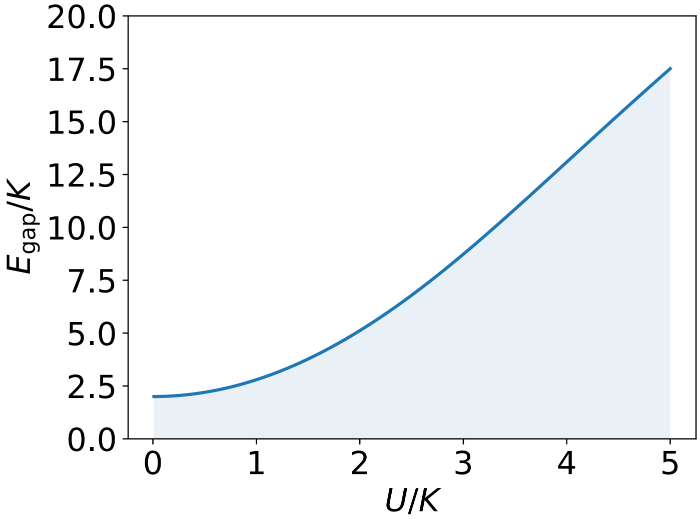

Figure 4.15: Energy gap E_{gap} of the KPO, expressed as a fraction of K, as a function of the pump power U, expressed as fraction of K.

drive is weak enough, $\Omega \ll E_{\text{gap}}$, the system is still confined in the degenerate subspace and coherent oscillations between $|\alpha\rangle$ and $|-\alpha\rangle$ can be performed; these oscillations can be exploited use the KPO as a qubit. This procedure was presented and experimentallay applied by Grimm et al. in Ref. [12]

Quantum theory with dissipation

When dissipation is included, the equation of motion for the density matrix ρ of the system is the Lindblad master equation 1.41. Interestingly, even in the presence of dissipation, the subspace spanned by the displaced coherent states $|\alpha\rangle$ is still isolated from the remaining part of the Hilbert space. To see this, we consider the dissipator operator appearing in the Lindblad master's equation 1.41, which acts on the system density matrix ρ as

$$\rho \to \hat{b}\rho\hat{b}^{\dagger}. \tag{4.60}$$

The dissipator randmonly transforms the even cat state $\left|C^{+}(\alpha)\right\rangle$ in the odd cat state $\left|C^{-}(\alpha)\right\rangle$. For this reason, the dissipative dynamics of the master's equation 1.41 introduces quantum jumps between the even and odd cat states of the subspace spanned by $|\alpha\rangle$ and $|-\alpha\rangle$. These jumps suppress the quantum coherence of the system but preserve the system from leaking outside of the degenerate subspace. In its steady state, when $U \gg K$, the system is well described [13] by the classical mixture

$$\rho_{ss} = \frac{1}{2}\left(|\alpha\rangle\langle\alpha| + |-\alpha\rangle\langle-\alpha|\right). \tag{4.61}$$

This qualitative explanation is motivated by numerically evaluating the Von Neumann entropy $\mathcal{S}(\rho_{\text{ss}})$ of the steady-state density matrix ρ_{ss} obtained from numerical simulations, as shown in the following section.

4.3.4 Numerical approach to steady state

For the numerical simulations, we choose $\gamma = 136$ MHz, which is similar to the measured value for the JPA. We express K and U as multiples of γ for simplicity. The steady-state solution was examined for $K/\gamma = \left[0.1, 0.5, 1\right]$ and for U ranging from 0 to $U_{\max} = \gamma/2 = 2U_c$. The maximum value for U was chosen to keep the cutoff dimension of the Hilbert space to $D_c = 50$. The chosen values for K allow us to understand the physics of the system going from a weak-non linearity regime, in which $K \ll \gamma$, to a regime, were the effects of the non-linearity cannot be accounted for by using perturbative solutions, $K \approx \gamma$. In our numerical experiment, we focused on the following quantities:

1. Average photon population $\bar{n} = \langle \hat{b}^\dagger \hat{b} \rangle$.

2. Squeezing level for the quadrature $\hat{q}(\theta)$ for $\theta = \pi/4$, defined compared to the vacuum,

$$S(\theta) = 10 \log_{10} \left(2\mathrm{var}(\hat{q}(\theta)) \right) . \tag{4.62}$$

3. Second-order correlation function $g^{(2)}$.

We start by discussing the results for the average number of photons $\langle \hat{b}^\dagger \hat{b} \rangle$. As can be seen from Figure 4.16, the photon number increases monotonically as function of U for all the considered values of K. As K increases, $\langle \hat{b}^\dagger \hat{b} \rangle$ decreases. In the right-panel of Figure 4.16, we plot the derivative of $\langle \hat{b}^\dagger \hat{b} \rangle$ with respect to U. This quantity is always continuous and does not show the divergence for $U \to U_c$ predicted by the mean-field theory.

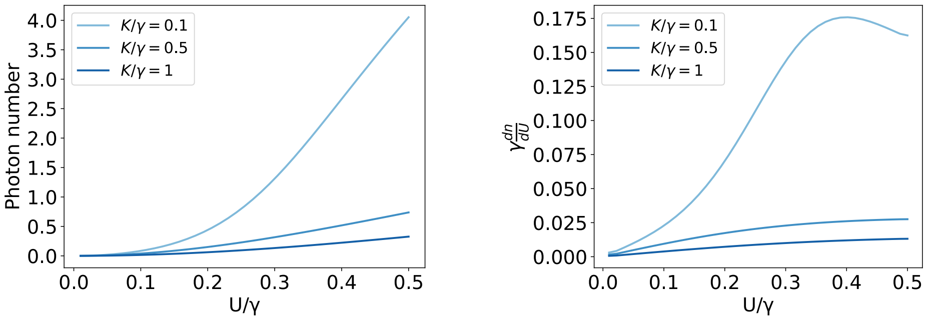

(a) **(b)**

Figure 4.16: Photon number, Figure (a), and derivative of the photon number with respect to the pump power, Figure (b), as function of the pump power U.

Next, we discuss the results of the second order correlation function $g^{(2)}$ and the squeezing level $S(3\pi/4)$, which are both plotted in Fig. 4.17. The second-order correlation function goes to $g^{(2)} \to \infty$ for decreasing values of the pump power, when $U < U_c$. This behavior is expected from squeezed vacuum states [31]. When $U > U_c$, the second-order correlation function quickly saturates to one. This observation is in agreement with the hypothesis that the steady-state solution in the high pump limit is well approximated by a classical mixture of displaced coherent states. For increasing values of K, we observe also that the squeezing along the $\theta = \pi/4$ quadrature deviates from the linear prediction. In particular, for $K/\gamma \simeq 1$, the intracavity squeezing reduces almost to zero.

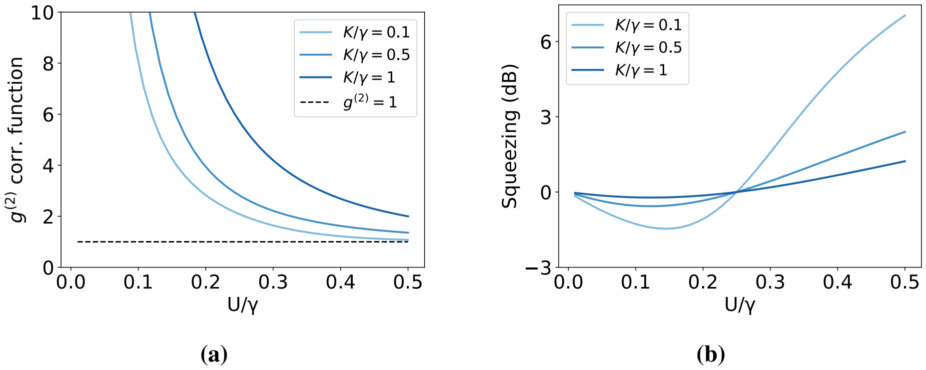

Figure 4.17: Second order correlation function $g^{(2)}$, Figure (a), and squeezing level with respect to the vacuum, Figure (b),for the quadrature $\hat{q}(\pi/4)$ as a function of U.

4.3.5 Wigner functions

To analyze graphically the behavior of the system, we show the Wigner functions associated to the steady state solutions, obtained for different values of U and K, Fig. 4.18. We observe that, for increasing values of the pump strength U, the steady state Wigner function of the quantum starts to split in the phase-space, along the $\theta = \pi/4$ quadrature, approaching the mixed state solution 4.61. Moreover, the steady-state Wigner function of the KPO are always positive.

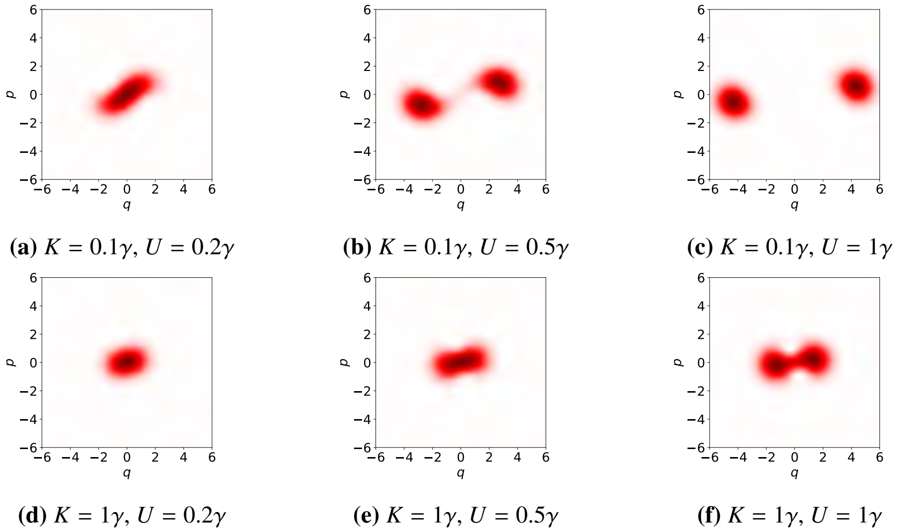

(a) $K = 0.1\gamma$, $U = 0.2\gamma$ **(b)** $K = 0.1\gamma$, $U = 0.5\gamma$ **(c)** $K = 0.1\gamma$, $U = 1\gamma$

(d) $K = 1\gamma$, $U = 0.2\gamma$ **(e)** $K = 1\gamma$, $U = 0.5\gamma$ **(f)** $K = 1\gamma$, $U = 1\gamma$

Figure 4.18: Wigner functions of the steady-state of teh Kerr Parametric Oscillator for different values of K and U, expressed here as fractions of γ. All the Wigner functions are normalized to their maximum value.

In figure 4.19, we show the marginal distributions of the computed density matrices for the axes $\theta = 3/4\pi$. The marginals are shown for different values od U and K. From the marginal distribution, the transition to a double-peak steady-state solution is clear.

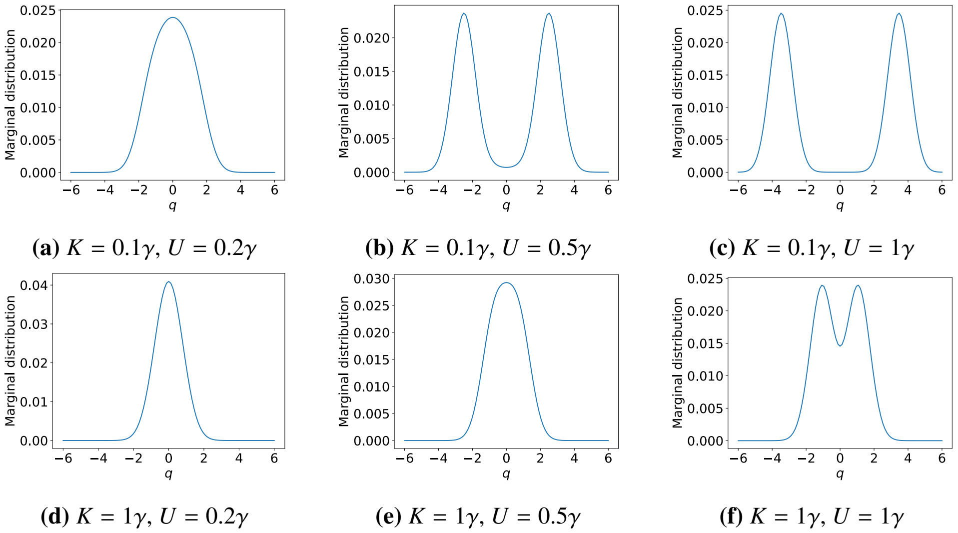

(a) $K = 0.1\gamma$, $U = 0.2\gamma$ **(b)** $K = 0.1\gamma$, $U = 0.5\gamma$ **(c)** $K = 0.1\gamma$, $U = 1\gamma$

(d) $K = 1\gamma$, $U = 0.2\gamma$ **(e)** $K = 1\gamma$, $U = 0.5\gamma$ **(f)** $K = 1\gamma$, $U = 1\gamma$

Figure 4.19: Marginal distributions along the axis $\theta = 3/4\pi$ of the Wigner function for the steady-state of teh Kerr Parametric Oscillator for different values of K and U, expressed here as fractions of γ. All the Wigner functions are normalized to their maximum value.

In Figure 4.20, we show the fidelity to the solution in Eq. 4.61 and the purity of the steady-state density matrix ρ evaluated numerically. As expected, the fidelity to the mixed state solution 4.61 approaches the unit value for high values of the pump strength. For increasing values of the Kerr non-linearity K, the fidelity to the solution 4.61 converges to one faster. In a similar way, the purity of the quantum state is a monotonically decreasing function of the pump strength U.

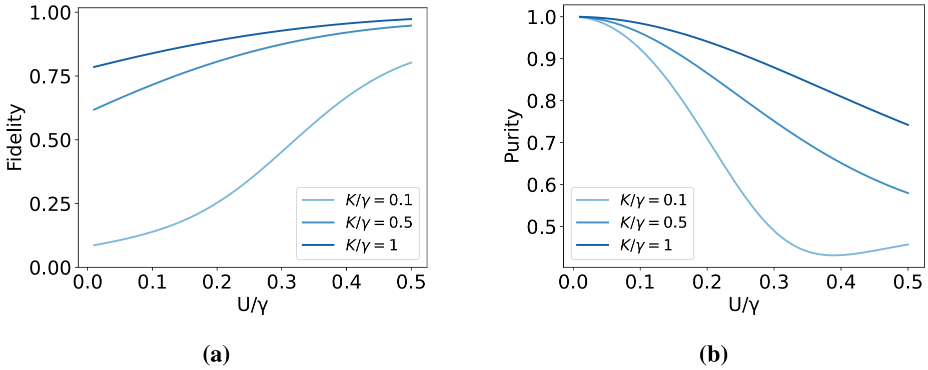

(a) **(b)**

Figure 4.20: Fidelity to the mixture of coherent states defined in equation 4.61, Figure (a), and purity of the steady-state density matrix, Figure (b), as a function of U.

To conclude our analysis we also show the Von Neumann entropy of the steady-state density

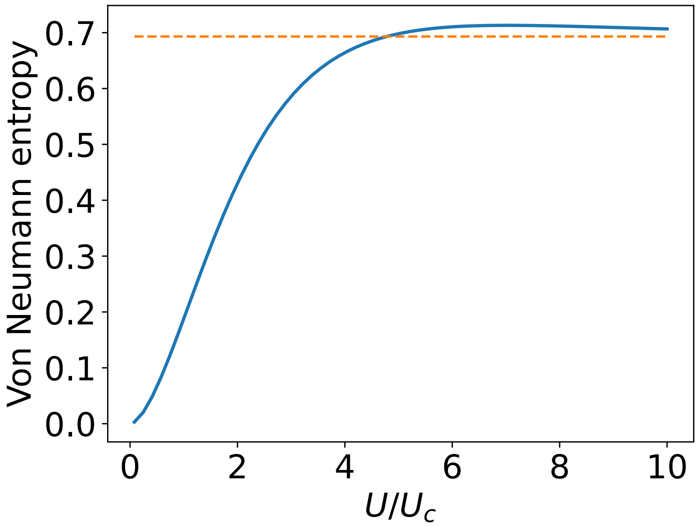

Figure 4.21: Von Neumann entropy of the steady state solution of the KPO, for $K = 2\gamma$, plotted as a function of the pump strength U.

matrix $\mathcal{S}(\rho_{\rm ss})$, which is defined as

$$\mathcal{S}(\rho_{\rm ss}) = -\mathrm{Tr}\left(\rho_{\rm ss}\log\rho_{\rm ss}\right) = -\sum_{n=1}^{D_c}\rho_{\rm ss}^{(n,n)}\log\rho_{\rm ss}^{(n,n)}. \tag{4.63}$$

The Von Neumann entropy $\mathcal{S}(\rho)$ is compared with the entropy $\mathcal{S}_{\rm mix}$ of a classical mixture REF, which, in the limit of large $\alpha, |\alpha| \gg 1$, reads as

$$\mathcal{S}_{\rm mix} = \log 2 \simeq 0.69. \tag{4.64}$$

As expected, for large values of the pump strenght U, the Von Neumann entropy $\mathcal{S}(\rho_{\rm ss}) \to \mathcal{S}_{\rm mix}$, as shown in Fig. 4.21. This observation confirms our phenomenological intuition: the steady-state of the KPO, in the high pump strength limit, does not describe a quantum superposition but rather a classical mixture of two coherent displaced states.

4.4 Conclusion

In this chapter, we discussed the quantum theory and the relevant physics of the superconducting quantum devices measured during this thesis work. In the first section, we introduced a lumped-element model to describe the superconducting quantum devices used in our experiments. In the second section, we described the quantum theory of the model describing the measurements performed using the JPC: the resonantly driven non-linear quantum oscillator. In the third and last section, we analyze the model describing the experiments performed using the JPA, the Kerr Parametric Oscillator (KPO).

Chapter 5

Experimental results

This chapter is dedicated to the discussion of the experimental results obtained during our thesis work; it is divided into two sections: the first section, 5.1, shows the analysis performed on the JPC experimental data. The second section, 5.2, deals with the experimental results of the JPA measurements. In both sections, we use the same notation as in Chapter 2 to label the quantum fields of the propagating radiation: we use $\hat{a}$ to label the quantum field before the amplification chain and $\hat{\xi}$ for the amplified field measured by the FPGA.

5.1 Results of JPC measurements

In this section, we summarize the experimental results obtained by analyzing the propagating quantum microwaves emitted by the JPC: the device is operated as explained in the first section of Chapter 4. First, in 5.1.1, we explain how the experimental histograms of the (I,Q) points are collected and how their histograms are averaged. We also mention how to compute the statistical uncertainties on the expectation values which, can be evaluated using the measured histogram. In the second one, 5.1.2, we analyze the deviation of the measured histogram from a Gaussian behavior, which is evidence of the non-linear nature of the JPC. In the third subsection, 5.1.3, we use the measured histogram to compute several expectation values of the propagating field emitted by the JPC; these expectation values are used as a benchmark for the results provided by tomographic techniques implemented in the following steps of our analysis. In the last subsection, 5.1.4, we perform the tomography of the radiation emitted by the JPC for a particular value of the signal power. Here, we combine the Lucy-Richardson deconvolution algorithm with the iterative maximum-likelihood estimation (IMLE) described in Chapter 2.

5.1.1 Meausuring the quantum field histograms

The emitted radiation of the JPC is analyzed for nine different values of the power of the input drive, ranging from -105 dBm to -80 dBm (estimated at the device). For each value of the input drive power, we measure $N_{tr} = 100$ traces consisting of $2^{14} = 16.384$ pairs of (I,Q) points. Given the IF frequency $f_{IF} = 12.5$ MHz of the demodulated signal, each trace lasts 1.3 ms. The JPC is operated with its coil current set at $I_{\text{coil}} = 0\ \mu A$. The resonance frequency of the device is $f_0 = 5.0927$ GHz at the measured working point.

Before averaging the measured histograms, we make sure that all the histograms, i.e. all the measured traces, encode the same physical information about the propagating microwave field emitted by the JPC in its *steady-state*. This is of fundamental importance since, in our experiments, we are measuring propagating quantum microwaves emitted in the *steady-state* of the JPC; the basic assumption in our measurements is that each (I,Q)-point is a random sampling from a fixed but unknown probability distribution. For this reason, we don't expect any correlation between the values of two consecutive points.

To check these requirements, we first measure the emitted average power for all the traces and for all the chosen values of the input field power. The results are shown in Figure 5.1, where we plot the relative measured power as a function of the number of traces for different values of the input power P_{in}. The relative power is defined as

$$P_{\text{rel}} = \log_{10}\left(\frac{P_{\text{measured}}(P_{\text{in}})}{P^0_{\text{measured}}}\right), \tag{5.1}$$

where $P_{\text{measured}}(P_{\text{in}})$ is the measured power for the input power P_{in} and P^0_{measured} is the measured power for the lowest value of the input power $P_{\text{in}} = -35$ dB, measured at the source (-105 dB estimated at the device). As expected, the average emitted power is constant for all traces for fixed values of the input field power.

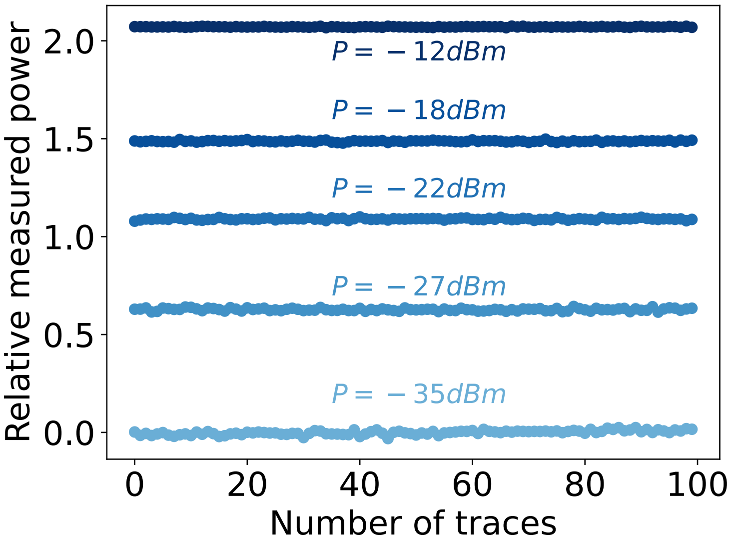

Figure 5.1: Measured relative powers at the FPGA plotted as a function of the trace number for different values of the input probe power at the JPC.

The second preliminary measurement deals with the phase ϕ of the measured (I,Q)-points, defined as

$$\phi = \arctan\left(\frac{Q}{I}\right). \tag{5.2}$$

When measuring this quantity, we observe a linear background imposed to its fluctuations around the mean value. We observe that:

1. the linear background covers the whole duration of the trace, which is on the order of 1 ms. For a cavity with decay rate $\gamma \approx 1$ MHz this time scale is several orders of magnitude longer than the average time correlation length $\tau \simeq 1/\gamma \approx 1\ \mu s$;
2. the slope of the linear background, measured in radians per millisecond is constant within the errors for different input drive powers, as shown in Figure 5.2. The average value for the slope is 0.22 rad/ms, for the input powers in the range between -95 dBm and -82 dBm.
3. The shift in the phase of the emitted signal most likely does not originate from a shift of the resonance frequency of the JPC. We motivate this statement by noting that the emitted power reflected by the JPC does not decrease over the measurement time, as shown Figure 1.1, which proves that the signal and the JPC are always in resonance. Since the frequency of the input signal is fixed, we state that the JPC frequency is also fixed.

In light of these observations, we conclude that the linear background is not a physical feature of the signal emitted by the JPC, therefore we treat it as an experimental artifact. We remove it by fitting the linear background in time and subctracting the fitted value from the phase fluctuations.

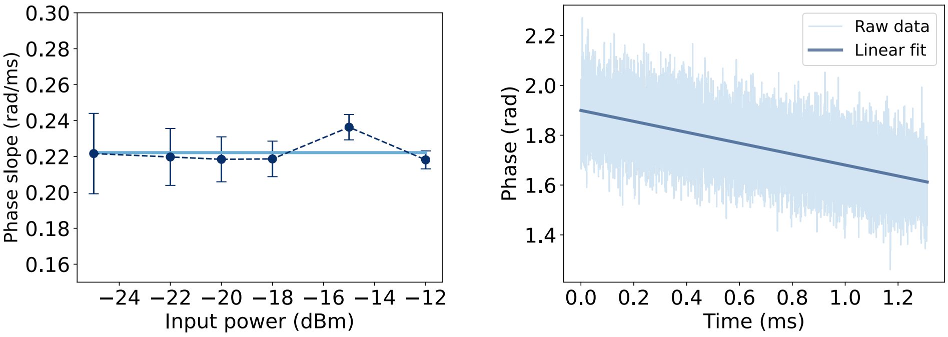

(a) **(b)**

Figure 5.2: Panel (a) shows the estimated slope of the linear phase background measured for different values of the input power P_{in}. The dark-blue marks represent the estimated values for the slope, the light-blue line indicates the average value for different values of the input power P_{in}. Panel (b) shows the phase of the sampled (I,Q)-points as a function of time (light-blue line) and linear fit of the background (dark-blue line), for $P_{in} = -88$ dBm.

To do so, for each trace of (I, Q)-points we define the complex numbers $z = I + \mathrm{j}Q$ and rotate them using

$$z \longrightarrow z' = e^{\mathrm{j}\phi_{\text{fitted}}} z, \tag{5.3}$$

where ϕ_{fitted} is the fitted linear background. From the rotated complex numbers z', we extract the rotated components $I' = \mathrm{Re}\{z'\}$ and $Q' = \mathrm{Im}\{z'\}$. The rotated components are binned in a two-dimensional histogram, obtained by discretizing each axis of the phase space with 100 points. The limits of the discretized axis are adapted to the power of the measured signal: we set the range of the axis to 1.5 times the value of the highest measured value for both quadratures. The discretized phase space is composed of 10,000 bins of the same area. The (I,Q) points are also rescaled by the square root of $\sqrt{G\kappa} = 1.84$ mV factor calibrated during the PNCF measurement in Chapter 3; the values collected in the histogram are therefore the rescaled quadratures

$$q_\xi = \frac{I}{\sqrt{G}}, \qquad p_\xi = \frac{Q}{\sqrt{G}} \tag{5.4}$$

of the amplified field $\hat{\xi}$. Each quadrature $\hat{q}_\xi$ and $\hat{p}_\xi$ has the units of squared number of photons. At the end of the whole process, for each k-th trace, with $k \in \{1, \ldots, N_{\mathrm{tr}}\}$, we obtain an histogram $H^{(k)}$ consisting of $2^{14} = 16.384$ points. From the $N_{\mathrm{tr}} = 100$ noisy histograms $H^{(k)}$, we obtain a single histogram H by averaging them. In particular, the value of the averaged histogram H in the (i,j)-th phase-space point, $H\left[i, j\right]$, is estimated as the mean of $H^{(k)}_{i,j}$ for all $k \in \{1, \ldots, N_{tr}\}$,

$$H_{i,j} = \frac{1}{N_{tr}} \sum_{k=1}^{N_{tr}} H^{(k)}_{i,j}. \tag{5.5}$$

In the last equation, the value $H\left[i,j\right]$ measures the average frequency outcome associated to (i, j)th-bin of the discretized phase-space. Moreover, in order to use the sampled histogram as an approximation of the continuous Husimi Q-function Q_ξ of the mode $\hat{\xi}$, we rescale each value $H\left[i,j\right]$ by the square of the phase-space resolution Δq^2. By doing this, we automatically impose the normalization condition

$$\iint_{\mathbb{C}} d^2z\, H(z) \simeq \Delta q^2 \sum_{i,j} H\left[i,j\right] = 1. \tag{5.6}$$

The statistical errors on $H_{i,j}$, $\delta H_{i,j}$, are estimated as the standard deviation on the mean,

$$\delta H_{i,j} = \frac{1}{\sqrt{N_{\mathrm{tr}}}} \sqrt{\mathrm{var}(H_{i,j})}, \tag{5.7}$$

and are grouped in an histogram δH.

Estimation of statistical errors

In the continuous case, the most general integral quantity that can be estimated using the histogram H is of the type

$$F = \iint_{\mathbb{C}} d^2z\, H(z) f(z), \tag{5.8}$$

where $f(z)$ is a generic integrable function on the phase-space. In our case, we deal with discretized functions and , therefore, we approximate the two-dimensional integral as

$$F \approx (\Delta q)^2 \sum_{i,j} H_{i,j} f_{i,j}, \tag{5.9}$$

where Δq is the quadrature resolution of the discretized axis. The statistical error on F, labeled as δF, can be computed from the histogram of the statical errors δH using standard error-propation techniques. Indeed, we estimate

$$\delta F = \sqrt{\sum_{ij}\left[\frac{\partial F}{\partial H_{i,j}}\delta H_{i,j}\right]^2} = \sqrt{\sum_{ij}\left[f_{i,j}\,\delta H_{i,j}\right]^2}. \tag{5.10}$$

Therefore, for any observable $f(z)$ in the phase space, we estimate the mean value F and the statical error δF with Eqs. 5.8 and 5.10.

5.1.2 Measured histograms and cross-sections

In this section, we show the measured histograms of the rescaled quadratures (q_ξ, p_ξ), obtained for different values of the power of the resonant drive to the JPC. Remarkably, non-Gaussian features of the propagating quantum radiation are clearly seen in the histogram for the amplified field mode $\hat{\xi}$. As explained in Chapter 4, the non-Gaussianity of the emitted field is an indicator of the non-linearity characterizing the JPC.

As a first analysis, we characterize the non-Gaussianity on a qualitative and quantitative level: first, by looking at the cross-sections of the measured two-dimensional histogram and, second, by measuring the functional distance between each histogram and its best Gaussian approximation.

In Fig. 5.3, we show the histogram H and the histogram of the statistical measurements errors for the measured mode $\hat{\xi}$, emitted by the JPC with a resonant input drive of strength -100 dBm. From the plot on the left, it is possible to observe a typical "bean" shape of the *steady-state* emission from a driven non-linear quantum oscillator, as described in Chapter 4. The statistical error is in the order of 2% of the measured value. In Fig. 5.4, we show the cross-sections of the

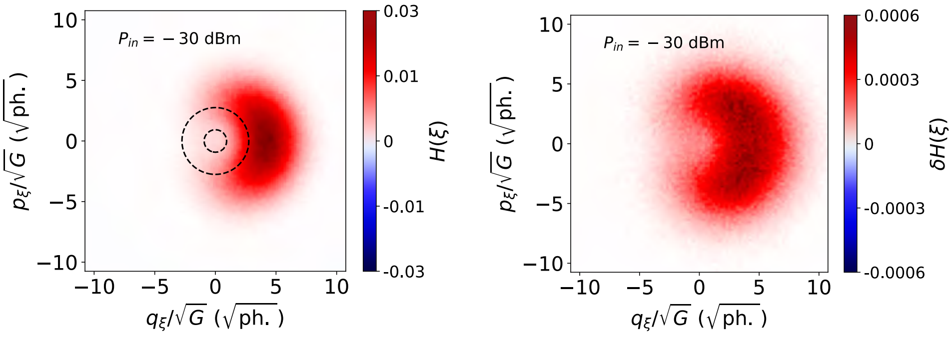

(a) **(b)**

Figure 5.3: Histogram H (Figure a) and error histogram δH (Figure b) measured for the mode $\hat{\xi}$. The mode corresponds to the amplified signal emitted by the JPC, when the power of the resonant input signal is $P_{in} = -30$ dBm at the source. The values binned in both histograms are rescaled by the PNCF coefficient $\sqrt{Gk} = 1.84$ mV measured in Chapter 3. The dashed black lines in figure (a) refers to the reference state measured without driving the JPC. The input power at the device can be obtained considering the $70dB$ attenuation on the input line.

measured histogram for different positions in the phase-space $\mathbb{C}$. On the left side, we show the cross-section of the measured histogram obtained at $p_\xi/\sqrt{G} = 0$. This cross-section slightly distorted Gaussian peak, displaced from the origin of the phase-space. On the right side, we show the cross-sections obtained at $q_\xi/\sqrt{G} = -0.87$ and $q_\xi/\sqrt{G} = 0.43$. These cross-sections show a clear double-peak structure.

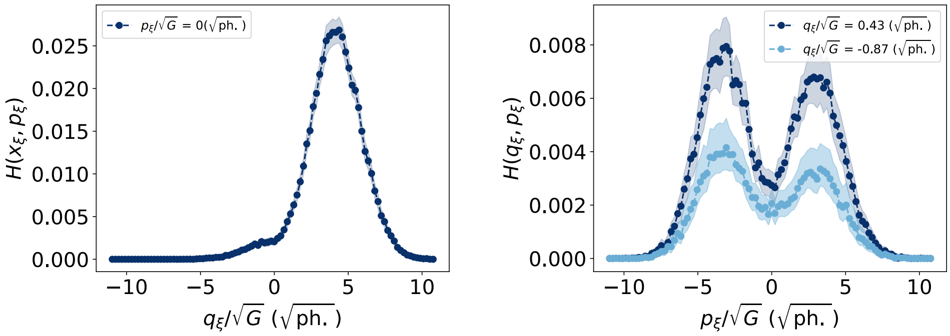

(a) **(b)**

Figure 5.4: Cross-sections of the measured histogram for different "cuts" in the phase-space $\mathbb{C}$ for $P_{in} = -100$ dBm (-30 dBm at the source). In both plots, the shaded region describes the statistical error, assumed to be three times the standard deviation of the estimated average value.

The same plots are shown for $P_{in} = -22dBm$. In particular, the histogram of the measured values and the histogram of the standard deviations are shown in Figure 5.5. Also, in this case, we observe that the histogram has the shape of a distorted displaced gaussian state.

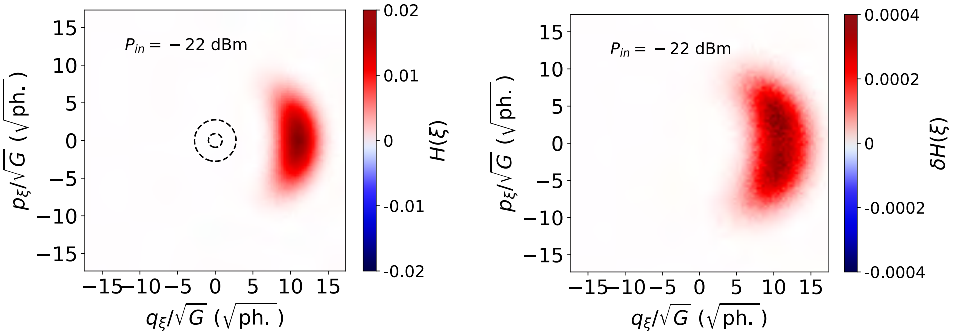

(a) **(b)**

Figure 5.5: Histogram H (Figure a) and error histogram δH (Figure b) measured for the mode $\hat{\xi}$. The mode corresponds to the amplified signal emitted by the JPC when the power of the resonant input signal is $P_{in} = -22$ dBm at the source. The dashed black line in figure (a) refers to the reference state measured without driving the JPC. The input power at the device can be obtained considering the $70dB$ attenuation on the input line.

The phase-space cross-section of the histograms collected for $P_{in} = -92$ dBm are shown in Figure 5.6.

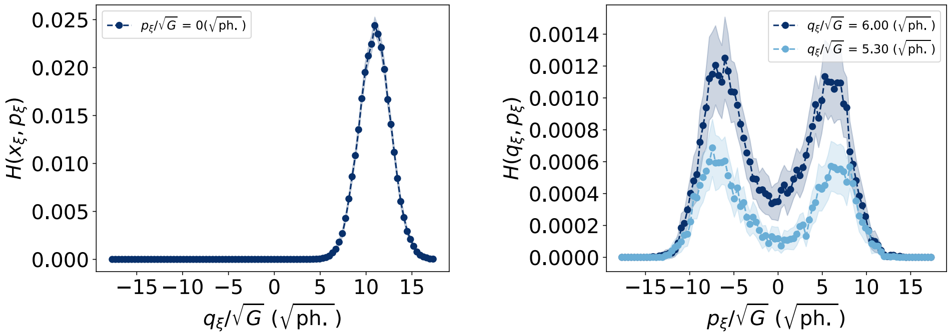

(a) **(b)**

Figure 5.6: Cross-sections of the measured histogram for different positions in the phase-space $\mathbb{C}$ for $P_{in} = -92$ dBm at the device (−22 dBm at the source). In both plots, the shaded region describes the statistical error, assumed to be three times the standard deviation of the estimated average value.

To quantify more precisely the deviation of the observed field mode $\hat{\xi}$ from a Gaussian state, we fit each of the two-dimensional histograms, collected for the different values of the signal power, to a two-dimensional Gaussian distribution. This two-dimensional Gaussian is chosen to be symmetric in both quadratures, as expected from the displaced field in a perfect linear cavity. Therefore, this model distribution, for a generic point z in the phase space $\mathbb{C}$, reads as

$$\mathcal{G}(z; z_c, \sigma, A) = A \cdot e^{-|z-z_c|^2/\sigma^2}, \tag{5.11}$$

where z_c is the complex displacement amplitude of the Gaussian, σ is the standard deviation of the Gaussian and A is a normalization constant. Physically, since we allow the standard deviation of the Gaussian model to vary, we fit the measured histograms against displaced thermal fields. For each measured histogram H, we numerically fit the most likely Gaussian $\mathcal{G}_H$ defined in Eq. 5.11. To evaluate the difference between the two distributions, we use the L^1 [82] functional difference $\mathcal{D}(H, \mathcal{G}_H)$, defined as

$$\mathcal{D}(H, \mathcal{G}_H) = \iint d^2\xi \left| H(\xi) - \mathcal{G}_H(\xi) \right| . \tag{5.12}$$

The results of the fit are shown in Fig. 5.7 for the input power $P_{\text{in}} = -100$ dBm and $P_{\text{in}} = -92$ dBm.

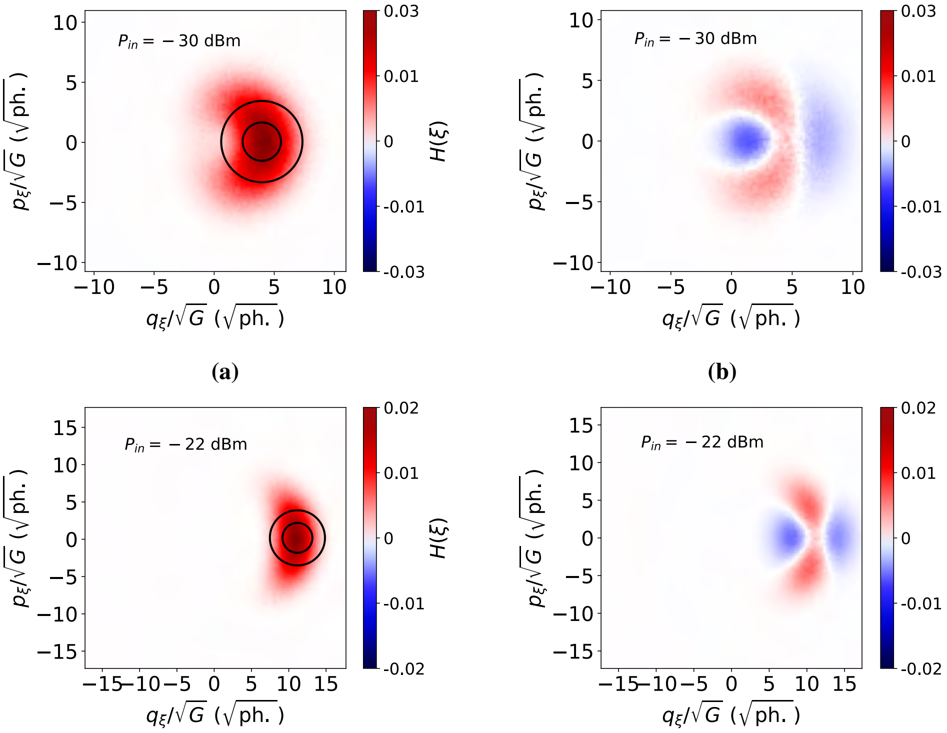

(a) **(b)**

(c) **(d)**

Figure 5.7: Figures (a) and (c), average histograms H and contour lines (black solid line) of the best-fit Gaussian function $\mathcal{G}_H$ for $P_{in} = -30$ dBm and $P_{in} = -22$ dBm at the source respectively. Figures (b) and (d), the difference between the average histogram H and the best fit gaussian $\mathcal{G}_H$ for $P_{in} = -30$ dBm and $P_{in} = -22$ dBm at the source respectively. To obtain the value of the input power estimated at the device we have to consider the 70 dB attenuation on the input line.

In Fig. 5.8, we plot $\mathcal{D}(H, \mathcal{G}_H)$ as a function of the signal power. We also show the absolute value of the fitted complex displacement amplitude z_c as a function of the power of the input signal to the JPC.

5.1.3 Expectation values

In this section, we continue our analysis of the histograms collected from the *steady-state* emission of the JPC. In particular, we compute several expectation values which are useful in order to characterize the features of the propagating quantum radiation. The expectation values of interest are:

1. the average photon number $\langle \hat{a}^\dagger \hat{a} \rangle$ of the field mode $\hat{a}$, which describes the propagating microwave before being amplified by the amplification chain;
2. the second-order correlation function $g^{(2)}$ of the field mode $\hat{a}$;
3. the absolute value of the complex displacement amplitude $\alpha = |\langle \hat{a} \rangle|$, which quantifies the displacement of the field mode $\hat{a}$ in the phase space;

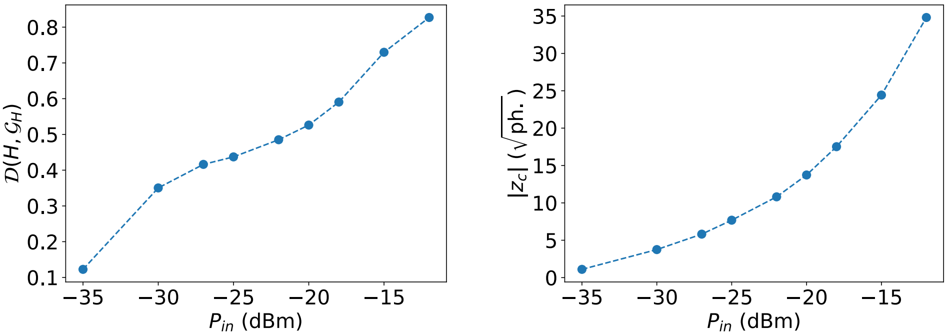

(a) **(b)**

Figure 5.8: The L^1 functional difference between the measured histogram H and the fitted gaussian $\mathcal{G}_H$, Figure (a), and the absolute value of the fitted complex displacement amplitude z_c, Figure (b), as a function of the power of the resonant drive signal to the JPC. Here the power is referred at the source. To obtain the value of the input power estimated at the device we have to consider the 70 dB attenuation on the input line.

4. the absolute value of the expectation value of the squared field mode $\hat{a}^2$, $|\langle \hat{a}^2 \rangle|$. This value will be used in the following sections to benchmark the results of the maximum-likelihood estimation protocol.

All the above-mentioned expectation values can be efficiently computed using the histogram of the amplified mode $\hat{\xi}$. In the next subsection, we discuss on how to practically compute these expectation values.

Calculation of expectation values from measured histograms

For each value of the power of the input signal to the JPC, the collected histograms approximate the Husimi Q-function of the amplified mode $\hat{\xi}$, Q_ξ. As explained in Chapter 1, Q-functions only allow to compute expectation values of anti-normal ordered products of field mode operator. In particular, for a general anti-normal product $\hat{\xi}^n \hat{\xi}^{\dagger^m}$, with n and m integers, we have

$$\langle \hat{\xi}^n \hat{\xi}^{\dagger^m} \rangle = \iint_{\mathbb{C}} d^2\xi \, Q_\xi(\xi) \xi^n \xi^{*^m}, \tag{5.13}$$

where Q_ξ is the Husimi Q-function describing the mode $\hat{\xi}$. Moreover, in order to compute the expectation values of the field mode $\hat{a}$, we use the approximated Caves relation

$$\frac{\hat{\xi}}{\sqrt{G}} = \hat{a} + \hat{v}^\dagger, \tag{5.14}$$

derived in Chapter 2. In the last equation, G is the linear amplification gain provided by the amplification chain and $\hat{v}$ is the thermal field with occupation number n_v, describing the noise introduced by the amplification process. In the following paragraphs, we provide the equations to compute the expectation values of the mode $\hat{a}$ using the Husimi Q-function of the mode $\hat{\xi}$, the Caves relation 5.14 and the average photon population n_v of the mode $\hat{v}$.

Absolute values $|\langle \hat{a} \rangle|$ and $|\langle \hat{a}^2 \rangle|$ We start from the absolute values $|\langle \hat{a} \rangle|$ and $|\langle \hat{a}^2 \rangle|$. Using the Caves relation 5.14 and Eq. 5.13, we can readily evaluate

$$|\langle \hat{a} \rangle| = \frac{1}{G} \left| \iint\limits_{\mathbb{C}} Q(\xi)\xi \, d^2\xi \right| , \tag{5.15}$$

where we neglect the expectation value $\langle \hat{v} \rangle$ since the noise field mode $\hat{v}$ describes non-displaced vacuum fluctuations and therefore $\langle \hat{v} \rangle = 0$. Experimentally, the measured histogram $H(\xi)$ approximates the Husimi Q-function and we can write

$$|\langle \hat{a} \rangle| \approx \frac{1}{G} \left| \iint\limits_{\mathbb{C}} H(\xi)\xi \, d^2\xi \right| . \tag{5.16}$$

In the same way,

$$|\langle \hat{a}^2 \rangle| = \frac{1}{G} \left| \iint\limits_{\mathbb{C}} H(\xi)\xi^2 \, d^2\xi \right| . \tag{5.17}$$

Average photon population $\langle \hat{a}^\dagger \hat{a} \rangle$ For the average photon population $\langle \hat{a}^\dagger \hat{a} \rangle$, we use the canonical commutation relation

$$\left[\hat{a}, \hat{a}^\dagger\right] = \mathbb{I}, \tag{5.18}$$

where $\mathbb{I}$ is the identity operator, and we rewrite the expectation value as

$$\langle \hat{a}^\dagger \hat{a} \rangle = \langle \hat{a}\hat{a}^\dagger \rangle - 1. \tag{5.19}$$

From Eq. 5.14, we derive that

$$\langle \hat{a}\hat{a}^\dagger \rangle = \frac{\langle \hat{\xi}\hat{\xi}^\dagger \rangle}{G} - n_v. \tag{5.20}$$

In the above equation we omit the terms $\langle \hat{a}\hat{v}^\dagger \rangle$ and $\langle \hat{a}^\dagger \hat{v} \rangle$; the reason is that these expectation values can be factorized as $\langle \hat{a} \rangle \langle \hat{v}^\dagger \rangle$ and $\langle \hat{a}^\dagger \rangle \langle \hat{v} \rangle$, respectively, since we assume that the statistics of the noise field $\hat{v}$ does not depend on the state being amplified. Using Eq. 5.13 we obtain,

$$\langle \hat{a}^\dagger \hat{a} \rangle = \frac{1}{G} \iint\limits_{\mathbb{C}} d^2\xi \, H(\xi)|\xi|^2 - n_v - 1. \tag{5.21}$$

The term (-1) in the last equation is physically relevant since it accounts for the non-commutative nature of bosonic operators.

Second order correlation function $g^{(2)}$ The second-order correlation function $g^{(2)}$ is defined as

$$g^{(2)} = \frac{\langle \hat{a}^{\dagger 2} \hat{a}^2 \rangle}{\left(\langle \hat{a}^\dagger \hat{a} \rangle\right)^2}. \tag{5.22}$$

The denominator of this expression can be computed using the Eq. 5.21. For the numerator, we start by rewriting it as a linear combination of the anti-normal ordered product of the field operator $\hat{a}$. Using the canonical commutation relation between $\hat{a}$ and $\hat{a}^\dagger$, we obtain

$$\langle \hat{a}^{\dagger^2} \hat{a}^2 \rangle = \langle \hat{a}^2 \hat{a}^{\dagger^2} \rangle - 4\langle \hat{a}\hat{a}^\dagger \rangle + 2. \tag{5.23}$$

The second term in this expression can be computed using Eq. 5.20. For the first term, starting from the Caves relation 5.14, we obtain

$$\langle \hat{a}^2 \hat{a}^{\dagger^2} \rangle = \frac{1}{G}\langle \hat{\xi}^2 \hat{\xi}^{\dagger^2} \rangle - \langle \hat{v}^{\dagger^2} \hat{v}^2 \rangle - 4\langle \hat{v}^\dagger \hat{v} \rangle \langle \hat{a}\hat{a}^\dagger \rangle, \tag{5.24}$$

where the expectation value $\langle \hat{\xi}^2 \hat{\xi}^{\dagger^2} \rangle$ can be computed using Eq. 5.13 in the case of $n = m = 2$. The expectation values of the thermal noise field mode $\hat{v}$, $\langle \hat{v}^{\dagger^2} \hat{v}^2 \rangle$ and $\langle \hat{v}^\dagger \hat{v} \rangle$, can be computed using the relations [31],

$$\langle \hat{v}^{\dagger^2} \hat{v}^2 \rangle = 2n_v^2 \qquad \text{and} \qquad \langle \hat{v}^\dagger \hat{v} \rangle = n_v, \tag{5.25}$$

where n_v is calibrated in Chapter 3 using the PNCF measurement.

Results In this paragraph, we present the experimental results obtained by calculating the expectation values of the mode $\hat{a}$ as a function of the input signal power. The results are shown in Figure 5.9.

(a) Photon population $\langle \hat{a}^\dagger \hat{a} \rangle$. **(b)** Absolute value $|\hat{a}|$.

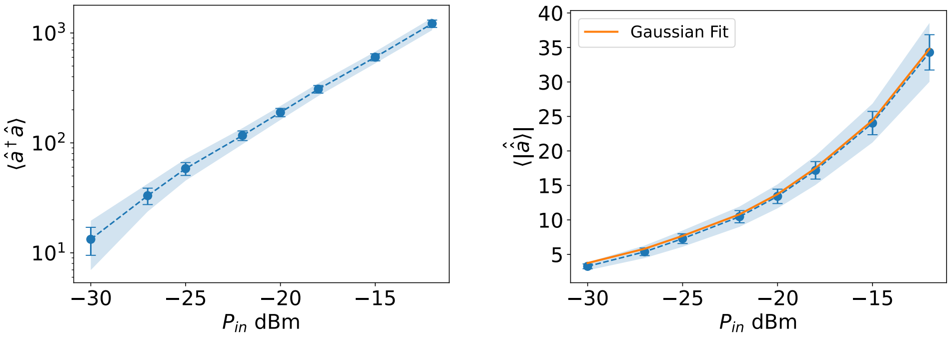

(c) Absolute value $|\hat{a}^2|$. **(d)** Correlation function $g^{(2)}$.

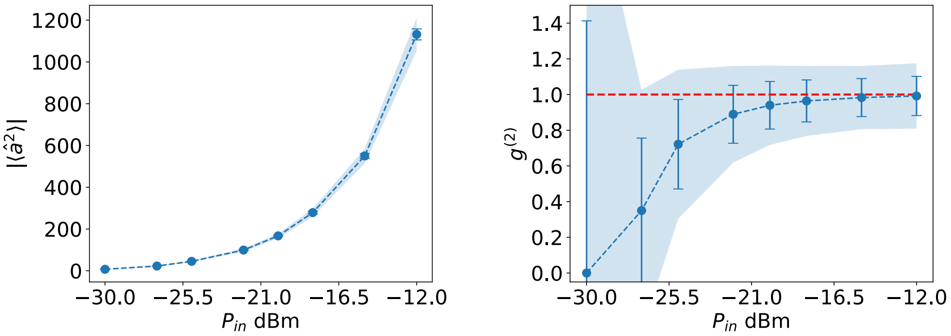

Figure 5.9: Expecatation values of the field mode $\hat{a}$ measured using the histogram of the measured mode $\hat{\xi}$. The expectation values are plotted as a function of the input power P_{in}. For all plots, the error bars correspond to three times the standard deviations (confidence interval of approximately 97%), while the shaded blue area corresponds to five times the standard deviation (confidence interval of 99%). In Figure (b), the orange solid line represents the absolute value of the displacement amplitude z_c from the Gaussian fit of the measured histogram. The powers on the x-axis are referred to the source. To obtain the value of the input power estimated at the device we have to consider the 70 dB attenuation on the input line.

We observe that the average photon population $\langle \hat{a}^\dagger \hat{a} \rangle$ increases exponentially as a function of the input power P_{in}: indeed, for $P_{\text{in}} \approx -95$ dBm, $\langle \hat{a}^\dagger \hat{a} \rangle \geq 60$ photons. The absolute value $\left|\langle \hat{a} \rangle\right|$ is shown together with the absolute value of the complex displacement amplitude $|z_c|$ for the mode $\hat{\xi}$, estimated in the previous section. The two curves show a good agreement, as expected. Indeed, from the Caves relation 5.14, we expect that

$$\langle \hat{a} \rangle = \frac{1}{G} \langle \hat{\xi} \rangle, \tag{5.26}$$

since the noise mode has zero average value, $\langle \hat{v} \rangle = 0$. This observation corroborates the physical consistency of the analysis performed so far.

For the considered expectation values, we observe that the size of the error bars increases with the power of the field mode $\hat{a}$. Indeed, while the errors of the second-order moments are small compared to their estimated value, this does not hold true for the the second-order correlation coefficient $g^{(2)}$, which calculation requires the calculation of fourth-order powers of the field mode $\hat{a}$, which shows a higher degree of statistical uncertainty. Despite that, we measure *anti-bunching* of the field emitted by the JPC, with a confidence interval of three standard deviations (97% confidence interval). This result suggests the quantum nature of the light emitted by the JPC.

5.1.4 Tomography of the JPC output field

In this section, we present the experimental results obtained by performing a complete quantum tomography for the JPC *steady-state* output mode $\hat{a}$. We divide the tomographic procedure into two steps: in the first step, we use a standard deconvolution technique, the Lucy-Richardson algorithm, to obtain the histogram of the mode $\hat{a}$ from the knowledge of the measured histogram $\hat{\xi}$ and the noise distribution $\hat{\nu}$. In the second step, we perform the iterative-maximum likelihood estimation (IMLE) to find the maximum-likelihood density matrix ρ_{MLE} from the estimated histogram of the mode $\hat{a}$. We use this two-step procedure instead of performing directly the IMLE protocol because, due to the preliminary noise deconvolution, we are able to reduce the numerical complexity of the overall procedure.

In particular, we apply the tomographic procedure to the histograms measured for input powers $P_{\mathrm{in}} = -100$ dBm $P_{\mathrm{in}} = -97$ dBm. For both values of P_{in}, we set the dimensional cut-off D_c of the density matrix ρ_{MLE} to respectively 120 and 160. The dimensional cut-offs are found empirically by running the IMLE protocol each time for different values of D_c. For higher values of P_{in}, the average photon population $\langle \hat{a}^\dagger \hat{a} \rangle$ increases above 100 photons, which would require a dimension cut-off $D_c \geq 200$. This estimation is obtained by assuming a linear dependence between D_c and the average photon population $\langle \hat{a}^\dagger \hat{a} \rangle$, as shown in Figure 5.10. Therefore, since the numerical complexity of the IMLE protocol scales as a power of D_c, as shown in Chapter 2, for input powers $P_{\mathrm{in}} \geq -95$ dBm, the protocol could not be run on the used hardware.

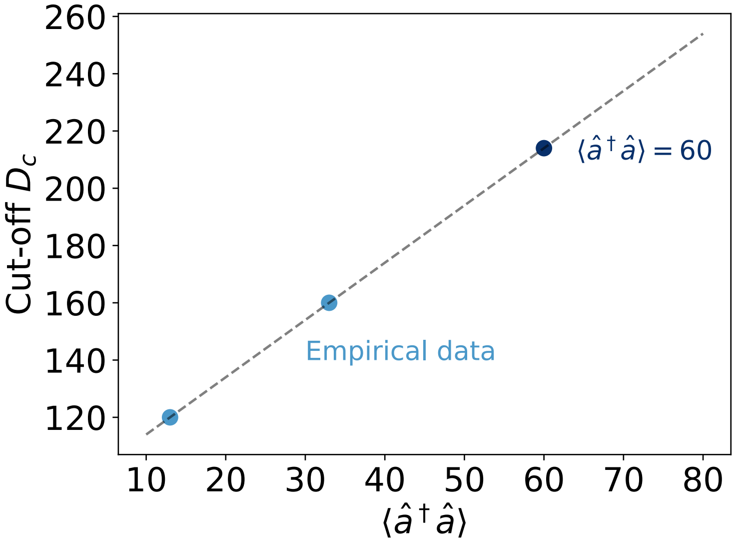

Figure 5.10: Linear regression, dashed grey line, of the minimum required cut-off dimension D_c as a function of the average photon population $\langle \hat{a}^\dagger \hat{a} \rangle$. The light-blue marks indicate the points found empirically. The dark-blue mark indicates the value of D_c estimated for $\langle \hat{a}^\dagger \hat{a} \rangle = 60$, which is greater than 200.

Deconvolution of measured histogram

The Lucy-Richardson deconvolution is an iterative procedure to reconstruct an image degraded from a known noise distribution. The algorithm was developed independently by W. Richardson [88] and L. Lucy [89]. Mathematically, given a general convolution

$$\zeta(z) = \iint d^2z' f(z) h(z - z') = f * h, \tag{5.27}$$

where h is the noise source, f is the original function and ζ is the degraded function, the Lucy-Richardson algorithm allows to estimate f iteratively using the Bayes theorem: at each iteration k of the algorithm, it returns an estimator $\tilde{f}_k$ of the function f. The algorithm stops when the maximum number of iterations, set by the user, is reached or when the difference between two consecutive estimations $\left|\tilde{f}_{k+1} - \tilde{f}_k\right|$ is smaller than a predefined numerical constant. In this work, we use the Lucy-Richardson algorithm to deconvolve the amplification noise mode $\hat{v}$ from the measured histogram of the mode $\hat{\xi}$, in order to obtain the Husimi Q-function of the mode $\hat{a}$. This is possible because of relation linking the Husimi Q-function of the measured histogram, Q_ξ, the Husimi Q-function of the mode $\hat{a}$, Q_a, and the Glauber-Sudarshan P-function of the noise P_v, reads as

$$Q_\xi(z) = \iint_{\mathbb{C}} d^2z'\, Q_a(z') P_v(z - z') = Q_a * P_v, \tag{5.28}$$

which is formally identical to the convolution in equation 5.27. The Lucy-Richardson deconvolution has already used by Boutin et al. in Ref. [90], in the context of microwave quantum optics to obtain the histogram of the quantum mode before the amplification chain.

Deconvolved Husimi Q-function In order to perform the noise deconvolution using the Lucy-Richardson algorithm, we utilize its implementation included in the open-source "scikit-image" [91] library for image processing developed using the Python programming language. To run the algorithm, we need to define three input parameters: the measured histogram for the mode $\hat{\xi}$, which plays the role of the degraded image, the P-function of the noise mode, calibrated using the PNCF measurement, and the number of iterations N_{iter} for the iterative procedure. The number of iterations is not set *a-priori*. In fact, we run the deconvolution protocol by sweeping the number of iterations N_{iter} from 1 to 20. For each value of the number of iterations N_{iter}, we estimate the average photon population $\langle \hat{a}^\dagger \hat{a} \rangle$ from the deconvoluted Q-function of the mode $\hat{a}$, Q_a, using

$$\langle \hat{a}^\dagger \hat{a} \rangle = \iint_{\mathbb{C}} d^2\alpha \, Q_a(\alpha) \left(|\alpha|^2 - 1 \right) . \tag{5.29}$$

The average photon population estimated from the last equation is compared to the one estimated with the measured histogram of the amplified mode $\hat{\xi}$ using Eq. 5.21. The results, for the case $P_{\text{in}} = -100$ dBm, are shown in Figure 5.11.

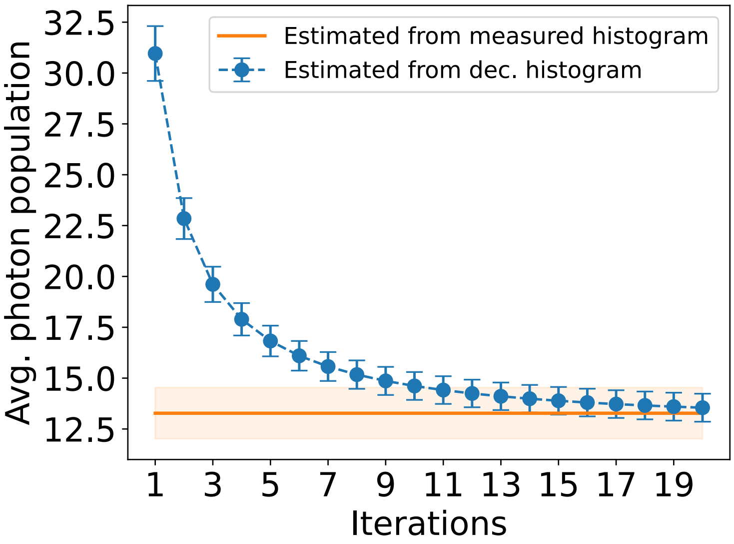

Figure 5.11: Average photon number estimated from the deconvolved histogram H_D of the mode $\hat{a}$ (blue marks) as a function of the number of iterations of the Lucy-Richardson algorithm applied to the measured histogram H. The orange solid line indicates the average photon number estimated from the measured histogram. The vertical errorbars indicate three times the standard deviation of the estimated average value. The value of the input power for the considered data is $P_{in} = -100$ dBm at the device.

As expected, the average photon population converges to its saturation value monotonically. We observe that when $N_{\text{iter}} = 20$, the average photon population estimated using the deconvoluted histogram Q_a, agrees within the error-bars with the one estimated using Eq. 5.21. So, in the following, we set $N_{\text{iter}} = 20$. In Figure 5.12, we show the color map of the deconvoled

Husimi Q-function for the mode $\hat{a}$ compared to the contour lines of the measured histogram for the mode $\hat{\xi}$. We clearly see how the Q-function for the mode $\hat{a}$ is narrower around its mean value, compared to the measured histogram, since we eliminate the fluctuations introduced by the noise mode $\hat{v}$.

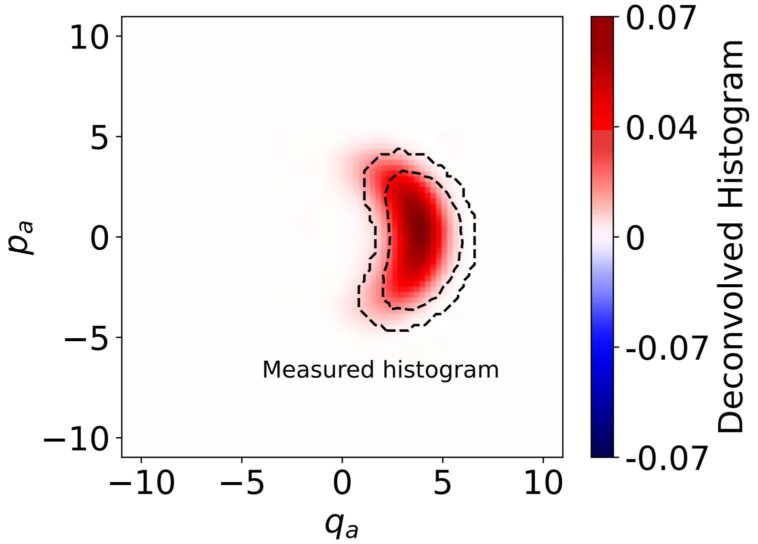

Figure 5.12: Deconvolved histogram H_D of the mode $\hat{a}$ obtained after 20 iterations of the Lucy-Richardson algorithm. The dashed black line indicates the contour lines of the measured histogram for the measured noisy mode $\hat{\xi}$.

Reconstruction of density matrix using IMLE

For this section, we only focus on the case $P_{\text{in}} = -100$ dBm; the results for the case $P_{\text{in}} = -97$ dBm are qualitatively similar.

The convoluted Q-functions obtained from the Lucy-Richardson algorithm is used as input parameters for the IMLE protocol introduced in Sec. 2.3. For the IMLE protocol, we set the number of maximum iterations to $N_{\max} = 30$ and the numerical tolerance factor to $\delta = 10^{-4}$. In Fig. 5.13, we plot the logarithmic likelihood $\log L[n]$ and the increment $\delta \log L[n]$ as a function of the iteration number $n \in \{1 \ldots, N_{\max}\}$, where the increment is defined as

$$\delta \log L[n] = \log L[n+1] - \log L[n] . \tag{5.30}$$

The logarithmic likelihood quickly increases as a function of n near its saturation value and the algorithm converges after $n \simeq 20$ iterations, when the increment $\delta \log L$ is smaller than the tolerance parameter $\delta = 10^{-4}$. Moreover, it is clear that the protocol converges exponentially fast, as a function of the iteration number, to the maximum-likelihood solution.

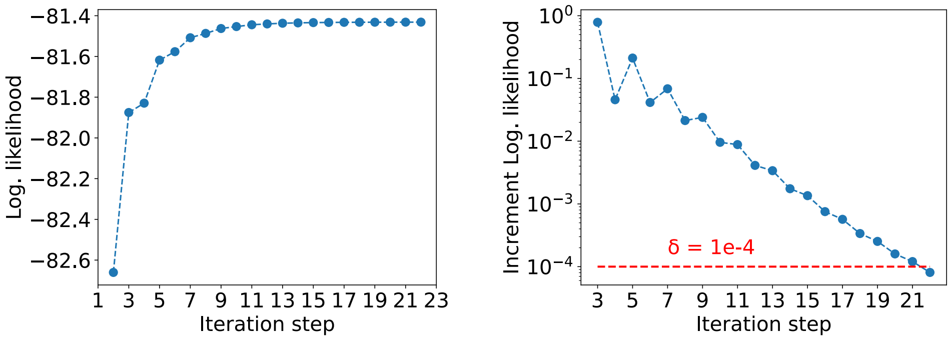

(a) **(b)**

Figure 5.13: Figure (a), logarithmic likelihood as function of the iteration step for the IMLE protocol. Figure (b), discrete differential logarithmic likelihood as function of the iteration step for the IMLE protocol .

The IMLE protocol outputs the maximum-likelihood density matrix ρ_{MLE} for the mode $\hat{a}$. The real and imaginary parts of the entries of the maximum-likelihood density matrix ρ_{MLE} are shown in Figure 5.14. For graphical purposes, we show only the first 35 rows and columns of the density matrix ρ_{MLE}. The reconstructed density matrix has an estimated purity of $\mathrm{Tr}\left(\rho_{\mathrm{MLE}}^2\right) = 0.15$, which is substantially higher to the theoretical lower bound for completely mixed states (see Ref. [55]) given by $1/D_c = 0.008$: this feature explains why some diagonal elements of the density matrix ρ_{MLE} are non-zero.

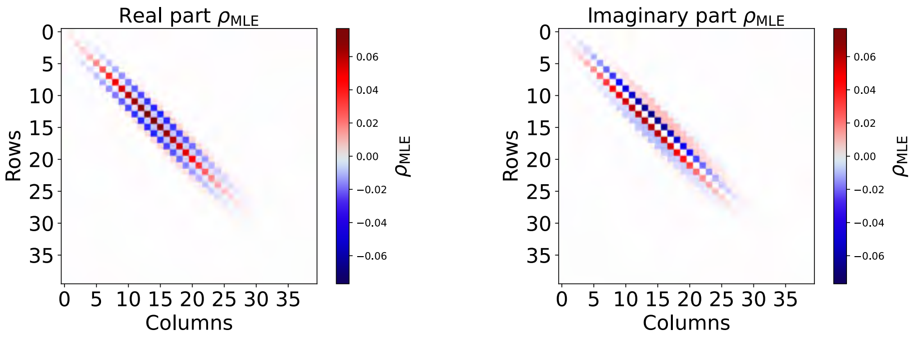

(a) **(b)**

Figure 5.14: Figure (a), real part of the entries of the maximum-likelihood density matrix ρ_{MLE}. Figure (b), imaginary part of the entries of the of the maximum-likelihood density matrix ρ_{MLE}.

In Figure 5.15, we plot the diagonal elements of the reconstructed density matrix ρ_{MLE} as a function of their index n, in logarithmic scale. Interestingly, despite the high dimensional cut-off $D_c = 120$, required by the IMLE protocol, for $n \geq 40$ the diagonal element $\rho_{\mathrm{MLE}}^{(n,n)} \leq 10^{-5}$. A possible explanation for this observation is that, during the iterative protocol, the IMLE algorithm explores a broader region of the approximated Hilbert space of dimension D_c. Further numerical experiments are required to shed light on this issue.

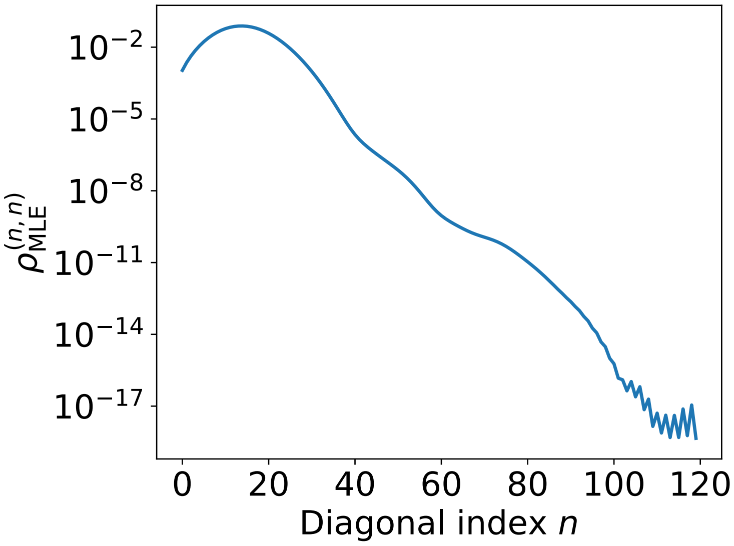

Figure 5.15: Diagonal elements of the reconstructed density matrix ρ_{MLE} plotted as a function of their index n in logarithmic scale.

To further analyze the properties of the most likely density matrix ρ_{MLE}, we compare its diagonal elements to the photon population distribution of an ideal coherent displaced state $|\alpha\rangle$. The diagonal elements of the density matrix of an ideal coherent state $|\alpha\rangle$ are given by Poisson distribution

$$p_n(\alpha) = e^{-|\alpha|^2}\frac{|\alpha|^{2n}}{n!}, \tag{5.31}$$

as shown in Ref. [31]. We fit the expression for $p_n(\alpha)$ against the diagonal elements of the most-likely density matrix ρ_{MLE}. We find that the coherent state with $\alpha = 3.78$ best fits the photon population statistics of ρ_{MLE}. The fidelity between ρ_{MLE} and $|\alpha = 3.78\rangle$ is 0.47, which indicates a substantial deviation of the density matrix obtained by the IMLE protocol from an ideal displaced state. The comparison between the photon population of ρ_{MLE} and the coherent state $|\alpha\rangle$ is shown in Figure 5.16.

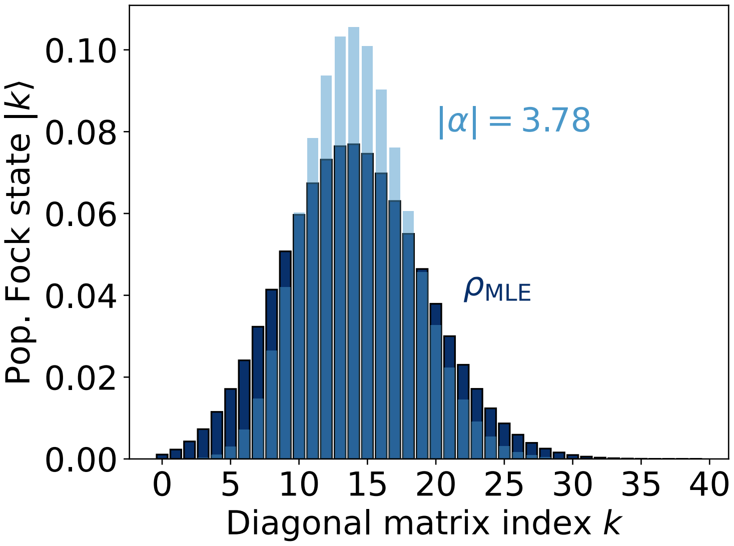

Figure 5.16: Figure (a), bar plot of the diagonal entries of the density matrix ρ_{MLE} (dark blue bars) and of the diagonal entries of the displaced states which fits best our data (light blue bars)

In order to benchmark the estimated density matrix ρ_{MLE}, we use it to compute the same expectation values evaluated in section 2.1.3 from the histogram of the mode $\hat{\xi}$. The results, shown in Figure 5.17, are in good agreement, within the statistical errors, to the ones estimated in section 2.1.3. This observation suggests that the estimated density matrix encodes the same physical information of the measured histogram for the mode $\hat{\xi}$. From the reconstructed density matrix, we also estimated $g^{(2)} = 1.06$, which is above the classical threshold of $g^{(2)} = 1$.

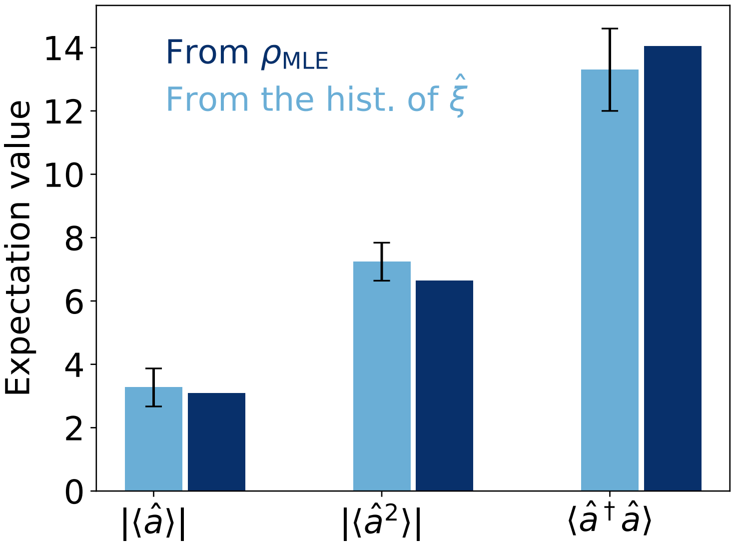

Figure 5.17: Comparison of the expectation values for the mode $\hat{a}$ obtained from the maximum likelihood density matrix ρ_{MLE} (dark-blue bars) and from the histogram of the measured mode $\hat{\xi}$ (light-blue bars) obtained in the previous section.

To conclude our analysis on the reconstructed density matrix ρ_{MLE}, we evaluate the Wigner function $W_{\mathrm{MLE}}(\alpha)$ using the built-in package contained in the Python package "QuTiP" [41], which implements a numerically stable Clenshaw algorithm [92] to perform the Weyl transform of the density matrix. The Wigner function $W_{\mathrm{MLE}}(\alpha)$ is plotted in Fig. 5.18 and, as expected, it shares the same physical features of the histograms presented in the previous sections.

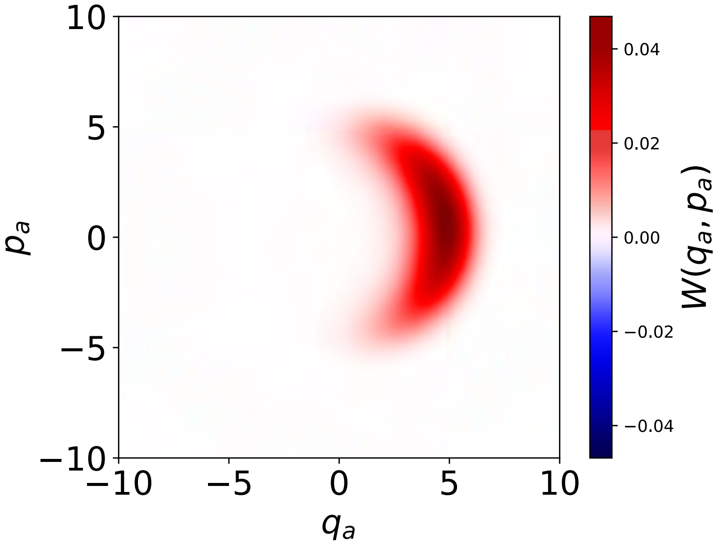

Figure 5.18: Wigner function $W(q,p)$ of the mode $\hat{a}$ obtained from the maximum-likehood density matrix ρ_{MLE}.

The reconstructed Wigner function W_{MLE} allows to compute the marginal distributions in the phase space for the quantum state ρ_{MLE}. Indeed, the marginal distribution $p_\theta(q)$ for the general quadrature $\hat{q}(\theta)$ can be obtained by integrating the Wigner function along the orthogonal quadrature $\hat{q}(\theta + \pi/2)$ (see Ref. [93]). Formally,

$$p_\theta(q) = \int dq_{\theta+\pi/2}\, W(q_\theta, q_{\theta+\pi/2}). \tag{5.32}$$

The marginal probability distributions $p_q(\theta)$ for $\theta = 0$ and $\theta = \pi/2$ are plotted in Fig. 5.19.

5.1.5 Reconstruction of the regularized P-function

In this section, we show how a regularized P-function $P_\Omega(\alpha)$ is reconstructed from the maximum likelihood density matrix ρ_{MLE} obtained in the section before. In the first part of this section, we briefly describe the concept of regularized P-functions. In the second part, we apply this concept to our measurements. We show that the regularized P-function of the field emitted by the JPC in its *steady-state* has a negative region in the phase-space. This result shows that the *steady-state* field emitted by the JPC has no classical analog.

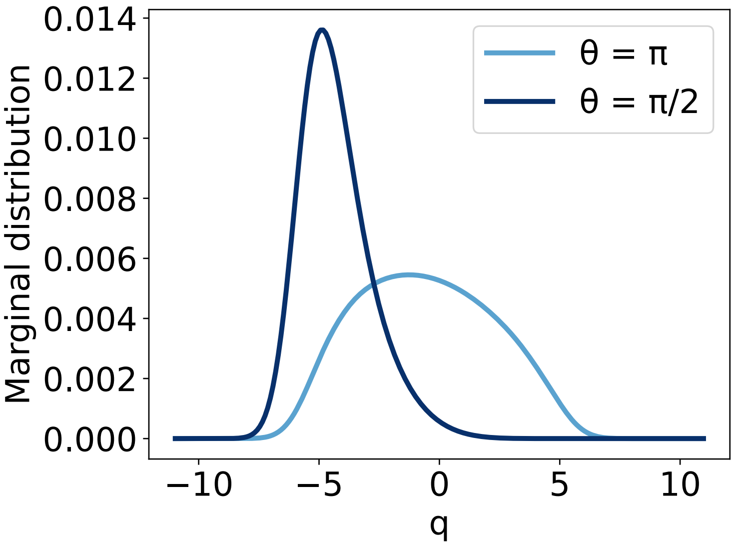

Figure 5.19: Figure (a), marginal distributions for the Wigner function $W(q,p)$ of the mode $\hat{a}$ for the angles $\theta = 0$ and $\theta = \pi/2$.

Regularized P-functions

The family of regularized P-functions is a relatively new theoretical tool to explore phase-space properties of quantum states; it has been analyzed theoretically by Kiesel and Vogel in Ref. [32].

For a quantum state with Glauber-Sudarshan P-function $P(\alpha)$ and a general integrable complex function $\Omega_w(\alpha)$, which we allow to depend on a real and positive parameter w, we define the regularized P-function $P_\Omega(\alpha)$ as the phase-space convolution,

$$P_\Omega(\alpha) = \iint_{\mathbb{C}} d^2z \, P(z) \, \Omega_w(\alpha - z). \tag{5.33}$$

The regularized P-function is analogous to the Glauber-Sudarshan P-function, where the main difference consists in the fact that P_Ω is always a continuous function in the phase-space. Also, as long as Ω_w belongs to the set of "non-classicality filters", the convolution in Eq. 5.33 preserves the physical information encoded in the Glauber-Sudarshan P-functionn $P(\alpha)$ without distorting it. As explained in Ref. [32], the set of "non-classicality filters" includes all complex functions $\Omega(\alpha)$, which satisfy the following properties

- *universality*: in order for the regularized P_Ω to be a continuous function in the phase space, for each non-classicality filter $\Omega_w(\alpha)$ we impose that $\Omega_w(\alpha)e^{|\alpha|^2/2}$ is a square-integrable [82] function in the space;
- *non-negativity*, each non-classicality filter $\Omega_w(\alpha)$ has non-negative Fourier transform.
- *Completeness with respect to the nonclassicality of the P-function*: the parameter w

represents the width of the filter. It may be introduced by the scaling relation

$$\Omega_w(\alpha) = \Omega_1\left(\frac{\alpha}{w}\right). \tag{5.34}$$

Moreover, when $w \to \infty$, i. e. for an infinitely wide filter, the convolution defined in Eq. 5.33 reduces to the identity:

$$\lim_{w\to\infty} P_\Omega(\alpha) = P(\alpha). \tag{5.35}$$

Recently, a rigorous and formal analysis of non-classicality filter functions $\Omega_w(\alpha)$ was conducted by Zartab et al. in Ref . [94]. Remarkably, the regularized P-function P_Ω can be used to detect the nonclassicality of any nonclassical state. The other way around, the negativities of the regularzed P function P_Ω are uniquely caused by the nonclassicality of the state, not by the filter Ω. In particular, for all nonclassical states, we can find a filter function Ω, such that the associated regularized P_Ω displays negativities.

Experimentally, regularized P-functions can be measured by sampling the phase-space marginal distributions of the quantum state, as shown for a squeezed vacuum state of light in Ref. [32] and for a photon-added thermal state, Ref. [95]; both experiments were conducted in the optical domain. More recently, regularized P-functions were used to experimentally explore the non-classical dynamics of polariton condensates by Lüders et al. in Ref. [96].

Calculation of P_Ω and results

In the following section, we use the filter function

$$\Omega_w(|\beta|) = \frac{2}{\pi}\left[\arccos\left(\frac{|\beta|}{2w}\right) - \frac{|\beta|}{2w}\sqrt{1-\frac{|\beta|^2}{4w^2}}\right]\mathrm{rect}\left(\frac{|\beta|}{4w}\right), \tag{5.36}$$

with $\mathrm{rect}(x) = 1$ if $x \leq 1/2$ and zero elsewhere. The filter Ω_w has been proved to be a non-classicality filter by Künh et al. in Ref. [97]. The filter width w is set to $w = 1.5$ in our analysis. From the maximum-likelihood density matrix ρ_{MLE}, we compute the regularized P-function $P_\Omega(\alpha)$ using

$$P_\Omega(\alpha) = \sum_{n,m=0}^{D_c} \rho_{\mathrm{MLE}}^{(n,m)} P_{\Omega,nm}(\alpha). \tag{5.37}$$

The coefficients $P_{\Omega,nm}(\alpha)$ entering ,in the last equation, are given by

$$\begin{aligned} P_{\Omega,nm}(\alpha) = \frac{16}{\pi^2} w^2 e^{i(n-m)\varphi_\alpha} \int_0^1 dz\, \Lambda_{nm}(2wz)z \\ \times J_{n-m}(4w|\alpha|z)\left[\arccos(z) - z\sqrt{1-z^2}\right] \end{aligned} \tag{5.38}$$

where $J_\alpha(x)$ belongs to the family of first-order Bessel functions and $\Lambda_{nm}(x)$ is defined as

$$\Lambda_{nm}(x) = \sqrt{\frac{m!}{n!}}\, |x|^{(n-m)} L_m^{(n-m)}(x^2), \tag{5.39}$$

where $L_n^k(x)$ is the generalized Laguerre polynomial. The expansion 5.37 in terms of the coefficients 5.38 has been proved by Krumm et al. in [98]. The filtered P-function $P_\Omega(\alpha)$ corresponding to the density matrix ρ_{MLE}, computed using equation 5.37 and the filter $\Omega(\alpha)$ defined in 5.36, is plotted in Figure 5.20. The negative phase-space region of P_Ω can clearly be distinguished: it indicates that the reconstructed state does not have a classical analog.

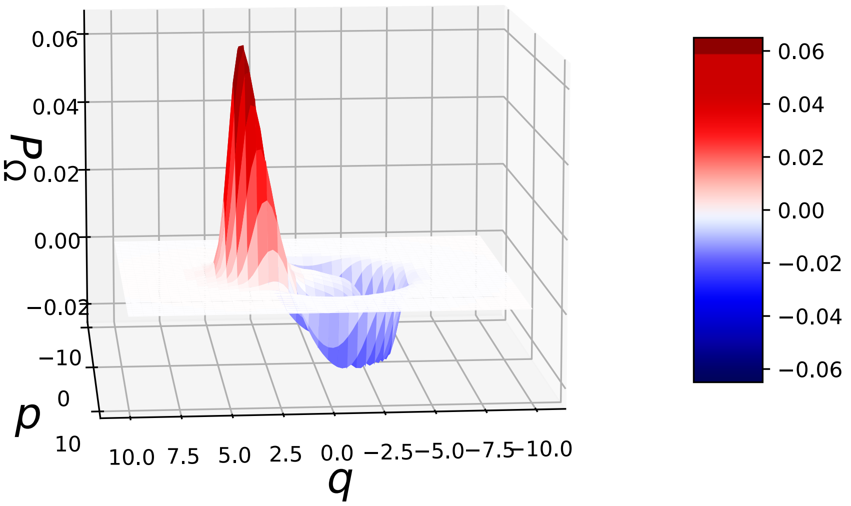

Figure 5.20: Regularized P-function $P_\Omega(\alpha)$ computed from the density matrix ρ_{MLE} estimated in the previous section for the input drive power set to -100 dBm. The width of the filter Ω defined in equation 5.36 is set to $w = 1.5$.

In Figure 5.21 we plot the cross-section of the function $P_\Omega(\alpha)$ across the real-axis.

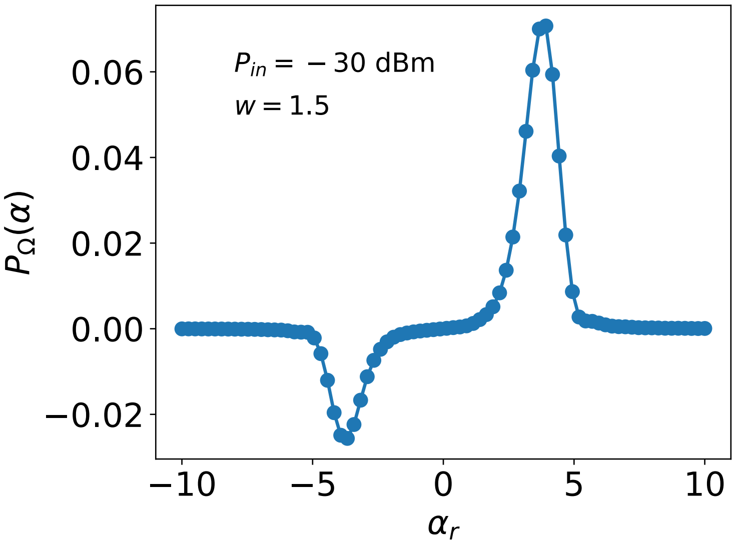

Figure 5.21: Cross section of the regularized P-function $P_\Omega(\alpha)$ across the real axis. The function was computed from the density matrix ρ_{MLE} estimated in the previous section for the input drive power set to −30 dBm, referred to the source (−100 dBm at the device). The width of the filter Ω defined in equation 5.36 is set to $w = 1.5$.

This result suggests that the radiation emitted by the JPC in its *steady-state* does not have classical analogs. While this result is interesting in itself, further investigations may prove the usefulness of this result in the context of quantum information processing.

5.2 Results of JPA measurements

In this section, we describe the experimental results obtained by analyzing the steady-state emission of the JPA. We operate the device by pumping it with a microwave signal at twice its resonance frequency: the pump was fed into the device through its pump port while, through its signal port, the device is subject to weak thermal fluctuations.
We provide a qualitative description of the measured histograms, showing the emergence of bistability in the high pump power regime. In the bistable regime, we show that the quantum state is described by a classical mixture of two displaced coherent states, symmetrical with respect to the origin of the phase-space, as predicted by the theoretical model described in Chapter 4. In practice, we experimentally show the transition in the JPA operation to the bistable regime by increasing the pump power. Also, in accordance with the quantum theory, the transition happens continuously without a discontinuous jump in the derivative of the photon population with respect to the pump power: this is in contrast with the predictions of the mean-field theory.

5.2.1 Discussion of the results

The JPA is operated by setting its coil current to 68 μA. The pump power is varied in 51 steps from −46 dBm to −31 dBm (estimated at the device). For each value of the pump power, we measure 50 traces of 16.384 (I,Q)-points which are then averaged and collected in two-dimensional histograms as described in section 5.1. We stress that from the measured histogram we can evaluate directly the expectation values for the amplified field mode operator $\hat{\xi}$. From these expectation values, we can compute the ones of the field mode $\hat{a}$ by using the Caves relation 5.14.

In Figure 5.22, we show the sampled histograms of the mode $\hat{\xi}$ for different values of the pump power. Going from a low pump power, −46 dBm, to an high pump power, −31 dBm, we observe how the histogram's shape changes: going from a single-peaked Gaussian state to a double-peaked distribution. This transition is in good agreement with the theoretical model explained in Chapter 4.

(a) $P_p = -46$ dBm **(b)** $P_p = -41.5$ dBm

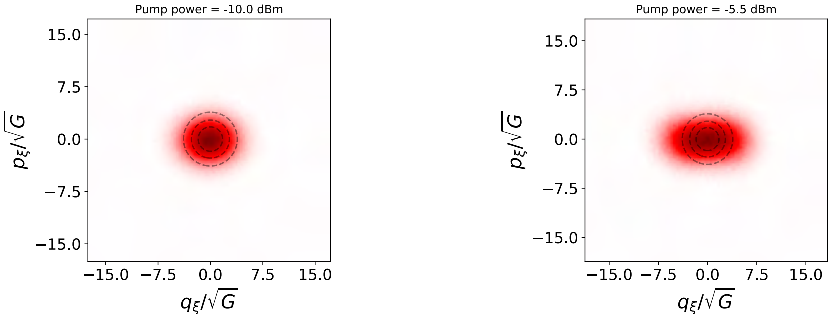

(c) $P_p = -37.6$ dBm **(d)** $P_p = -31$ dBm

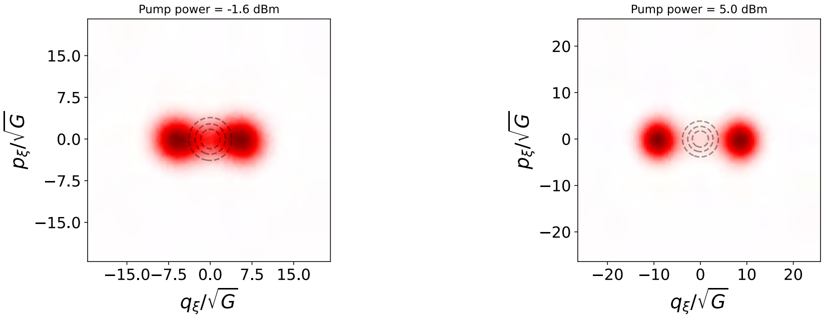

Figure 5.22: Histograms of the mode $\hat{\xi}$ for the JPA subject to different pump powers. All the histograms are normalized from zero to one. The gray dashed lines indicate the contour plot of the noise mode $\hat{v}$. The pump power P_p in the captions refers to the value estimated at the device (−36 dB compared to the value at the source). The pump powers in the title of the figures refers to the pump power at the source.

We take a look at the time traces of the sampled I points. In particular, we consider time traces of duration 40 μs, which is enough to show 500 values of the demodulated points. The time traces for four different values of the pump powers are shown in Figure 5.23. Interestingly, the transition from a Gaussian squeezed state to a mixed state of two displaced coherent states can be observed from the time traces. For low pump powers, the values of the demodulated I quadratures fluctuate around their mean, which is zero. For higher values of the pump power, the fluctuations around zero are replaced by random jumps between two points I_{max} and $I_{\text{min}} \simeq -I_{\text{max}}$, approximately symmetric around zero. The points I_{max} and I_{min} correspond to the horizontal coordinates of the double peaks of the measured histograms. This observation agrees with the theoretical picture that, in the high pump limit, the steady state radiation emitted by the JPA describes a symmetric mixture of two displaced coherent states.

(a) $P_p = -46$ dBm

(c) $P_p = -41.5$ dBm

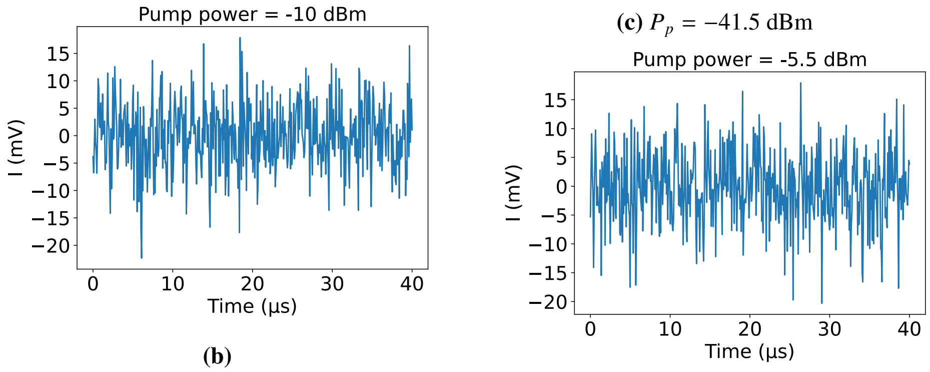

(b)

(d) $P_p = -37.6$ dBm

(f) $P_p = -31$ dBm

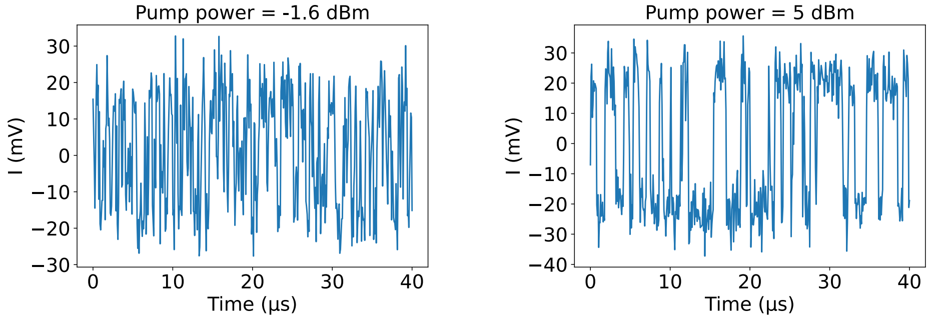

(e) **(g)**

Figure 5.23: Time traces of the measured quadrature I for different values of the JPA input power. The pump power P_p in the captions refers to the value estimated at the device (−36 dB compared to the value at the source).

In Fig. 5.24, we compare the histograms of the measured I values for the lowest and highest values of the considered pump powers, for a time trace of 16.384 (I,Q) points. Coming back to the measured two-dimensional histograms, we evaluate the average photon population,$\langle \hat{a}^\dagger \hat{a} \rangle$, of the mode $\hat{a}$. This quantity is shown as a function of the pump power in Fig. 5.25. The average photon population of the field emitted by the JPA monotonically increases as a function of the pump power, as expected from both the mean-field and full quantum theory presented in Chapter 4. In the right panel of Figure 5.25, we show the derivative of $\langle \hat{a}^\dagger \hat{a} \rangle$ with respect to the

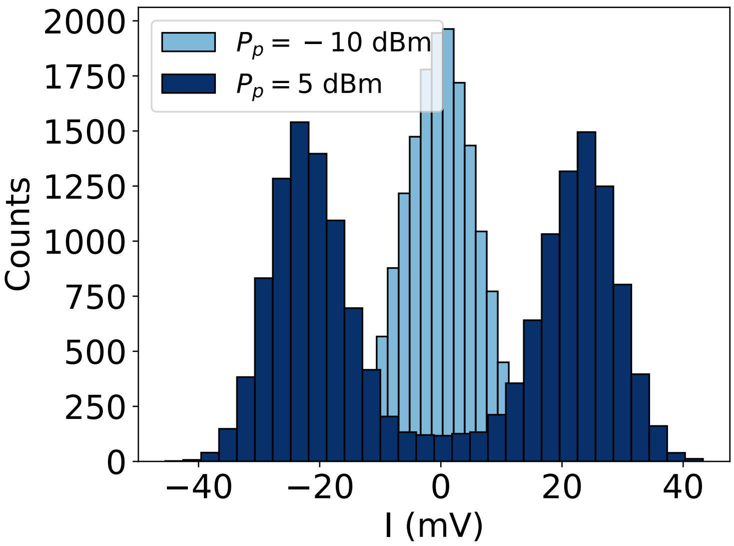

Figure 5.24: Histograms of the measured I values for the lowest and highest values of the considered pump powers for the full time-traces of 16.384 (I,Q) points. Here the pump powers are referred to the source (to estimate the power at the device, we need to consider the −36 dB attenuation on the pump-line of the JPA).

pump power. It is estimated as

$$\frac{d}{dP_p}\langle\hat{a}^\dagger\hat{a}\rangle \simeq \frac{\langle\hat{a}^\dagger\hat{a}\rangle(P_p+\Delta P_p)-\langle\hat{a}^\dagger\hat{a}\rangle(P_p)}{\Delta P_p}, \tag{5.40}$$

where $\Delta P_p = 0.29$ dBm is the difference between two consecutive pump powers. The derivate of the average photon population with respect to the pump power is always continuous function and does not show the divergence predicted by the mean-field theory in Chapter 4. This observation confirms that the transition to the bistable regime is indeed continuous, as predicted by the full quantum-theory, and is not a second-order phase transition, as predicted by the semiclassical mean-field theory. Then, we evaluate the second-order correlation function $g^{(2)}$ as a function of the pump power. The correlation function $g^{(2)} \to \infty$ in the limit of low pump powers and $g^{(2)} \to 1$ in the high pump powers limit. Both limits are expected from the quantum theory of the JPA developed in Chapter 4. Finally, if a quantum state ρ is described by the symmetric mixture of two displaced coherent states $|\alpha\rangle$ and $|-\alpha\rangle$,

$$\rho = \frac{1}{2}\left(|\alpha\rangle\langle\alpha| + |-\alpha\rangle\langle-\alpha|\right), \tag{5.41}$$

the average photon population is given by

$$\langle\hat{a}^\dagger\hat{a}\rangle = \mathrm{Tr}\left(\hat{a}^\dagger\hat{a}\,\rho\right) = |\alpha|^2, \tag{5.42}$$

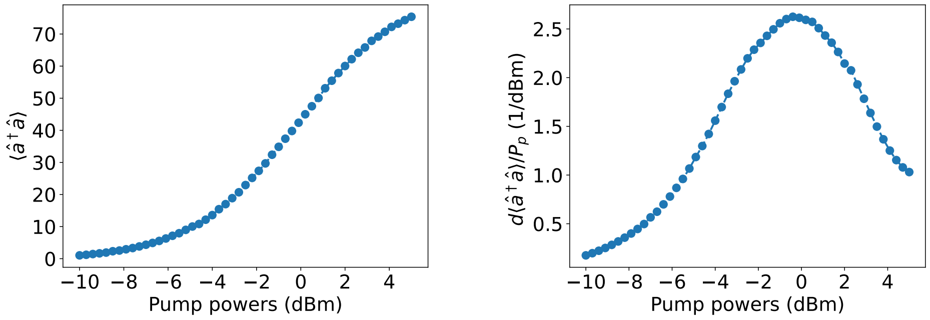

(a) **(b)**

Figure 5.25: Average photon population $\langle \hat{a}^\dagger \hat{a} \rangle$, figure (a), and derivative of the average population with respect to the pump power, figure (b), as a function of the pump powers. Here the pump powers are referred to the source (to estimate the power at the device, we need to consider the −36 dB attenuation on the pump-line of the JPA).

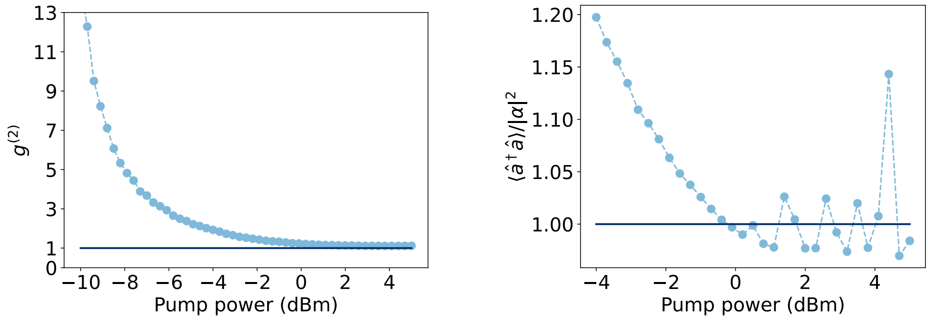

(a) **(b)**

Figure 5.26: Second order correlation function $g^{(2)}$, Figure (a), and ratio between $\langle \hat{a}^\dagger \hat{a} \rangle$ and $|\alpha|^2$, Figure (b), as a function of the pump power. Here the pump powers are referred to the source (to estimate the power at the device, we need to consider the −36 dB attenuation on the pump-line of the JPA).

and therefore

$$\frac{\langle \hat{a}^\dagger \hat{a} \rangle}{|\alpha|^2} = 1. \tag{5.43}$$

We test this prediction for our measured histograms: we evaluate the ratio $\langle \hat{a}^\dagger \hat{a} \rangle / |\alpha|^2$ as a function of the pump power. The results are presented in the right panel of Figure 5.26. As expected, the ratio $\langle \hat{a}^\dagger \hat{a} \rangle / |\alpha|^2 \to 1$ in the high pump power limit, is in agreement with our theoretical prediction. The result suggests that the steady state emitted by the JPA is a classical mixture of two displaced coherent states and not a superposition of them.

5.2.2 Phase-space simmetry

For each value of the pump power, the marginal distributions of the measured histograms for the mode $\hat{\xi}$ were fitted to a double-peak Gaussian model,

$$f_H(q; A_1, A_2, \mu_1, \mu_2, \sigma_1, \sigma_2) = \mathcal{N} \cdot \sum_{j=1,2} A_j e^{-(q-\mu_j/\sigma_j)^2}, \tag{5.44}$$

where the symmetry of the marginal distribution was not imposed *a-priori*. The double-peaked gaussian model describes accurately the experimental data, as shown in Figure 5.27 for the pump powers $P_p = -37.6$ dBm and $P_p = -31$ dBm. To prove that the measured marginal distributions are symmetrical with respect to a reflection in the phase-space, we measure the difference in the parameters entering in the definition of the double-peaked Gaussian model. In particular, we plot, as a function of the pump power, the differences $A_1 - A_2$, $\sigma_1 - \sigma_2$ and $\mu_1 - \mu_2$. The plots are shown in Figure 5.28. All three differences are compatible with zero within their statistical errors. This observation shows that $A_1 \approx A_2$, $\mu_1 \approx \mu_2$ and $\sigma_1 \approx \sigma_2$ and therefore the marginal distributions are described by a sum of two identical gaussian functions centered in symmetric points on the real line. To further test the symmetry of the measured marginal distributions, we measured the symmetry integral

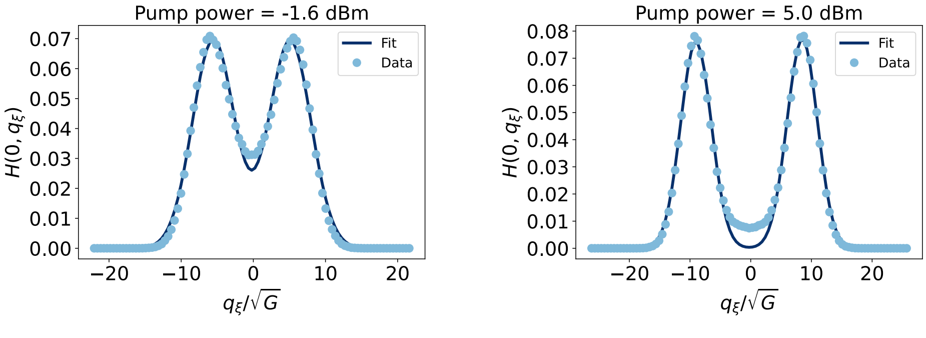

(a) **(b)**

Figure 5.27: Measured marginal distributions (light-blue dot) as a function of the coordinate q for the pump powers $P_p = -1.6$ dBm, Panel (a), and $P_p = 5$ dBm, Panel (b). The data are fitted with a double-peaked Gaussian model (dark-blue solid line). Here the pump powers are referred to the source (to estimate the power at the device, we need to consider the −36 dB attenuation on the pump-line of the JPA).

$$S = \int_{\mathbb{R}} dq \left| f(q) - f(-q) \right| . \tag{5.45}$$

When the function is even, i.e. invariant by inversion, $S = 0$. The integral S is plotted as a function of the pump powers in the bottom right panel of Figure 5.28. To analyze the result numerically, we consider identically"zero" all the floating point numbers smaller than 10^{-15}. Interestingly, $S \approx 10^{-18}$ for all values of the pump powers. In light of the tests here presented and their results, we conclude that the measured quantum state of light emitted by the JPA in its steady state always preserves its reflection symmetry in the phase-space. This conclusion is consistent with our choice to describe the JPA with the Hamiltonian of a KPO.

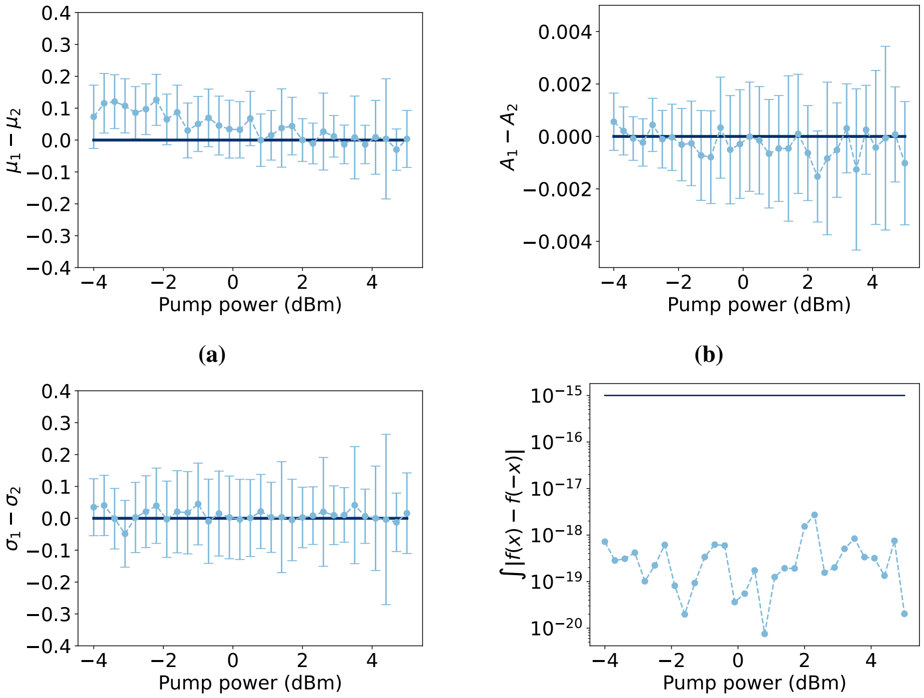

(a) **(b)**

(c) **(d)**

Figure 5.28: Fitteded differences $\mu_1 - \mu_2$, Figure (a),$\sigma_1 - \sigma_2$, Figure (b), and $A_1 - A_2$, Figure (c), as a function of the pump powers. The dark-blue solid lines indicate the expected value 0. In Figure (d), the results of the symmetric integral S (light-blue marks), defined in 5.45, are plotted as a function of the pump powers. The dark blue solid line indicates the floating value 10^{-15}. Here the pump powers are referred to the source (to estimate the power at the device, we need to consider the −36 dB attenuation on the pump-line of the JPA).

5.3 Conclusion

In this chapter, we presented the experimental results obtained analyzing the steady-state radiation emitted by two superconducting quantum devices at cryogenic temperatures: a JPC and a JPA. For the JPC, we analyzed the histograms obtained by measuring the emitted radiation in its steady state, while driving it with a resonant input signal. We also tested the IMLE protocol applied to heterodyne detection, which was implemented during this thesis work. The protocol was implemented by combining it with the Lucy-Richardson deconvolution technique, an approach that helps reduce its numerical complexity and allows for a more efficient reconstruction of the quantum state. The expectation values obtained from the reconstructed density matrix are in good agreement with the ones computed from the measured histograms. From the reconstructed density matrix, we were also able to perform the Wigner tomography of the quantum state, by computing the Wigner function from the Weyl transform of the density matrix. Moreover, we calculated the regularized P-function P_Ω for a particular choice of the filter Ω. The regularized P-function assumes negative values in the phase space. This observation confirms that the radiation emitted by the JPC in its steady-state has no-classical analogs, i.e. the features of the emitted radiation can be accounted for only in the framework of a full quantum theory.

For the JPA, we performed a simpler analysis due to time constraints. We measured the histograms for the radiation emitted in the steady state for different values of the pump power. We experimentally showed how the steady-state shifts from a mono-stable to a bi-stable regime by increasing the pump power. This transition, in accordance with quantum theory, happens smoothly as a function of the pump power. We also show that the measured histograms are symmetric with respect to the inversion in the phase space. Moreover, in the high pump power limit, the steady-state histograms are well described as a mixture of two displaced coherent states which is symmetric by inversion in the phase-space. Both observations confirm our assumption that the JPA can be modeled effectively by the Hamiltonian of a Kerr Parametric Oscillator (KPO).

Conclusion and outlook

In this thesis, we have analyzed the theoretical and experimental results obtained by studying the steady-state microwave emission from two superconducting quantum circuits.
Theoretically, we have revisited the theory of one-photon and two-photon driven Kerr oscillators. For both models, we have presented the analytical linear approximations and the full numerical solutions, both in the *steady state* and *transient state* regimes. The numerical solutions have been obtained using an approach based on the linearization of the master's equation by means of the Choi-Jamiolkvosky isomorphism.

Experimentally, we have aimed to verify our theory predictions. All our quantum measurements have been based on the photon number calibration routines of the amplification chain. Here, we have directly shown the gaussian nature of the noise introduced by the amplification chain. We note that this calibration is fundamental in order to deconvolve the effects of the amplification chain and obtain the underlying density matrices of quantum states emitted by the superconducting devices. In the following, we have analyzed the radiation emitted by the JPC in its *steady-state*. The JPC is operated by driving it with a resonant coherent signal, thus realizing a one-photon driven Kerr oscillator. The propagating signal from the JPC has been reconstructed using a quantum tomography method which relies on the combination of the Lucy-Richardson deconvolution technique and the IMLE protocol explained in Chapter 2. This tomographic protocol does not make any assumption on the state to be reconstructed, thus being completely general and state-independent. We have extracted the density matrix of the JPC for two different values of the power of the resonant coherent signal. The expectation values computed from this reconstructed density matrix have been compared to the ones extracted directly from the measured histogram of the amplified microwave signal detected by the FPGA: the results agree within the experimental errors, which means that the assumption-free tomographic protocol is successful in reconstructing physical information encoded in the propagating quantum microwave signal. Furthermore, using the concept of regularized P-function, we have shown how the reconstructed signal does not have classical analogs. This result suggests that some of the non-classical features of the single-photon driven Kerr oscillator survive in the *steady state*. Then, we have analyzed the radiation emitted by the JPA, which has been operated by pumping it with an external coherent signal at twice its resonant frequency and realizes the two-photon driven Kerr oscillator. As expected from the theoretical model presented in Chapter 4, the steady state of the JPA shows a transition to a bistable classical mixture of displaced coherent states for high pump powers. This transition in confirmed by analyzing the time traces of the sampled (I, Q)-points and the measured histogram of the amplified propagating signal sampled by the FPGA.

In the outlook, our results can be expanded by exploring the transient regime of the superconducting quantum circuits. For this, the methods developed in this thesis can serve as a solid foundation for reaching that next milestone. Furthermore, the IMLE reconstruction from the histogram of propagating microwave signals is a powerful and flexible tool that doesn't require any prior knowledge of the state-to-be reconstructed and can be applied in all experiments requiring the tomography of propagating microwave radiation.

Bibliography

[1] M. A. A. Caballero. *A Setup for Quantum Signal Detection in a Circuit QED Architecture*. Ph.D. thesis, Technische Universität München (2008).

[2] F. Arute, K. Arya, R. Babbush, D. Bacon, J. C. Bardin, R. Barends, R. Biswas, S. Boixo, F. G. S. L. Brandao, D. A. Buell, B. Burkett, Y. Chen, Z. Chen, B. Chiaro, R. Collins, W. Courtney, A. Dunsworth, E. Farhi, B. Foxen, A. Fowler, C. Gidney, M. Giustina, R. Graff, K. Guerin, S. Habegger, M. P. Harrigan, M. J. Hartmann, A. Ho, M. Hoffmann, T. Huang, T. S. Humble, S. V. Isakov, E. Jeffrey, Z. Jiang, D. Kafri, K. Kechedzhi, J. Kelly, P. V. Klimov, S. Knysh, A. Korotkov, F. Kostritsa, D. Landhuis, M. Lindmark, E. Lucero, D. Lyakh, S. Mandrà, J. R. McClean, M. McEwen, A. Megrant, X. Mi, K. Michielsen, M. Mohseni, J. Mutus, O. Naaman, M. Neeley, C. Neill, M. Y. Niu, E. Ostby, A. Petukhov, J. C. Platt, C. Quintana, E. G. Rieffel, P. Roushan, N. C. Rubin, D. Sank, K. J. Satzinger, V. Smelyanskiy, K. J. Sung, M. D. Trevithick, A. Vainsencher, B. Villalonga, T. White, Z. J. Yao, P. Yeh, A. Zalcman, H. Neven & J. M. Martinis. Quantum supremacy using a programmable superconducting processor. *Nature* **574**, 505–510 (2019).

[3] L. Steffen, Y. Salathe, M. Oppliger, P. Kurpiers, M. Baur, C. Lang, C. Eichler, G. Puebla-Hellmann, A. Fedorov & A. Wallraff. Deterministic quantum teleportation with feed-forward in a solid state system. *Nature* **500**, 319–322 (2013).

[4] N. Gisin & R. Thew. Quantum communication. *Nat. Photonics* **1**, 165–171 (2007).

[5] R. Alléaume, F. Treussart, G. Messin, Y. Dumeige, J.-F. Roch, A. Beveratos, R. Brouri-Tualle, J.-P. Poizat & P. Grangier. Experimental open-air quantum key distribution with a single-photon source. *New J. Phys.* **6**, 92 (2004).

[6] S. Pirandola, B. R. Bardhan, T. Gehring, C. Weedbrook & S. Lloyd. Advances in photonic quantum sensing. *Nat. Photonics* **12**, 724–733 (2018).

[7] M. Schlosshauer. *Decoherence* (Springer, Berlin, Germany). URL `https://link.springer.com/book/10.1007/978-3-540-35775-9`.

[8] B. E. Stumborg, K. A. Baerenklau & R. C. Bishop. *Fluctuating Nonlinear Oscillators: From Nanomechanics to Quantum Superconducting Circuits*, Vol. 23 (Oxford University Press, Oxford, England, UK, 2001).

[9] C. K. Andersen, A. Kamal, N. A. Masluk, I. M. Pop, A. Blais & M. H. Devoret. Quantum Versus Classical Switching Dynamics of Driven Dissipative Kerr Resonators. *Phys. Rev. Appl.* **13**, 044017 (2020).

[10] I. Siddiqi, R. Vijay, F. Pierre, C. M. Wilson, L. Frunzio, M. Metcalfe, C. Rigetti, R. J. Schoelkopf, M. H. Devoret, D. Vion & D. Esteve. Direct Observation of Dynamical Bifurcation between Two Driven Oscillation States of a Josephson Junction. *Phys. Rev. Lett.* **94**, 027005 (2005).

[11] M. Renger, S. Pogorzalek, Q. Chen, Y. Nojiri, K. Inomata, Y. Nakamura, M. Partanen, A. Marx, R. Gross, F. Deppe & K. G. Fedorov. Beyond the standard quantum limit for parametric amplification of broadband signals. *npj Quantum Inf.* **7**, 1–7 (2021).

[12] A. Grimm, N. E. Frattini, S. Puri, S. O. Mundhada, S. Touzard, M. Mirrahimi, S. M. Girvin, S. Shankar & M. H. Devoret. Stabilization and operation of a Kerr-cat qubit. *Nature* **584**, 205–209 (2020).

[13] S. Puri, S. Boutin & A. Blais. Engineering the quantum states of light in a Kerr-nonlinear resonator by two-photon driving. *npj Quantum Inf.* **3**, 1–7 (2017).

[14] H. Goto, Z. Lin, T. Yamamoto & Y. Nakamura. On-demand generation of traveling cat states using a parametric oscillator. *Phys. Rev. A* **99**, 023838 (2019).

[15] Z. Wang, M. Pechal, E. A. Wollack, P. Arrangoiz-Arriola, M. Gao, N. R. Lee & A. H. Safavi-Naeini. Quantum Dynamics of a Few-Photon Parametric Oscillator. *Phys. Rev. X* **9**, 021049 (2019).

[16] M. H. Devoret & R. J. Schoelkopf. Superconducting Circuits for Quantum Information: An Outlook. *Science* **339**, 1169–1174 (2013).

[17] T. Niemczyk, F. Deppe, H. Huebl, E. P. Menzel, F. Hocke, M. J. Schwarz, J. J. Garcia-Ripoll, D. Zueco, T. Hümmer, E. Solano, A. Marx & R. Gross. Circuit quantum electrodynamics in the ultrastrong-coupling regime. *Nat. Phys.* **6**, 772–776 (2010).

[18] R. J. Schoelkopf & S. M. Girvin. Wiring up quantum systems. *Nature* **451**, 664–669 (2008).

[19] A. Wallraff, D. I. Schuster, A. Blais, L. Frunzio, R.-S. Huang, J. Majer, S. Kumar, S. M. Girvin & R. J. Schoelkopf. Strong coupling of a single photon to a superconducting qubit using circuit quantum electrodynamics. *Nature* **431**, 162–167 (2004).

[20] X. H. H. Zhang & H. U. Baranger. Driven-dissipative phase transition in a Kerr oscillator: From semiclassical $\mathcal{PT}$ symmetry to quantum fluctuations. *Phys. Rev. A* **103**, 033711 (2021).

[21] N. Bartolo, F. Minganti, W. Casteels & C. Ciuti. Exact steady state of a Kerr resonator with one- and two-photon driving and dissipation: Controllable Wigner-function multimodality and dissipative phase transitions. *Phys. Rev. A* **94**, 033841 (2016).

[22] D. F. Walls & G. J. Milburn. *Quantum Optics* (Springer, Berlin, Germany). URL `https://link.springer.com/book/10.1007/978-3-642-79504-6`.

[23] A. A. Clerk, M. H. Devoret, S. M. Girvin, F. Marquardt & R. J. Schoelkopf. Introduction to quantum noise, measurement, and amplification. *Rev. Mod. Phys.* **82**, 1155–1208 (2010).

[24] J. J. Sakurai & J. Napolitano. *Modern Quantum Mechanics* (Cambridge University Press, Cambridge, England, UK, 2017).

[25] E. C. G. Sudarshan. Equivalence of Semiclassical and Quantum Mechanical Descriptions of Statistical Light Beams. *Phys. Rev. Lett.* **10**, 277–279 (1963).

[26] E. Wigner. On the Quantum Correction For Thermodynamic Equilibrium. *Phys. Rev.* **40**, 749–759 (1932).

[27] K. Husimi. Some Formal Properties of the Density Matrix. *Proceedings of the Physico-Mathematical Society of Japan. 3rd Series* **22**, 264–314 (1940).

[28] W. P. Schleich. *Quantum Optics in Phase Space* (2001).

[29] R. J. Glauber. Coherent and Incoherent States of the Radiation Field. *Phys. Rev.* **131**, 2766–2788 (1963).

[30] U. M. Titulaer & R. J. Glauber. Correlation Functions for Coherent Fields. *Phys. Rev.* **140**, B676–B682 (1965).

[31] C. Gerry & P. Knight. *Introductory Quantum Optics* (Cambridge University Press, Cambridge, England, UK, 2004).

[32] T. Kiesel & W. Vogel. Nonclassicality filters and quasiprobabilities. *Phys. Rev. A* **82**, 032107 (2010).

[33] W. B. Case. Wigner functions and Weyl transforms for pedestrians. *Am. J. Phys.* **76**, 937–946 (2008).

[34] C. W. Gardiner & M. J. Collett. Input and output in damped quantum systems: Quantum stochastic differential equations and the master equation. *Phys. Rev. A* **31**, 3761–3774 (1985).

[35] M.-D. Choi. Completely positive linear maps on complex matrices. *Linear Algebra Appl.* **10**, 285–290 (1975).

[36] A. Jamiołkowski. Linear transformations which preserve trace and positive semidefiniteness of operators. *Rep. Math. Phys.* **3**, 275–278 (1972).

[37] G. Lindblad. On the generators of quantum dynamical semigroups. *Commun. Math. Phys.* **48**, 119–130 (1976).

[38] F. Minganti, I. I. Arkhipov, A. Miranowicz & F. Nori. Continuous Dissipative Phase Transitions without Symmetry Breaking. *arXiv* (2021).

[39] E. Carlen & M. C. Carvalho. *Linear Algebra: From the Beginning* (W. H. Freeman, 2006). URL `https://books.google.it/books?id=EqGjBOXbPAoC&pg=PA217&redir_esc=y`.

[40] J. R. Dormand & P. J. Prince. A family of embedded Runge-Kutta formulae. *J. Comput. Appl. Math.* **6**, 19–26 (1980).

[41] J. R. Johansson, P. D. Nation & F. Nori. QuTiP 2: A Python framework for the dynamics of open quantum systems. *arXiv* (2012).

[42] G. H. Golub & C. F. Van Loan. *Matrix Computations* (Johns Hopkins University Press, Baltimore, MD, USA, 1996). URL `https://books.google.it/books?id=mlOa7wPX6OYC&pg=PA470&redir_esc=y#v=onepage&q&f=false`.

[43] scipy.sparse.linalg.eigsh — SciPy v1.11.2 Manual. URL `https://docs.scipy.org/doc/scipy/reference/generated/scipy.sparse.linalg.eigsh.html`. [Online; accessed 26. Sep. 2023] (2023).

[44] B. D. Josephson. Possible new effects in superconductive tunnelling. *Physics Letters* **1**, 251–253 (1962).

[45] A. Barone & G. Paternò. *Physics and Applications of the Josephson Effect* (1982).

[46] R. C. Jaklevic, J. Lambe, A. H. Silver & J. E. Mercereau. Quantum Interference Effects in Josephson Tunneling. *Phys. Rev. Lett.* **12**, 159–160 (1964).

[47] M. Sandberg, C. M. Wilson, F. Persson, T. Bauch, G. Johansson, V. Shumeiko, T. Duty & P. Delsing. Tuning the field in a microwave resonator faster than the photon lifetime. *Appl. Phys. Lett.* **92** (2008).

[48] B. Yurke, L. R. Corruccini, P. G. Kaminsky, L. W. Rupp, A. D. Smith, A. H. Silver, R. W. Simon & E. A. Whittaker. Observation of parametric amplification and deamplification in a Josephson parametric amplifier. *Phys. Rev. A* **39**, 2519–2533 (1989).

[49] T. Yamamoto, K. Inomata, M. Watanabe, K. Matsuba, T. Miyazaki, W. D. Oliver, Y. Nakamura & J. S. Tsai. Flux-driven Josephson parametric amplifier. *Appl. Phys. Lett.* **93** (2008).

[50] D. M. Pozar. *Microwave Engineering* (Wiley, 2012).

[51] G. M. D'Ariano, M. G. A. Paris & M. F. Sacchi. Quantum Tomography. *arXiv* (2003).

[52] J. Řeháček, Z. Hradil & M. Ježek. Iterative algorithm for reconstruction of entangled states. *Phys. Rev. A* **63**, 040303 (2001).

[53] C. M. Caves. Quantum limits on noise in linear amplifiers. *Phys. Rev. D* **26**, 1817–1839 (1982).

[54] F. Mallet, M. A. Castellanos-Beltran, H. S. Ku, S. Glancy, E. Knill, K. D. Irwin, G. C. Hilton, L. R. Vale & K. W. Lehnert. Quantum State Tomography of an Itinerant Squeezed Microwave Field. *Phys. Rev. Lett.* **106**, 220502 (2011).

[55] M. A. Nielsen & I. L. Chuang. *Quantum Computation and Quantum Information: 10th Anniversary Edition* (Cambridge University Press, Cambridge, England, UK, 2010).

[56] S. Kullback & R. A. Leibler. On Information and Sufficiency. *Ann. Math. Stat.* **22**, 79–86 (1951).

[57] D. Coppersmith & S. Winograd. Matrix multiplication via arithmetic progressions. *J. Symbolic Comput.* **9**, 251–280 (1990).

[58] A. I. Lvovsky. Iterative maximum-likelihood reconstruction in quantum homodyne tomography. *J. Opt. B: Quantum Semiclassical Opt.* **6**, S556 (2004).

[59] M. S. Kim. Quasiprobability functions measured by photon statistics of amplified signal fields. *Phys. Rev. A* **56**, 3175–3179 (1997).

[60] P. Virtanen, R. Gommers, T. E. Oliphant, M. Haberland, T. Reddy, D. Cournapeau, E. Burovski, P. Peterson, W. Weckesser, J. Bright, S. J. van der Walt, M. Brett, J. Wilson, K. J. Millman, N. Mayorov, A. R. J. Nelson, E. Jones, R. Kern, E. Larson, C. J. Carey, İ. Polat, Y. Feng, E. W. Moore, J. VanderPlas, D. Laxalde, J. Perktold, R. Cimrman, I. Henriksen, E. A. Quintero, C. R. Harris, A. M. Archibald, A. H. Ribeiro, F. Pedregosa, P. van Mulbregt & SciPy 1.0 Contributors. SciPy 1.0: Fundamental Algorithms for Scientific Computing in Python. *Nature Methods* **17**, 261–272 (2020).

[61] K. Huang. *Statistical Mechanics, 2nd Edition* (Wiley, Hoboken, NJ, USA, 1988). URL `https://www.wiley.com/en-gb/Statistical+Mechanics,+2nd+Edition-p-9780471815181`.

[62] SC-219/50-NbTi-NbTi | COAX CO., LTD. URL `http://www.coax.co.jp/en/product/sc/219-50-nbti-nbti.html`. [Online; accessed 19. Sep. 2023] (2023).

[63] HUBER+SUHNER Radio frequency. URL `https://literature.hubersuhner.com/Technologies/Radiofrequency/MicrowavecabelesEN/`

?gotofirstsearchresult=Minibend%20KR-10&page=98. [Online; accessed 19. Sep. 2023] (2023).

[64] B. Abdo, A. Kamal & M. H. Devoret. Non-degenerate, three-wave mixing with the Josephson ring modulator. *arXiv* (2012).

[65] R. Neagu. FPGA-based Tomography of Propagating Quantum Microwaves (2019).

[66] PXIe-5775 Specifications - NI. URL https://www.ni.com/docs/de-DE/bundle/pxie-5775-specs/page/specs.html. [Online; accessed 8. Jul. 2023] (2023).

[67] Single-Cycle Timed Loop FAQ for the LabVIEW FPGA Module - NI. URL https://knowledge.ni.com/KnowledgeArticleDetails?id=kA00Z000000P8sWSAS&l=de-DE. [Online; accessed 17. Aug. 2023] (2017).

[68] T. Schilcher. RF applications in digital signal processing. *CERN Document Server* (2008).

[69] Why is np.dot so much faster than np.sum? URL https://stackoverflow.com/questions/75556221/why-is-np-dot-so-much-faster-than-np-sum. [Online; accessed 20. Sep. 2023] (2023).

[70] G. D'Antona & A. Ferrero. *Digital Signal Processing for Measurement Systems* (Springer US). URL https://link.springer.com/book/10.1007/0-387-28666-7.

[71] M. Mariantoni, E. P. Menzel, F. Deppe, M. Á. Araque Caballero, A. Baust, T. Niemczyk, E. Hoffmann, E. Solano, A. Marx & R. Gross. Planck Spectroscopy and Quantum Noise of Microwave Beam Splitters. *Phys. Rev. Lett.* **105**, 133601 (2010).

[72] C. E. Shannon. A mathematical theory of communication. *Bell System Technical Journal* **27**, 379–423 (1948).

[73] A. Hyvärinen & E. Oja. Independent component analysis: algorithms and applications. *Neural Networks* **13**, 411–430 (2000).

[74] T. M. Cover & J. A. Thomas. *Elements of Information Theory* (2005).

[75] P. R. Bevington, D. K. Robinson & G. Bunce. Data Reduction and Error Analysis for the Physical Sciences, 2nd ed. *Am. J. Phys.* **61**, 766–767 (1993).

[76] S. Probst, F. B. Song, P. A. Bushev, A. V. Ustinov & M. Weides. Efficient and robust analysis of complex scattering data under noise in microwave resonators. *arXiv* (2014).

[77] Open-source library "resonator-tools". URL https://github.com/sebastianprobst/resonator_tools. [Online; accessed 20. Sep. 2023] (2023).

[78] Keysight. N5222A PNA Microwave Network Analyzer, 26.5 GHz [Discontinued]. *Keysight* (2021).

[79] C. Eichler & A. Wallraff. Controlling the dynamic range of a Josephson parametric amplifier. *EPJ Quantum Technol.* **1**, 1–19 (2014).

[80] S. M. Girvin. Basic Concepts in Quantum Information. *arXiv* (2013).

[81] V. I. Arnold. *Mathematical Methods of Classical Mechanics* (Springer, New York, NY, USA, 1978). URL `https://link.springer.com/book/10.1007/978-1-4757-1693-1`.

[82] G. Arfken. *Mathematical Methods for Physicists* (Academic Press, Inc., 1985), third edn.

[83] T. Yamaji, S. Kagami, A. Yamaguchi, T. Satoh, K. Koshino, H. Goto, Z. R. Lin, Y. Nakamura & T. Yamamoto. Spectroscopic observation of the crossover from a classical Duffing oscillator to a Kerr parametric oscillator. *Phys. Rev. A* **105**, 023519 (2022).

[84] A. Serafini. *Quantum Continuous Variables:A Primer of Theoretical Methods* (Taylor & Francis, Andover, England, UK, 2017).

[85] P. C. Parks. A. M. Lyapunov's stability theory 100 years on. *IMA J. Math. Control Inf.* **9**, 275–303 (1992).

[86] C. H. Meaney, H. Nha, T. Duty & G. J. Milburn. Quantum and classical nonlinear dynamics in a microwave cavity. *EPJ Quantum Technol.* **1**, 1–23 (2014).

[87] T. Kato. On the Adiabatic Theorem of Quantum Mechanics. *J. Phys. Soc. Jpn.* **5**, 435–439 (1950).

[88] W. H. Richardson. Bayesian-Based Iterative Method of Image Restoration$*$. *JOSA* **62**, 55–59 (1972).

[89] L. B. Lucy. An iterative technique for the rectification of observed distributions. *Astron. J.* **79**, 745 (1974).

[90] S. Boutin, D. M. Toyli, A. V. Venkatramani, A. W. Eddins, I. Siddiqi & A. Blais. Effect of Higher-Order Nonlinearities on Amplification and Squeezing in Josephson Parametric Amplifiers. *Phys. Rev. Appl.* **8**, 054030 (2017).

[91] S. Van der Walt, J. L. Schönberger, J. Nunez-Iglesias, F. Boulogne, J. D. Warner, N. Yager, E. Gouillart & T. Yu. scikit-image: image processing in Python. *PeerJ* **2**, e453 (2014).

[92] C. W. Clenshaw. A note on the summation of Chebyshev series. *Math. Comput.* **9**, 118–120 (1955).

[93] F. E. Schroeck. *Quantum Mechanics on Phase Space* (Springer Netherlands, Dordrecht, The Netherlands, 1996). URL `https://link.springer.com/book/10.1007/978-94-017-2830-0`.

[94] M. Zartab, E. Shojaee & S. Rahimi-Keshari. Filter functions for the Glauber-Sudarshan *P*-function regularization. *Phys. Rev. A* **107**, 053706 (2023).

[95] T. Kiesel, W. Vogel, V. Parigi, A. Zavatta & M. Bellini. Experimental determination of a nonclassical Glauber-Sudarshan *P* function. *Phys. Rev. A* **78**, 021804 (2008).

[96] C. Lüders, M. Pukrop, F. Barkhausen, E. Rozas, C. Schneider, S. Höfling, J. Sperling, S. Schumacher & M. Aßmann. Tracking Quantum Coherence in Polariton Condensates with Time-Resolved Tomography. *Phys. Rev. Lett.* **130**, 113601 (2023).

[97] B. Kühn & W. Vogel. Visualizing nonclassical effects in phase space. *Phys. Rev. A* **90**, 033821 (2014).

[98] F. Krumm & W. Vogel. Time-dependent nonlinear Jaynes-Cummings dynamics of a trapped ion. *Phys. Rev. A* **97**, 043806 (2018).

Acknowledgements

In this part, I would like to thank the people who contributed to this thesis.

To the **Deutscher Akademischer Austauschdienst**, for giving me the opportunity to do my M. Sc. in Munich. To **Prof. Dr. Rudolf Gross**, for giving me the opportunity to do my master's thesis at the Walther Meissner Institute.

To **Dr. Kirill Fedorov**, for being giving me the opportunity to do my thesis in the QMiCS group and for being my advisor throughout this work. I also thank you for your useful proofreading of this thesis.

To PhD student **Florian Fesquet**, for helping me with the experimental work and for always being there when I needed help.

To all the people of the QMiCs group and of the WMI.

Dediche

Nessun uomo è un'isola
Completo in se stesso
Ogni uomo è parte della terra
Una parte del tutto
Se una zolla è portata via dal mare
L'Europa risulta essere più piccola
Come se fosse un promontorio
Come se fosse una proprietà di amici tuoi
Come se fosse tua
La morte di ciascun uomo mi sminuisce
Perché faccio parte del genere umano
E perciò non chiederti
Per chi suoni la campana
Suona per te

Traduzione da John Donne

In queste pagine, una breve dedica a tutte le persone che, con il loro supporto, hanno reso possibile questo lavoro di tesi,
A **Po**, prima di tutti e più di tutti, perchè questo lavoro è mio nella misura in cui è anche tuo. Fare un elenco delle motivazioni sarebbe superfluo ed impossibile. Mi sforzo di fare un tentativo: per questi due anni di sacrifici e di rinunce; per questi due anni di spasmodiche attese e infinite videochiamate; per questi di anni di vederci due giorni una volta al mese; per questi due anni in cui mi hai dimostrato il tuo incodizionato supporto e il tuo indissolubile amore. Per avermi accolto ad ogni rientro e per avermi dato la forza di ripartire, ogni volta con lo stesso sorriso. Per avermi dato la forza di perseverare, quando ero allo stremo. Per le notti passate a correggere questa tesi. Per la gioia che provo nello stare insieme. Per credere in me, più di quanto lo faccia io stesso.
A **Ciro, Ferdinando, Geremia, Giovanni, Lucio, Mario** e al *PSMEFNS*, perché quando stiamo insieme, è come se non fossi mai partito. Per le sere passate insieme, nei pochi giorni in cui potevamo vederci, a prescindere da tutto. Per la vostra amicizia.
Alla mia famiglia, **Mamma, Papà, Beatrice e Chiara**, per esserci sempre stati, anche quando era difficile.
A mio **Nonno Sebastiano** e mia **Nonna Maria**, che, da qualche parte, fanno il tifo per me.
A **Claudia, Sergio e Patrizia**, per avermi fatto sempre sentire una persona di famiglia e accogliermi sempre con calore, a Napoli ed a Palinuro.

A **Tiffany, Sky, Oscar, Stellina, Toby e Fiocco**, per avermi fatto compagnia nelle lunghe notti di lavoro e di scrittura. Questa tesi, e' per voi.